

Vibrational Spectroscopy on thermally and optically switchable spin crossover compounds

Dissertation
zur Erlangung des Grades
Doktor der Naturwissenschaften

am Fachbereich Chemie und Pharmazie
der Johannes Gutenberg-Universität
in Mainz

Andreas Hofer
geboren in Koblenz

Mainz 2000

Tag der mündlichen Prüfung: 06.12.2000

“Die Erfahrung nutzt erst der Wissenschaft, sodann schadet sie, weil die Erfahrung Gesetz und Ausnahme gewahr werden läßt. Der Durchschnitt von beiden gibt keineswegs das Wahre.”

[Goethe: Wilhelm Meisters Wanderjahre]

Contents

1 INTRODUCTION	1
1.1 THE SPIN CROSSOVER PHENOMENON	1
1.2 SPIN CROSSOVER AND VIBRATIONAL SPECTROSCOPY - THE GOAL OF THIS THESIS	4
2 THEORETICAL SECTION	7
2.1 NORMAL COORDINATE ANALYSIS (NCA)	7
2.1.1 <i>The F Matrix</i>	7
2.1.2 <i>The FG method</i>	9
2.2 DENSITY FUNCTIONAL THEORY	10
2.3 THE SELECTION OF INTERNAL COORDINATES	12
2.4 NORMAL MODES OF AN OCTAHEDRON	17
3 EXPERIMENTAL SECTION	19
4 RESULTS A: $[M^{\text{II}}(\text{PTZ})_6](\text{BF}_4)_2$	23
4.1 THE SYSTEM $[M^{\text{II}}(\text{PTZ})_6](\text{BF}_4)_2$	23
4.2 FORMER VIBRATIONAL MEASUREMENTS	24
4.3 SINGLE CRYSTAL FIR SPECTRA ON LABELLED COMPLEXES	27
4.4 MIDDLE INFRARED SPECTRA	35
4.5 RAMAN SPECTRA OF $[\text{Fe}(\text{MTZ})_6](\text{BF}_4)_2$	39
4.6 DENSITY FUNCTIONAL CALCULATIONS	41
4.6.1 <i>The anion BF_4^-</i>	41
4.6.2 $[\text{M}(\text{NH}_3)_6]^{2+}$	42
4.6.3 <i>Propyl tetrazole (pure ligand)</i>	43
4.6.4 $[\text{M}(\text{N}_3)_4(\text{htz})_2]^{2-}$	46
4.6.5 $[\text{M}(\text{diimine})_2(\text{htz})_2]^{2+}$	46
4.7 NORMAL COORDINATE CALCULATIONS	49
4.7.1 <i>FeN₆ core</i>	49
4.7.2 <i>Fe(Rtz)₂N_{(EQ)4}</i>	53
5 THE SYSTEM $\{\text{Fe}[(\text{ENTZ})_3\text{N}]_2\}(\text{BF}_4)_2$	65
5.1 PHYSICAL PROPERTIES	65
5.2 RAMAN SPECTROSCOPY	66
5.2.1 <i>Spectral features</i>	66
5.2.2 <i>Light induced structural phase transitions</i>	67
5.2.3 <i>Low energy spectra of accessible species</i>	72
5.3 INFRARED SPECTRA	74
5.4 DFT CALCULATIONS	77
6 RESULTS C: $[\text{Fe}(\text{PHEN})_2(\text{NCS})_2]$	79
6.1 THE SYSTEM $[\text{Fe}(\text{PHEN})_2(\text{NCS})_2]$	79
6.2 INFRARED SPECTROSCOPY	80

CONTENTS

6.3 RAMAN SPECTROSCOPY	83
6.4 DISCUSSION C	88
7 DFT CALCULATIONS ON α-DIIMINE SYSTEMS	91
8 RESULTS D: [Fe^{II}(PM-R)₂(NCS)₂] SERIES	95
8.1 [Fe ^{II} (PM-BIA) ₂ (NCS) ₂]	96
8.2 [Fe ^{II} (PM-PEA) ₂ (NCS) ₂]	101
8.3 [Fe ^{II} (PM-A) ₂ (NCS) ₂]	106
8.4 [Fe ^{II} (PM-FLA) ₂ (NCS) ₂]	109
8.5 [Fe ^{II} (PM-DMA) ₂ (NCS) ₂]	114
8.6 [Fe ^{II} (PM-AzA) ₂ (NCS) ₂]	117
8.7 [Fe ^{II} (PM-BPM) ₂ (NCS) ₂]	120
8.8 [Fe ^{II} (PM-BMM) ₂ (NCS) ₂]	123
8.9 COMPARISON AND SUMMARY	126
9 SUMMARY	129
APPENDIX	131
A.1 DFT RESULTS ON TETRAZOLE LIGANDS:	131
A.2 DFT RESULTS ON [M(HTZ) ₂ (DIIMINE) ₂] ²⁺	133
A.2.1 [Zn(htz) ₂ (diimine) ₂] ²⁺	133
A.2.2 [Fe ^{HS} (htz) ₂ (diimine) ₂] ²⁺	135
A.2.3 [Fe ^{LS} (htz) ₂ (diimine) ₂] ²⁺	136
A.3 DFT RESULTS ON [Fe(PM-H)(DIIMINE)(NCS) ₂]	137
BIBLIOGRAPHY	143

1 Introduction

1.1 The Spin crossover phenomenon

Octahedrally coordinated transition metals with electron configurations of $[\text{Ar}]3d^4 - 3d^7$ can exist in two different electronic states depending on the ligand field strength of the ligand, namely a high spin (HS) or a low spin (LS) configuration. For example, d^6 - Fe(II) can have $^1A_{1g} (t_{2g}^6)$, i.e. LS, or $^5T_{2g} (t_{2g}^4 e_g^2)$, i.e. HS configuration.

The effect of the ligand field strength Dq on the spin state of the metal is represented in the Tanabe-Sugano diagram [SUG70] in Fig. 1.1:

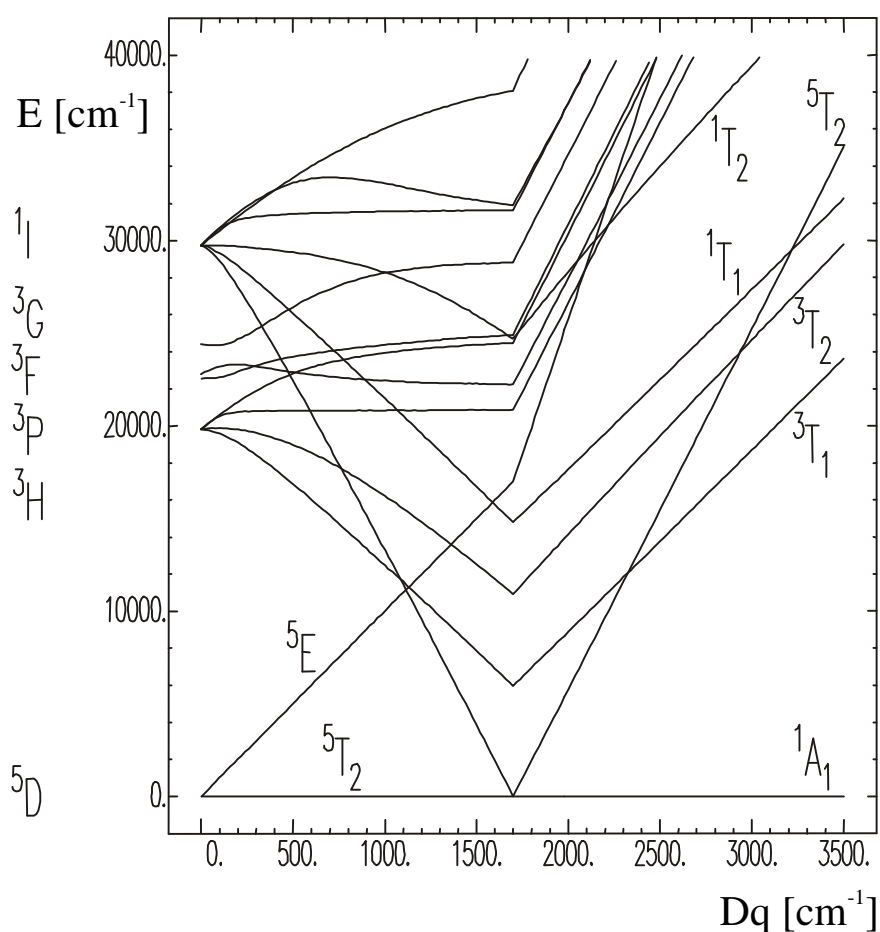


Figure 1.1: Tanabe-Sugano diagram for a $3d^6$ system, calculated with the Racah parameters of the free Fe(II)-ion $B = 917 \text{ cm}^{-1}$ and $C = 4040 \text{ cm}^{-1}$ [HAU91].

Complex molecules with rather small Dq values are in the HS state, whereas ligand field strengths above a critical value D_{crit} lead to a LS ground state. For Fe(II)-complexes the t_{2g} orbitals are of non-bonding character, whereas the e_g orbitals are anti-bonding. Therefore, the metal-ligand bond length r is significantly higher in the HS state than in the LS state, because in the former the anti-bonding orbitals are populated and, additionally, less electrons for d_{π} - p_{π}

back donation are available. Compounds with $\text{Fe}^{\text{II}}\text{N}_6$ core show typical values of $r_{\text{HS}} \approx 2.16 - 2.20 \text{ \AA}$ and $r_{\text{LS}} \approx 1.96 - 2.00 \text{ \AA}$ [MIK80, WIE86], i.e. a difference of about 10 % in the metal-ligand distance.

Because of a strong dependence of Dq on the bond length r ($Dq \sim \mu/r^6$ for neutral ligands [SCH80]), with μ being the dipole moment of the ligand, complexes with $10Dq$ values in the vicinity of the critical value D_{crit} can exist in both spin states. If the energy gap between the zero point energies of the two spin states DE_{HL} is within the range of thermal energies, a thermal spin crossover (SC) is possible, i.e. at low temperatures the complex molecule is in the $^1\text{A}_{1\text{g}}$ ground state and with increasing temperature the $^5\text{T}_{2\text{g}}$ state is populated. As the HS state has a fifteen-fold electronic degeneracy and a higher density of vibrational states (due to the weaker metal-ligand bond), this entropy-driven spin change occurs almost quantitatively. The two spin states show significant differences in their physical (e.g. magnetic or optical) properties which are used to monitor the spin transition.

The first example of a spin crossover was reported by *Cambi et al.* [CAM31] in 1931 on Fe-(III)-tris(dithiocarbamate) complexes. It took more than 30 years until the first Fe-(II) spin crossover system, namely $[\text{Fe}(\text{phen})_2(\text{NCS})_2]$ (phen = 1, 10 - phenanthroline), was found by *Baker et al.* [BAK64]. Since then the SC phenomenon and its mechanism has been studied extensively and reviewed by different authors [GÜT81, BEA88, TOF89, KÖN91, GÜT94].

The spin transition curve $\gamma_{\text{HS}}(\text{T})$, where γ_{HS} is the molar fraction of molecules in the HS state, can have very different forms, from gradual, as observed in solution, to very abrupt or even with hysteresis or steps due to cooperative effects in the solid state. Additionally, e.g. dislocations and defects in the crystal lattice may lead to a residual HS fraction at low temperatures. Cooperative interactions are understood in terms of elastic ones due to the large volume change between HS and LS molecules, i.e. long-range interactions, and secondly short-range nearest neighbour interactions. These can be used to model the spin transition [GÜT94 and references therein].

From calorimetric measurements values for the transition enthalpy $\Delta H_{\text{HL}} = H_{\text{HS}} - H_{\text{LS}} \approx 6 - 15 \text{ kJ/mol}$ and the transition entropy $\Delta S_{\text{HL}} = S_{\text{HS}} - S_{\text{LS}} \approx 40 - 65 \text{ J/mol/K}$ are known. Results from *Sorai et al.* [SOR74] on $[\text{Fe}(\text{phen})_2(\text{NCS})_2]$ reveal that the dominant part ($\sim 70 \%$) of the entropy change arises from contributions of inter- and intramolecular vibrations, which therefore are the major driving force for the spin crossover process. The remaining 30 % is the electronic (magnetic) contribution of the spin change.

With the discovery of the LIESST effect (i.e. **L**ight **I**nduced **E**xcited **S**pin **S**tate **T**rapping) by *Decurtins et al.* [DEC84, DEC85] in 1984 the area of spin transition research was expanded widely: it is also possible to populate the HS state by irradiation with light at low temperatures. With elucidating the mechanism by *Hauser et al.* [HAU86, HAU91b] it became clear, that the opposite direction, i.e. the light induced switching from the meta-stable HS to the LS ground state, is possible at different wavelengths, as well (reverse-LIESST effect). This mechanism is represented in Fig. 1.2.

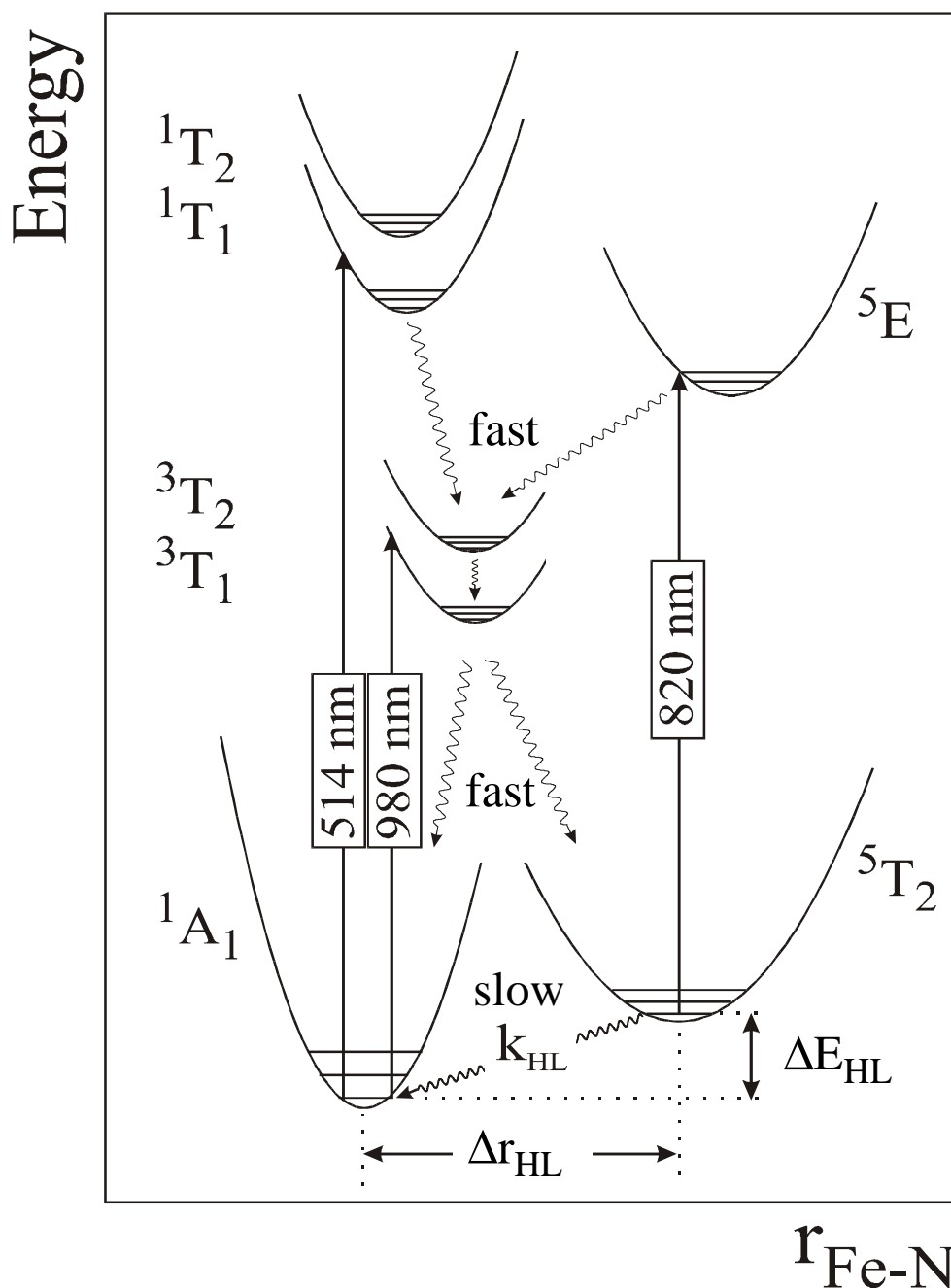


Figure 1.2: Mechanism of LIESST and reverse-LIESST according to *Hauser* [HAU91].

Irradiation into the LS d-d bands (i.e. the $^1A_1 \rightarrow ^1T_1 / ^1T_2$, or the spin forbidden triplet excitation) leads to a population of the 5T_2 HS state via one or two intersystem crossing steps, respectively. This metastable state is only depopulated by slow low temperature tunneling effects ($< \sim 50$ K) thus showing lifetimes from minutes to days. Low lying metal-ligand charge transfer (MLCT) transitions can be used for LIESST in the same way.

The other way round excitation into the ${}^5T_2 \rightarrow {}^5E$ band of the trapped HS state again produces the LS ground state. Due to the overlap of the quintet absorption band with the LS triplet excitation often only a steady state value of γ_{HS} is achieved.

1.2 Spin crossover and vibrational spectroscopy - the goal of this thesis

Because of the large electronic rearrangement during the spin crossover process, the metal-ligand bond is strongly weakened in the HS compared to the LS state, which can be seen in the change of the bond length of about 10 %. On the other hand this should also be reflected in the vibrational properties of the complexes. Since the totally symmetrical stretching mode is considered to be the most important reaction coordinate during the spin transition, and the main driving force are the entropic contributions of the intramolecular vibrations, from the very beginning of spin crossover research special efforts have been made to identify the corresponding relevant modes. Nevertheless reliable vibrational spectroscopic data are rather scarce. Quite a few researchers [HER86, KÖN67, SOR74, TOF84] used the CN stretch of coordinated isothiocyanate at around 2070 cm^{-1} , which shifts about 40 cm^{-1} to higher energies in the LS state, to monitor the spin transition, but only very few data concerning the metal-ligand stretching mode region are available until now.

The first detailed approach to this aim has been the work of *Takemoto et al.* [TAK72, TAK73, TAK74] on $[\text{Fe}(\text{phen})_2(\text{NCS})_2]$: They assign a shift in the Fe-N stretching frequency from 220 cm^{-1} (HS) to 375 cm^{-1} (LS) for Fe-N(phen) and from 252 cm^{-1} (HS) to 530 cm^{-1} (LS) for Fe-N(NCS), respectively. In a very simple approach of a single spring for one vibrational mode the vibrational energy ν is proportional to the square-root of the force constant f divided by the mass of the moving body m (i.e. $\nu \sim \sqrt{f/m}$). From this viewpoint especially the latter shift seems to be very high, as this would correspond to a factor of about 4.4 in harmonic force constants.

Early temperature dependent far infrared spectroscopic investigations by *Franke et al.* and *Müller et al.* [FRA82, MÜL83] on $[\text{Fe}(\text{ptz})_6](\text{BF}_4)_2$ (ptz = 1-n-propyltetrazole) suggested a change from 227 cm^{-1} to 413 cm^{-1} of the IR active T_{1u} metal ligand stretch, which would still mean a factor of 3.3 in squared frequencies (as a measure of the force constants) between LS and HS state. On the same compound *Jung* [JUN95] has found a factor of 1.24 in frequencies (i.e. 1.54 in force constants) from the evaluation of the ratio of the Mößbauer-Lamb factors. This discrepancy in experimental results needs further examination. In order to get an idea for the size of the different force constants, evaluated compounds with a HS or a LS state over the whole temperature range from the literature are compared (Table 1.1):

Lit.	Force Field	[Fe ^{HS} (NH ₃) ₆] ²⁺	[Fe ^{HS} (H ₂ O) ₆] ²⁺	[Fe ^{LS} (CN) ₆] ⁴⁻
[HUP85]	SVFF		1.52	
[KHA91]	SVFF	1.03	1.6	
[SCH75, SCH76]	GVFF	0.73		
[NAK64]	UBFF		0.76	
[NAK62]	UBFF			2.43
[GRI70]	JRI-FF			2.3

Table 1.1: Comparison of literature force constants [mdyn/Å] of pure HS and pure LS compounds.

Taking the extrema for a pure LS and a pure HS complex, a **factor of 3.3** in force constants would be an intrinsic limit, that should not be reached by a spin crossover complex.

First experiments utilising polarized Raman measurements on single crystals of [Fe(ptz)₆](BF₄)₂ [HOE95] have not been entirely successful. The totally symmetrical A_{1g} stretching mode of the octahedron could not be assigned unequivocally.

The aim of this work is to elucidate the low frequency assignments by the use of Raman and Infrared spectroscopy as well as calculations within the scope of normal coordinate analysis and density functional methods. Therefore, the structure of the thesis is as follows:

A theoretical section introduces the computational procedures used, i.e. normal coordinate analysis (NCA) and ab initio methods within the frame of density functional theory (DFT). After that the experimental methods are explained. In the next chapter the system [Fe(ptz)₆](BF₄)₂ is presented by reviewing the Raman spectroscopic results [HOE95] and afterwards showing the infrared spectroscopic measurements on isotope labelled single crystals with the metals ⁵⁴Fe, ⁵⁶Fe, ⁶⁴Zn, ⁶⁸Zn in comparison with experiments on pellets and mulls. Using these data the infrared active metal-ligand stretching modes are assigned by the help of the NCA and DFT calculations.

In chapter 5 the similar but two dimensional system {Fe[(entz)₃N]₂}(BF₄)₂ ((entz)₃N = tris(tetrazol-1-yl-ethane)amine) is introduced. Light induced phase transitions at low temperatures are described. Assignments in the low frequency range of the Raman and IR spectra conclude this chapter.

The next chapters deal with a series of spin crossover complex molecules with two α-diimine and two cis-NCS ligands: starting with the ‘classical’ [Fe(phen)₂(NCS)₂] system the Raman and IR spectra of this compound are discussed including isotope labelled IR measurements with ¹⁵N¹³CS. The low frequency modes are reassigned in comparison to the literature data.

The very similar series of [Fe(PM-R)₂(NCS)₂] (PM-R = N-(2'-pyridylmethylene)-amino-R) with different substituents R is presented with their Raman and infrared spectroscopic results. DFT calculations on a simplified model are considered for the assignments on these systems. The results are summarized and discussed in connection to the spin crossover phenomenon.

2 Theoretical Section

2.1 Normal Coordinate Analysis (NCA)¹

Every molecule has three types of internal energy, namely electronic, vibrational, and rotational energies. Each molecule is continually executing vibrational motions, i.e. motions in which interatomic distances or internal angles change periodically without producing any net translation of the centre of mass of the molecule or imparting any net angular momentum to the molecule. Therefore, the vibrational motions can be separated from the translational and rotational degrees of freedom.

An appropriate basis for describing the motions of a molecule consisting of N atoms are the $3N$ cartesian displacement coordinates ($\mathbf{D}x_i$, $\mathbf{D}y_i$, $\mathbf{D}z_i$). Subtracting 3 translational and 3 rotational degrees of freedom for a non-linear molecule $3N-6$ vibrational degrees of freedom remain. Those normal modes can be expressed as linear combinations of the cartesian displacement coordinates.

For practical reasons, especially for describing the normal modes in a more geometry depending way that corresponds to the idea of chemical bonding, the so called *internal displacement coordinates* ('internals') are constructed. These consist of stretches of bond lengths ($\mathbf{D}r$), bends of bond angles ($\mathbf{D}\alpha$), and torsions ($\mathbf{D}\tau$). For simplicity \mathbf{D} frequently is omitted. This way more than the $3N-6$ necessary coordinates are often obtained. These additional coordinates are therefore called '*redundant*'. They are used for constructing simple expressions for the *symmetrized internals* (see below).

2.1.1 The F Matrix

Assuming that the nuclei vibrate harmonically, the potential energy V of the molecule may be written as:

$$2V = \sum_{i,k} f_{ik} s_i s_k \quad (2.1)$$

where s_i and s_k are internal displacement coordinates, $f_{ik} = f_{ki}$ are the force constants. A term such as $f_{ii} s_i^2$ represents the potential energy of stretching at a given bond or bending at a given angle, whereas cross terms represent the energies of interaction between such motions.

E.g. the water molecule (H_2O) can be described in terms of three internal coordinates, namely two O-H stretches (r_1 and r_2) and the bend of the H-O-H angle (α). The potential energy of H_2O can then be written as:

¹ This section is based on [COT90]. For a detailed treatment see [WIL55].

$$2V = f_r r_1^2 + f_r r_2^2 + f_a \alpha^2 + 2f_{ra} r_1 \alpha + 2f_{ra} r_2 \alpha \quad (2.2)$$

The force constants can also be written in matrix representation which is called the f-matrix:

	r_1	r_2	α
r_1	f_r	f_{rr}	f_{ra}
r_2	f_{rr}	f_r	f_{ra}
α	f_{ra}	f_{ra}	f_a

f_r represents the force constant for the O-H stretching motion and f_a the one for the H-O-H bend, respectively. The off-diagonal elements f_{rr} and f_{ra} connect these different motions. Here already some symmetry information has been used, as the O-H bonds are taken to be equal, i.e. $f_{r1} = f_{r2} = f_r$.

One can also make use of symmetry-related linear combinations of internal coordinates, and then express the potential energy in terms of the so called *symmetry coordinates* S_j :

$$2V = \sum_{j,l} F_{jl} S_j S_l \quad (2.3)$$

From that results a symmetry factorization of the \mathbf{F} matrix simplifying further calculations (see below). For H_2O two vibrations of A_1 and one of B_1 symmetry are obtained:

$$\begin{aligned} S_1^{A_1} &= \frac{1}{\sqrt{2}}(r_1 + r_2) \\ S_2^{A_1} &= \alpha \\ S_1^{B_1} &= \frac{1}{\sqrt{2}}(r_1 - r_2) \end{aligned}$$

The unitary transformation \mathbf{U} transforms the internal into symmetry coordinates:

	r_1	r_2	α
$S_1^{A_1}$	$\frac{1}{\sqrt{2}}$	$\frac{1}{\sqrt{2}}$	0
$S_2^{A_1}$	0	0	1
$S_1^{B_1}$	$\frac{1}{\sqrt{2}}$	$-\frac{1}{\sqrt{2}}$	0

Using the \mathbf{U} matrix the basis transformation of the \mathbf{f} matrix according to:

$$\mathbf{F} = \mathbf{U} \mathbf{f} \mathbf{U}^T \quad (2.4)$$

leads to the symmetry based \mathbf{F} matrix in terms of the internal force constants f_{ik} :

$$\begin{array}{c}
 S_1^{A_1} \\
 S_2^{A_1} \\
 S_1^{B_1}
 \end{array}
 \begin{array}{ccc}
 S_1^{A_1} & S_2^{A_1} & S_1^{B_1} \\
 \hline
 f_r + f_{rr} & \sqrt{2} f_{ra} & 0 \\
 \sqrt{2} f_{ra} & f_a & 0 \\
 0 & 0 & f_r - f_{rr}
 \end{array}$$

2.1.2 The FG method

For the calculation of the force constants and the normal modes of a molecule *Wilson's* method of \mathbf{F} and \mathbf{G} matrices [WIL55] is applied. The master equation

$$|\mathbf{FG} - \mathbf{E}\lambda| = 0 \quad (2.5)$$

has to be solved, where \mathbf{F} is the force constants matrix in terms of symmetry coordinates (see 2.1.1) representing the potential energy, \mathbf{G} is a matrix that involves the masses and certain spatial relationships of the atoms, and therefore stands for the kinetic energy, and \mathbf{E} is the unit matrix. The solution of this secular equation yields the vibrational frequencies as square roots of the eigenvalues λ_i , and the obtained eigenvectors are the so called *normal coordinates* Q_i .

The last thing before solving the problem is the construction of the \mathbf{G} matrix which is set up by a similar procedure to that used for the \mathbf{F} matrix. According to

$$\mathbf{G} = \mathbf{U} \mathbf{g} \mathbf{U}^T \quad (2.6)$$

e.g. the (symmetrical) general \mathbf{g} matrix of water

$$\begin{array}{c}
 r_1 \\
 r_2 \\
 \alpha
 \end{array}
 \begin{array}{ccc}
 r_1 & r_2 & \alpha \\
 \hline
 g_{11} & g_{12} & g_{13} \\
 g_{21} & g_{22} & g_{23} \\
 g_{31} & g_{32} & g_{33}
 \end{array}$$

with the elements in terms of the reciprocal of the mass of atom A μ_A ($A = \text{O}, \text{H}$) and the dimensions of the molecule $|r|$ (O-H bond length) and $|\alpha|$ (H-O-H bonding angle), as taken from general expressions tabulated e.g. in [COT90],

$$\begin{aligned}
 g_{11} &= g_{22} = \mu_H + \mu_O \\
 g_{12} &= \mu_O \cos |\mathbf{a}| \\
 g_{13} &= g_{23} = -(\mu_O / |r|) \sin |\mathbf{a}| \\
 g_{33} &= 2(\mu_H + \mu_O - \mu_O \cos |\mathbf{a}|) / |r|^2
 \end{aligned}$$

is transformed into the \mathbf{G} matrix in the basis of symmetry coordinates:

	$S_1^{A_1}$	$S_2^{A_1}$	$S_1^{B_1}$
$S_1^{A_1}$	$g_{11} + g_{12}$	$\sqrt{2} g_{13}$	0
$S_2^{A_1}$	$\sqrt{2} g_{13}$	g_{33}	0
$S_1^{B_1}$	0	0	$g_{11} - g_{12}$

Thus \mathbf{G} is symmetry-factored in the same way as \mathbf{F} , and the secular equation separates into different symmetry blocks.

A problem in computing force constants (from given experimental fundamental frequencies) is that usually a force field which accounts for the principal interaction constants, as well as the stretching and bending constants will contain more constants to evaluate than there are fundamental frequencies. One way of coping with this is to get vibrational data on isotope substituted molecules, thereby providing an additional set of equations with identical \mathbf{F} and only slightly changed \mathbf{G} matrix elements. Another solution that has been followed in a way in this work is to get good starting values for \mathbf{F} by means of other calculations, e.g. DFT calculations which will be discussed in the next chapter.

2.2 Density functional theory²

A system of K nuclei and N electrons is described by the time-independent Schrödinger equation. In the Born-Oppenheimer approximation (separation of the motion of the nuclei and the electrons) the Eigenvalue problem:

$$H\Psi = E\Psi \quad (2.7)$$

with E the total electronic energy, Ψ the wave function of a stationary state is solved. The electronic Hamilton operator:

$$H = T + V_{ne} + V_{ee} \quad (2.8)$$

² This section is based on [SZA89, FOR95] and the detailed representation in [PAR89]

is expressed by the kinetic energy of the electrons

$$T = -\frac{1}{2} \sum_{i=1}^N \nabla_i^2 \quad (2.9),$$

the electron-nucleus attraction energy

$$V_{ne} = \sum_{i=1}^N v(\mathbf{r}_i) \quad (2.10)$$

with the potential $v(\mathbf{r}_i)$ acting on electron i :

$$v(\mathbf{r}_i) = - \sum_{a=1}^K \frac{Z_a}{r_{ia}} \quad (2.11)$$

and finally the electron-electron repulsion

$$V_{ee} = \sum_{i < j}^N \frac{1}{r_{ij}} \quad (2.12).$$

T and V_{ee} depend on the N electron coordinates in contrast to V_{ne} that depends on the geometrical arrangement of the nuclei.

The DFT approach is based upon a strategy of modelling electron correlation via general functionals of the electron density (according to the Hohenberg-Kohn theorems, that state that the ‘external’ potential $v(\mathbf{r})$ is determined by the electron density $\rho(\mathbf{r})$, and that for a trial density $\tilde{\rho}(\mathbf{r})$, such that $\tilde{\rho}(\mathbf{r}) \geq 0$ and $\int \tilde{\rho}(\mathbf{r}) d\mathbf{r} = N$ the true ground state energy E_0 can be found by minimizing in a variational way the energy functional $E_v[\tilde{\rho}]$). However, the explicit form of this functional is not known.

Following the work of *Kohn and Sham* of 1965 the approximate functionals employed in today's DFT methods partition the electronic energy into the kinetic energy term E^T , the potential energy of the nuclear-electron attraction and of the repulsion of pairs of nuclei E^V , the electron-electron repulsion (Coulomb self-interaction of the electron density) E^J , and the exchange correlation term, E^{XC} , accounting for the remaining part of the electron-electron interactions. All terms except the nuclear-nuclear repulsion are functions of the electron density ρ . $E^T + E^V + E^J$ corresponds to the classical energy of the charge distribution ρ . E^{XC} is usually divided into separate parts, namely the exchange and correlation parts, that both are again functions of the electron density:

$$E^{XC}[\mathbf{r}] = E^X[\mathbf{r}] + E^C[\mathbf{r}] \quad (2.13)$$

One of the first functionals used is the local exchange functional derived from the uniform electron gas (local density approximation, LDA):

$$E_{LDA}^X = -\frac{3}{2} \left(\frac{3}{4\pi} \right)^{\frac{1}{3}} \int \rho^{\frac{4}{3}} d\mathbf{r} \quad (2.14)$$

In 1988 *Becke* improved this functional by adding gradient corrections:

$$E_B^X = E_{LDA}^X - \gamma \int \frac{\rho^{\frac{4}{3}} x^2}{(1 + 6\gamma \sinh^{-1} x)} d\mathbf{r} \quad (2.15)$$

where $x = \rho^{-4/3} |\nabla\rho|$. γ is a parameter chosen to fit known exchange energies of the inert gas atoms. Similarly, there are local (e.g. derived from quantum Monte Carlo calculations by *Vosko*, *Wilk*, and *Nusair*; VWN) and gradient-corrected correlation functionals, e.g. the formulations of *Perdew* and *Wang* (PW91) or *Lee*, *Yang*, and *Parr* (LYP) which are the most commonly used functionals today. A wide spread functional that has been used in this work as well is the hybrid functional B3LYP that includes a Hartree-Fock exchange part:

$$E_{B3LYP}^{XC} = E_{LDA}^X + c_1 (E_{HF}^X - E_{LDA}^X) + c_2 \Delta E_B^X + E_{VWN}^C + c_3 (E_{LYP}^C - E_{VWN}^C) \quad (2.16)$$

The constants c_1 , c_2 and c_3 have been determined by *Becke* by fitting to the atomisation energies, ionisation potentials, proton affinities and first-row atomic energies of a set of molecules.

2.3 The selection of internal coordinates

When trying to interpret calculational results beyond a simple frequency inspection one always thinks in terms of classical springs connecting the N different atoms of a molecule. The strength of the chemical bond is explained by the value of the spring constant. Therefore, the non-illustrative cartesian coordinates x_i are transformed into internal displacement coordinates s_i . These consist of stretches, bends and torsions. The potential energy in the framework of the classical picture in terms of those internals is expressed as

$$2V = \sum_i f_{ii} s_i^2. \quad (2.17)$$

This means no off-diagonal elements in the \mathbf{f} -matrix occur when thinking of simple springs. In other words all off-diagonal interaction force constants are of a pure quantum-mechanical origin.

In principle, the choice of the internal coordinate system for the description of the interatomic potential is arbitrary. For example the \mathbf{f} -matrix of the water molecule can be expressed

in terms of the three interatomic distances r_1 , r_2 (O-H distance) and r_3 (H-H distance). If the cartesian force constants obtained by means of DFT calculations are transformed into a basis of internal displacement coordinates, one gets the following **f**-matrix (force constant units are [mdyn/Å] for stretches and their interactions, [mdyn·Å] for bends and their interactions and [mdyn] for stretch-bend interactions, where 1 dyn = 0.01 mN):

	r_1	r_2	r_3
r_1	8.1996		
r_2	0.2785	8.1996	
r_3	-1.1873	-1.1873	2.2332

Choosing the bend of the H-O-H angle α as an internal instead of the H-H distance r_3 leads to

	r_1	r_2	α
r_1	7.7475		
r_2	-0.1737	7.7475	
α	0.3559	0.3559	0.7071

This clearly demonstrates the influence of the selection of the coordinates: on one hand the resulting value for the O-H stretching force constant differs, on the other hand the interaction force constants change dramatically. In order to judge which set of internals is better to describe the molecule by classical springs, an evaluation of the gained force field by the NCA procedure ignoring all off-diagonal elements f_{ij} ($i \neq j$) has been done. The calculated frequencies [cm^{-1}] using the three distances r_1 , r_2 and r_3 as a basis

	$f_{ij} \neq 0$	$f_{ij} = 0$	difference
ν_{as}	3801	3868	67
ν_{s}	3644	4466	822
δ	1613	1404	-209

deviate strongly from the complete picture with included interaction constants. Especially the symmetric stretch is shifted more than 800 cm^{-1} upwards. Therefore, the force constants of the three interatomic distances are a bad description of the water molecule.

Replacement of r_3 by α improves the idea of springs a lot:

	$f_{ij} \neq 0$	$f_{ij} = 0$	difference
ν_{as}	3801	3760	-41
ν_{s}	3644	3689	45
δ	1613	1652	38

The deviation from the exact solution is rather small, because only minor values on the off-diagonal elements have to be neglected. It is in the same order of magnitude as the differences between the DFT calculations and the experimental values. The measured modes are at 3756 , 3652 and 1595 cm^{-1} [VOL72]. Consequently, the two O-H stretches and the H-O-H bend are a good basis for the discussion of the water molecule, and the diagonal elements f_{rr} can satisfactorily be interpreted as bond strengths.

To further demonstrate this influence, another trinuclear molecule, i.e. \mathbf{B}_3^+ , is calculated by means of density functional methods and proceeded in the same way as above.

The (r_1, r_2, α) basis leads to the \mathbf{f} -matrix:

	r_1	r_2	α
r_1	4.3254		
r_2	0.1876	4.3254	
α	2.0439	2.0439	6.9467

Rather large off-diagonal elements lead to deviations from the exact solution when ignored:

	$f_{ij} \neq 0$	$f_{ij} = 0$	difference
$\nu_s(A_1)$	1179	1473	294
$\nu_s(E)-1$	978	1000	22
$\nu_s(E)-2$	978	895	-82

Also, the degeneracy of the lower energetic stretching mode is removed.

Describing the equilateral molecule with three equivalent distances $r_1, r_2,$ and r_3 the following \mathbf{f} -matrix is generated:

	r_1	r_2	r_3
r_1	3.7614		
r_2	-0.3764	3.7614	
r_3	-0.3764	-0.3764	3.7614

Neglecting the off-diagonal elements yields the frequencies [cm^{-1}]:

	$f_{ij} \neq 0$	$f_{ij} = 0$	difference
$\nu_s(A_1)$	1179	1319	140
$\nu_s(E)-1$	978	933	-45
$\nu_s(E)-2$	978	933	-45

It can be seen that the modes are reproduced much better, and the degeneracy of the E-symmetry stretch is preserved, as well. Hence, this trinuclear system is preferably described with three bond distances.

This, of course, matches the ‘chemical intuition’. The molecule is represented best in terms of valence internal coordinates, i.e. stretches of chemical bonds and bends of valence angles. Nevertheless, there remains some arbitrariness, especially in the number of internals used to describe the $3N-6$ vibrational degrees of freedom.

Every new coordinate introduces an additional ‘spring’ with more or less large influence on the distribution of the potential energy among the internals. Thus, as few coordinates as possible should be used. But because of the geometric connection not all possible valence internal coordinates are linearly independent. This in general leads to a number larger than $3N-6$ of internal coordinates used to physically meaningful describe the molecular system: some

redundancy is obtained. E.g. the CH₄ tetrahedron may be perfectly expressed by four C-H bond stretches and five of the six angles (i.e. exactly $3N-6 = 9$ coordinates).

	r₁	r₂	r₃	r₄	a₁	a₂	a₃	a₄	a₅
r₁	5.317								
r₂	0.027	5.317							
r₃	0.027	0.027	5.317						
r₄	0.027	0.027	0.027	5.317					
a₁	0.17	0.17	-0.17	-0.17	1.148				
a₂	0.17	0	0	-0.17	0.574	1.175			
a₃	0.17	0	-0.17	0	0.574	0.588	1.175		
a₄	0	0.17	0	-0.17	0.574	0.588	0.601	1.175	
a₅	0	0.17	-0.17	0	0.574	0.601	0.588	0.588	1.175

The sixth angle can be expressed by the other five. The redundancy relation $\sum_i a_i = 0$ is valid. Nevertheless, the introduction of the tenth internal coordinate makes sense: which peculiarity should distinguish one angle from the others. Therefore a force field with equivalent force constants for all six angles is much more meaningful.

	r₁	r₂	r₃	r₄	a₁	a₂	a₃	a₄	a₅	a₆
r₁	5.317									
r₂	0.027	5.317								
r₃	0.027	0.027	5.317							
r₄	0.027	0.027	0.027	5.317						
a₁	0.085	0.085	-0.085	-0.085	0.488					
a₂	0.085	-0.085	0.085	-0.085	-0.1	0.488				
a₃	0.085	-0.085	-0.085	0.085	-0.1	-0.1	0.488			
a₄	-0.085	0.085	0.085	-0.085	-0.1	-0.1	-0.087	0.488		
a₅	-0.085	0.085	-0.085	0.085	-0.1	-0.087	-0.1	-0.1	0.488	
a₆	-0.085	-0.085	0.085	0.085	-0.087	-0.1	-0.1	-0.1	-0.1	0.488

One can see the dramatic reduction of the angle-bend force constant by a factor of about two just by the introduction of the additional redundant coordinate. But the off-diagonal elements are lowered, as well.

To demonstrate the possible influence of such a redundant coordinate the two examples from above, H₂O and B₃⁺, are evaluated with r₁, r₂, α and r₃ as internal coordinates:

H₂O:

	r₁	r₂	α	r₃
r₁	4.859			
r₂	-3.0621	4.859		
α	-0.5843	-0.5843	0.786	
r₃	1.1354	1.1354	-0.51	1.5634

B₃⁺:

	r ₁	r ₂	α	r ₃
r ₁	3.2817			
r ₂	-0.8561	3.2817		
α	-0.4635	-0.4635	1.0234	
r ₃	0.5831	0.5831	0.927	1.8425

In the case of H₂O the diagonal elements for r₁ and r₂ are far away from the earlier obtained force constants. Very large off-diagonal elements show up. The B₃⁺ example is not that bad concerning r₁ and r₂. But the strong correlation between r₃ and α however introduces larger off-diagonal elements than before and the potential energy is distributed among both coordinates.

In summary, the selection of appropriate internal coordinates to some extent remains intuitive and arbitrary. One should confine oneself to valence internal coordinates, i.e. no stretches between non-bonded atoms should be used. Since the complete renunciation of redundancies is not wanted or nearly impossible for larger systems, only the careful examination of the obtained **f**-matrix shows the significance of those values. Only blocks of the matrix that are more or less diagonal can be interpreted like classical springs and are therefore a quantitative description of bond strengths.

2.4 Normal modes of an octahedron

In order to analyse the vibrations of a spin crossover complex with six nitrogen donor atoms at the ligands it is obvious first to look at the possible normal modes of an octahedron built up by the FeN_6 core, thereby assuming that the intraligand forces are much higher than those of the metal-ligand forces.

The cartesian coordinates of the seven atoms are a basis of the 21-fold reducible representation of the molecule considered in O_h symmetry:

O_h	E	8 C_3	6 C_2	6 C_4	3 C_2	i	6 S_4	8 S_6	3 σ_h	6 σ_d
Γ_{tot}	21	0	-1	3	-3	-3	-1	0	5	3

Applying the reduction formula one gets the irreducible representations of Γ_{tot} :

$$\Gamma_{\text{tot}} = A_{1g} \oplus E_g \oplus T_{1g} \oplus 3 T_{1u} \oplus T_{2g} \oplus T_{2u} .$$

T_{1g} and one T_{1u} belong to the rotational and translational degrees of freedom, respectively. The remaining vibrational degrees of freedom of an octahedral molecule are represented by

$$\Gamma_{\text{vib}} = A_{1g} \oplus E_g \oplus 2 T_{1u} \oplus T_{2g} \oplus T_{2u} .$$

From group-theoretical considerations on selection rules it follows that A_{1g} , E_g , and T_{2g} are Raman active, 2 T_{1u} modes are expected in the infrared spectrum and one T_{2u} mode is spectroscopically silent.

A normal coordinate analysis of a simple octahedral molecule reveals the form of the atom displacements of the different normal modes (i.e. the normal coordinates). These are shown in figure 2.1:

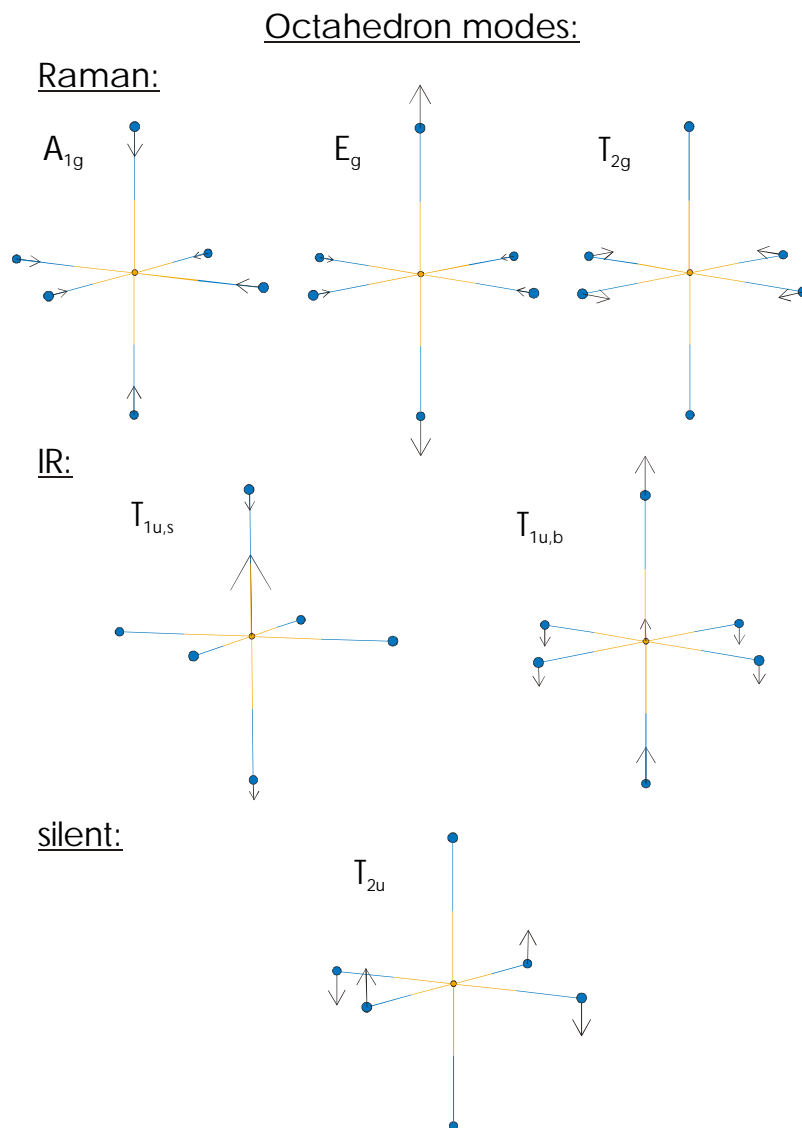


Figure 2.1: Normal modes of an octahedral molecule

These octahedral modes can further split under the influence of lower molecular symmetry or lower site symmetry in the lattice. Additionally, they may be coupled to intra-ligand modes of the same symmetry.

3 Experimental Section

Sample preparation of $[Fe(ptz)_6](BF_4)_2$

$[Fe(Rtz)_6](BF_4)_2$ (with $Rtz = ptz, mtz$) and its zinc analogue have been prepared from $[M^{II}(H_2O)_6](BF_4)_2$ and 1-n-propyl-1-H-tetrazole (ptz) or 1-methyl-1-H-tetrazole (mtz), respectively, according to *Schmitt* [SCH89] based on the original preparation by *Franke et al.* [FRA82] in a mixture of water and ethanol as solvent and recrystallized from nitromethane. This leads to large hexagonal single crystals in a quality very well suited for optical measurements. They can be split manually along the ab-plane in order to get thicknesses well below 100 μm suitable for transmission infrared spectroscopy.

Isotope labelled compounds of $[M^{II}(ptz)_6](BF_4)_2$ with the metals ^{54}Fe , ^{56}Fe , ^{64}Zn , and ^{68}Zn (Chemotrade, Düsseldorf, Germany) in a purity >90%, have been prepared in the same manner using 100 mg of the metal in a 10 ml flask each. Single crystals in a similar quality as the natural isotope complexes were achieved and used for vibrational spectroscopy.

Sample preparation of $[Fe(entz_3N)_2](BF_4)_2$

The pure ligand $entz_3N$, i.e. tris(tetrazol-1-yl-ethane)amine, as well as the white powder of the two-dimensional $[Fe(entz_3N)_2](BF_4)_2$ (α -phase) have been prepared in the group of Prof. M. F. Rudolf (Wroclaw, Poland) [RUD95, BRO96].

Sample preparation of $[Fe(phen)_2(NCS)_2]$

Samples of $[Fe(phen)_2(NCS)_2]$ with $phen = 1,10$ -phenanthroline have been prepared following the extraction method [GAN81] (method B) from $[Fe(phen)_3](NCS)_2$ in acetone originally proposed by *Madeja et al.* [MAD66] yielding a dark violet, fine powder.

The analogous isotope labelled $[Fe(phen)_2(^{15}N^{13}CS)_2]$ was done in the group of Prof. J. J. McGarvey (Belfast, Northern Ireland) making use of the precipitation route (method A) [GAN81] where 1,10-phenanthroline monohydrate is added to a stirred solution of $Fe(^{15}N^{13}CS)_2$.

Sample preparation of $[Fe(PM-R)_2(NCS)_2]$

The powder samples of the series of compounds $[Fe(PM-R)_2(NCS)_2]$ with $PM-R = N$ -(2'-pyridylmethylene)-amino-R with different substituents R have been prepared in the group of Prof. O. Kahn (Bordeaux, France) according to the literature [LET97, LET97b, LET98].

Raman spectroscopy

Temperature dependent Raman spectroscopy was carried out employing a setup involving the following components: Spectra Physics 2020 5W Ar⁺- laser (488 or 514 nm); Spectra Physics 2080 Kr⁺- laser (752 or 799 nm); liquid helium bath-cryostat (Cryovac) for measurements from 4.2 to 300 K; SPEX 1404 0.85 m double monochromator equipped with CCD camera (PI Instruments, 1024 x 256 pixels EEV chip, liquid nitrogen cooled; spectrograph mode) and Peltier-cooled RCA 31034 detector connected to a Stanford Research SR 400 photon counter (scanning mode). Spectral resolution was typically set to ~ 3.5 cm⁻¹. Standard laser powers were kept between 20 and 100 mW depending on the scattering intensity and the sensitivity for laser heating effects.

For the measurements powder samples were pressed into the groove of a copper holder placed directly into the stream of helium gas.

Infrared spectroscopy

Middle infrared (MIR) and far infrared (FIR) measurements were done on a Bruker IFS 66v/S FTIR-spectrometer equipped with an Oxford Optistat^{CF} dynamic continuous flow helium cryostat with zinkselenide (MIR) and polyethylene windows (FIR), respectively, allowing a temperature range from 15 to 300 K. Usually, a globar light source was used (Hg-lamp for spectra < 100 cm⁻¹). A DTGS detector was implemented for the MIR range, whereas in the far infrared besides a DTGS a liquid helium cooled silicon bolometer was utilized for signal registration. As beamsplitters KBr (MIR) and 6 μ (550 - 100 cm⁻¹) or 50 μ mylar films (100 - 10 cm⁻¹) have been employed.

The spectrometer's front plate was modified with a BK7 glass window in order to allow irradiation of the cooled sample with laser light of different wavelengths.

The resolution of the spectra was set to 2 cm⁻¹ (DTGS) or 1 cm⁻¹ (bolometer), respectively, typically accumulating 500 scans for each spectrum.

Single crystals of [M^{II}(Rtz)₆](BF₄)₂ were split along the ab-plane achieving a thickness far less than 100 μ m thus allowing transmission experiments with the crystals glued to a copper sample holder. All powder samples were processed as CsI or polyethylene (PE) pellets or as nujol mulls between thin PE discs, without grinding the sample!

Normal Coordinate Analysis

Normal coordinate calculations have been performed using the QCPE computer program 576 by *M. R. Peterson* and *D. F. McIntosh* that involves the diagonalization procedure of *Miyazawa* [MIY58] for solving the secular equation $GFL = LL$. The calculations are based on a general valence force field. Due to the lack of additional experimental data no refinement on the force constants has been executed. The visualisation of the normal eigenvectors was done with the molecular graphics program *XMol* [XMO93].

DFT calculations

Spin restricted (LS, Zn, ligands) and unrestricted (HS) density functional calculations have been done with the use of *Becke's* three parameter hybrid exchange functional in combination with the correlation functional of *Lee, Yang, and Parr* (B3LYP) [BEC93] and the LanL2DZ basis set that applies Dunning/Huzinaga full double zeta (D95) [DUN76] basis functions on first row and Los Alamos effective core potentials plus DZ functions on all other atoms [HAY85, WAD85]. The calculational procedures were used as implemented in the *Gaussian94* E.2 program package [GAU94]. The program was run on a DEC-8400 M 5/300 alpha machine with OSF/1 V4.0 and a RAM memory between 100 and 500 MB.

For visualisation purposes the graphic programs *Molden* [SCH96] and *XMol* [XMO93] have been used. The extraction of force constants in internal coordinates from the *Gaussian94* output was done with the help of *Redong* [ALL93].

4 Results A: $[\text{M}^{\text{II}}(\text{ptz})_6](\text{BF}_4)_2$

4.1 The system $[\text{M}^{\text{II}}(\text{ptz})_6](\text{BF}_4)_2$

$[\text{Fe}(\text{ptz})_6](\text{BF}_4)_2$ (ptz = 1-n-propyl-tetrazole) shows an abrupt and complete thermal spin transition first investigated by *Franke et al.* [FRA82] and *Müller et al.* [MÜL83b]. The spin transition is accompanied by a first-order crystallographic phase transition leading to a hysteresis of about 7 K ($T_{1/2}^{\downarrow} = 128$ K, $T_{1/2}^{\uparrow} = 135$ K). The metal-ligand distance changes by $\Delta r_{\text{HL}} \approx 0.18$ Å. The crystallographic phase transition can be suppressed by rapid cooling (> 2 K/min). Then a spin transition temperature of $T_{1/2} = 125$ K [OZA89] in the $R\bar{3}$ high temperature phase [FRA82, WIE93] is observed. The core of the LS complex has almost octahedral geometry, whereas the HS form is slightly Jahn-Teller distorted along the 3-fold axis.

The LS compound is deep purple and the HS compound is colourless. The evaluation of the UV-Vis spectra (fig. 4.1) results in ligand field strengths of $10 Dq = 11760$ cm^{-1} in the HS and $10 Dq = 20550$ cm^{-1} in the LS state, respectively. These values fit into the narrow range expected for spin crossover complexes [HAU91].

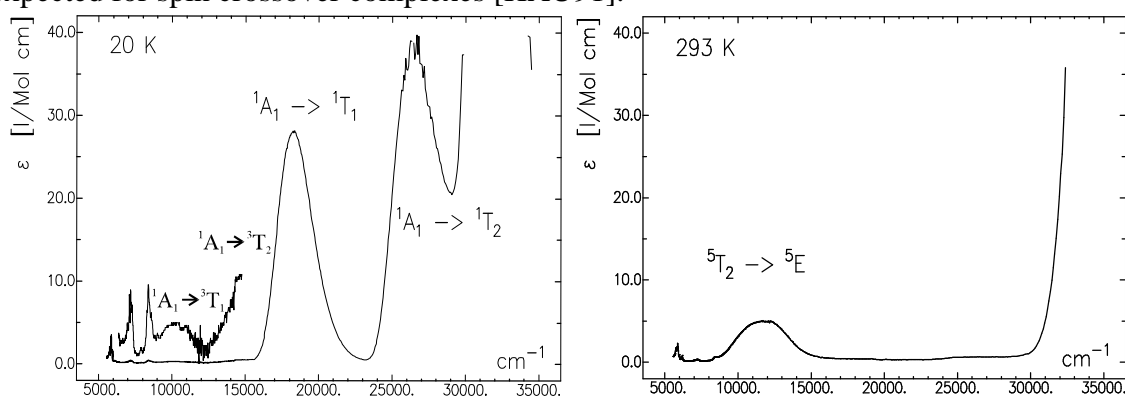


Figure 4.1: UV-Vis spectra of $[\text{Fe}(\text{ptz})_6](\text{BF}_4)_2$ at 20 K (LS) and 293 K (HS) (the spin forbidden triplet bands are enlarged in the insert) [HAU91].

Irradiation into the ${}^1A_1 \rightarrow {}^1T_1$ absorption band e.g. with 514 nm of an Ar^+ - laser at temperatures below 50 K produces the metastable HS-LIESST state quantitatively. Treatment of the compound in the HS-LIESST state with red light (e.g. 752 or 799 nm), i.e. the ${}^5T_2 \rightarrow {}^5E$ excitation, leads to the LS form with a steady state value of $\gamma_{\text{LS}} \approx 0.9$ [HAU91].

The compound $[\text{Zn}(\text{ptz})_6](\text{BF}_4)_2$ is isostructural to the high temperature phase of $[\text{Fe}(\text{ptz})_6](\text{BF}_4)_2$. Because Zn is very similar in size to the Fe ion in the HS state and the metal-ligand distance is approximately the same for Zn-N and $\text{Fe}^{\text{HS}}\text{-N}$, $[\text{Zn}(\text{ptz})_6](\text{BF}_4)_2$ is a good reference system for comparing the vibrations of the crystal in both spin states.

4.2 Former vibrational measurements

From temperature dependent FT-FIR spectra both *Franke et al.* [FRA82] and *Müller et al.* [MÜL83] assigned the infrared active T_{1u} stretching mode of the octahedral molecule to 227 cm^{-1} (HS) and 413 cm^{-1} (LS) due to the temperature dependence of the intensity of these modes in a polyethylene pellet. However, in these spectra other bands arise or decrease as well, so that for an unequivocal assignment of the iron-nitrogen stretching vibration, isotope labelled compounds should be measured. The influence of temperature on the bands of the spectra makes a comparison of molecular vibrational properties at different temperatures difficult. This difficulty can be overcome by comparing the LS with the light-induced metastable LIESST state at the same temperature. In order to avoid matrix influences of e.g. CsI or polyethylene pellet material or influences from grinding, pressing etc. measurements on single crystals are preferred. This has been realised and is presented in the next chapter.

Polarised Raman measurements at low temperatures on single crystals of $[Fe(ptz)_6](BF_4)_2$ in LS and HS-LIESST state and of $[Zn(ptz)_6](BF_4)_2$ were not sufficient to identify the totally symmetrical A_{1g} stretch [HOE95]. For comparison with the calculations in chapters 4.6 and 4.7 and a further discussion these spectra are plotted in figures 4.2 and 4.3.

A comparison of the spectra of the HS state and the corresponding zinc system reveals some changes in the $130 - 210\text{ cm}^{-1}$ region. All other bands are more or less identical in the Zn and the HS spectra. Therefore, the observed changes must be connected to the metal-nitrogen bond. But the shift to higher energies of the modes when going from HS to Zn does not fit the expectations. The heavier central atom and a less strong metal-ligand bond (see chapter 4.6) should shift the Zn-N vibrations to lower energies compared to the HS vibrations.

The LS spectra in this region resemble very much the HS spectra. No band that is present in the HS spectra is absent in the LS spectra. Only two additional modes occur at 236 cm^{-1} and 312 cm^{-1} in the spectra of the LS state.

Therefore, a definite assignment of the Raman active metal-ligand vibrations was not possible.

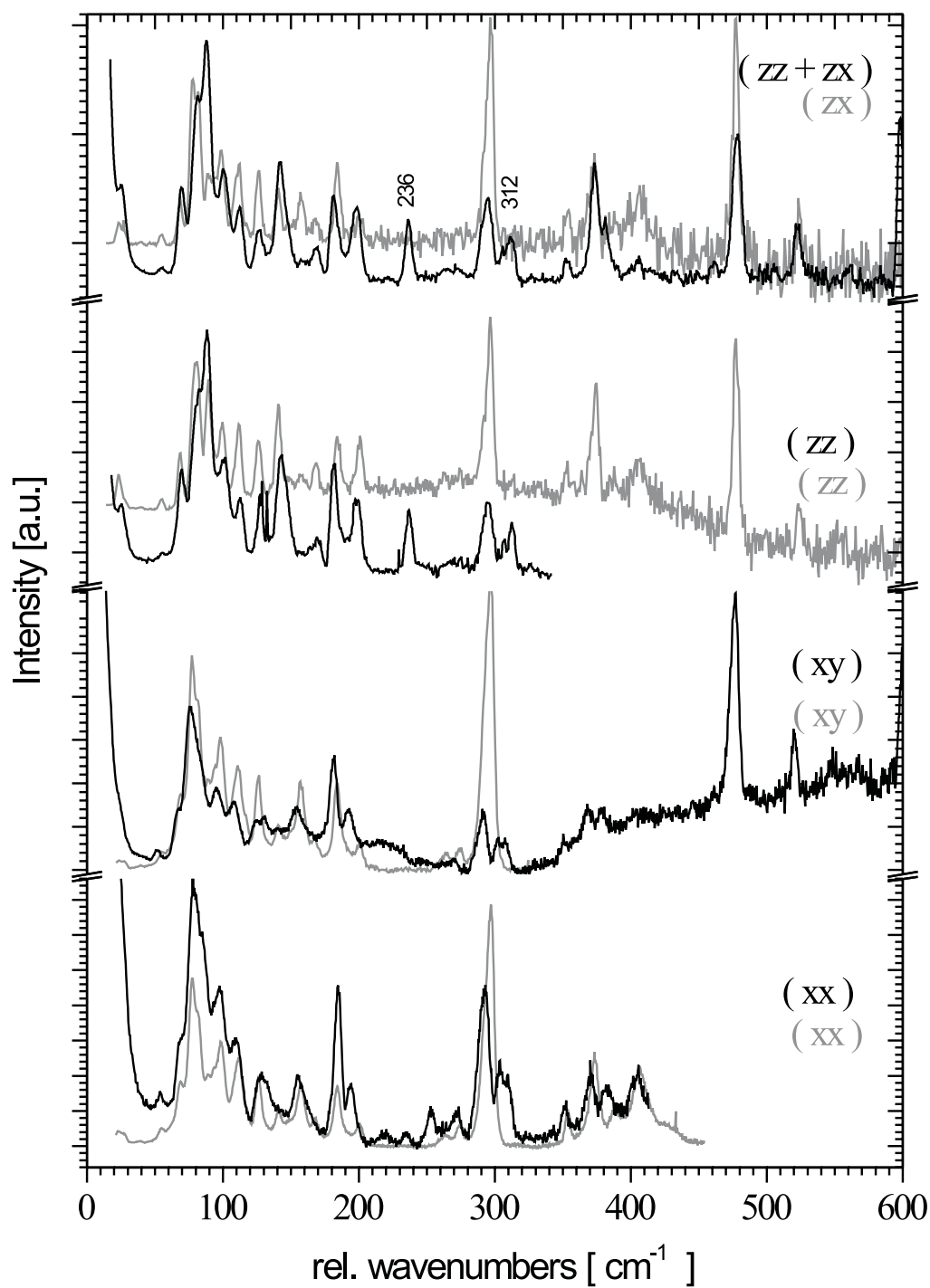


Figure 4.2: Polarised Raman spectra of $[\text{Fe}(\text{ptz})_6](\text{BF}_4)_2$ in HS-LIESST (grey) and LS (black) state at 10 K [HOE95].

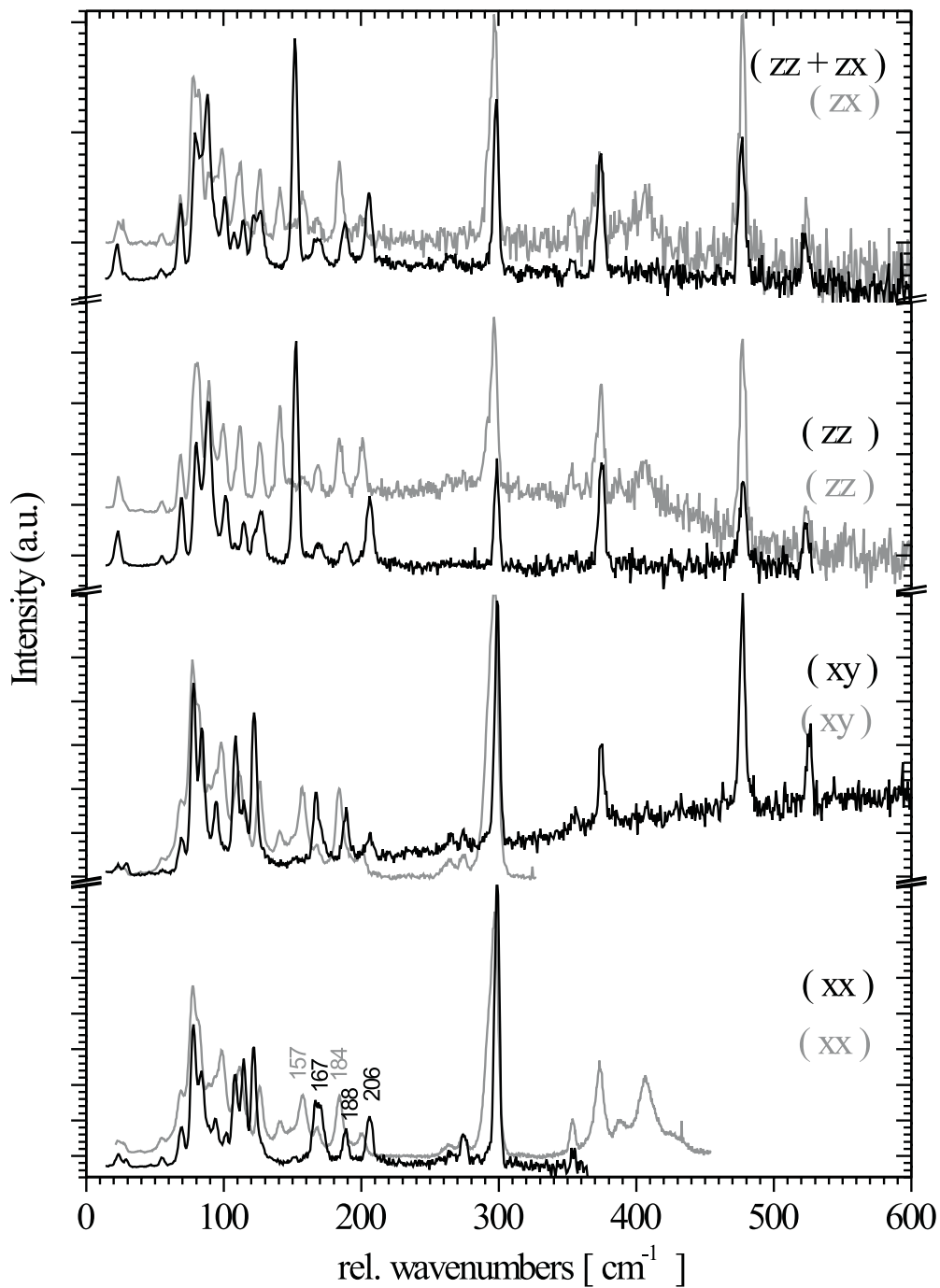


Figure 4.3: Polarised Raman spectra of HS - $[\text{Fe}(\text{ptz})_6](\text{BF}_4)_2$ (grey) and $[\text{Zn}(\text{ptz})_6](\text{BF}_4)_2$ (black) at 10 K [HOE95].

4.3 Single crystal FIR spectra on labelled complexes

In contrast to the Raman spectra [HOE95], the FIR spectra reveal quite a few differences between the HS and the LS state [FRA82, MÜL83]. In order to unequivocally assign the infrared active metal-ligand stretching mode, the T_{1u} mode in octahedral symmetry, the isotope substitution method has been employed. The complexes $[M^{II}(\text{ptz})_6](\text{BF}_4)_2$ have been synthesised with $M^{II} = {}^{54}\text{Fe}$, ${}^{56}\text{Fe}$, ${}^{64}\text{Zn}$, and ${}^{68}\text{Zn}$. The vibrations originating from the two T_{1u} symmetry modes (denominated as ‘ T_{1u} ’- modes in the following) are expected to show a slight energetic shift, because these two normal modes move the metal-center. The isostructural zinc complex may be considered as an additional heavy isotope of the iron complex in the high-spin state, since the zinc complex has nearly the same lattice parameters and metal-ligand bond lengths.

Single crystals have been obtained even from the small amounts of sample of the ${}^{54}\text{Fe}$, ${}^{56}\text{Fe}$, ${}^{64}\text{Zn}$, and ${}^{68}\text{Zn}$ complexes. After cleaving along the hexagonal *ab*-plane the samples were thin enough for FT-IR transmission experiments. For a direct comparison of the HS and LS spin states in the same lattice and at the same temperature the LIESST state was produced by irradiation of the iron complex with green laser light with $\lambda = 514$ nm at 30 K. The FIR spectra (100 - 550 cm^{-1}) of the ${}^{54}\text{Fe}$ and ${}^{56}\text{Fe}$ complexes in HS and LS state in comparison with the spectra of the two zinc complexes are shown in figure 4.4.

The only difference between the zinc and the HS spectra is the mode at **191 cm^{-1}** (${}^{68}\text{Zn}$), 195 cm^{-1} (${}^{64}\text{Zn}$) that shifts to **234 cm^{-1}** (${}^{56}\text{Fe}$), 237 cm^{-1} (${}^{54}\text{Fe}$). It is the only mode sensitive to isotope substitution in the zinc and HS spectra, as well. This vibration, therefore, must be assigned to the infrared active ‘ T_{1u} ’ stretching mode. The apparent change in band width in the ${}^{54}\text{Fe}$ spectrum is only due to different thicknesses of the samples: despite a satisfactory transmittance of the crystals most of the bands are saturated. Care has to be taken when looking at intensities. The shift of the ‘ T_{1u} ’ vibration between zinc and HS has no influence on the remaining modes. All other modes stay constant within 1 cm^{-1} . The LIESST state spectrum of the ${}^{54}\text{Fe}$ complex still contains some residual LS.

The LS spectrum is not that similar to the HS spectrum: some small changes occur in the very low frequency range [$\lesssim 100$ cm^{-1} , i.e. 33, 53, 61, 81, 98 and 105 cm^{-1} (HS) and 38, 60, 68, 76, 87 and 105 cm^{-1} (LS), respectively]. These are attributed to bends of the octahedron as well as lattice modes and ligand torsions and frozen rotations (librations). The major differences between the HS and LS spectra are as follows:

The bands at 128, 162 and 260 cm^{-1} (HS) probably shift to 153, 202 and 265 cm^{-1} (LS). The mode at 236 cm^{-1} probably stems from a shift downwards of the 295 cm^{-1} (HS) vibration that is of only low intensity at 297 cm^{-1} in the LS state. A similar observation has been made in the Raman spectra [HOE95]. The 236 cm^{-1} (LS) band only accidentally coincides with the metal-ligand stretch in the HS complex.

The LS spectra reveal **two bands showing an isotope effect**, namely **359 cm^{-1}** (${}^{56}\text{Fe}$, 361 cm^{-1} for ${}^{54}\text{Fe}$) and **413 cm^{-1}** (${}^{56}\text{Fe}$, 416 cm^{-1} for ${}^{54}\text{Fe}$). This is in disagreement with the expectation

from a simple octahedral molecule of only one isotope-sensitive vibration in the iron-nitrogen stretching regime. In this region the band at 374 cm^{-1} in the HS state is not present in the LS spectra. The zinc spectrum shows this band at the same position as the HS complex, despite a change in the metal-nitrogen bond strength. The vibration is also present in the spectrum of the pure ligand (fig. 4.6) and, therefore, has to be assigned to an intra-ligand vibration. From this consideration a large shift of this mode in the LS complex is not expected. The ‘missing’ band and the presence of two isotope sensitive modes can be understood in terms of a larger coupling between this intra-ligand mode and the Fe-N-stretch in the LS state. But to clearly prove this, one has to examine the assignments of the normal modes based on normal mode calculations (NCA, DFT) presented in chapters 4.6 and 4.7.

The peak at 474 cm^{-1} (HS) moves to 488 cm^{-1} (LS). The BF_4^- anion bending mode at 524 cm^{-1} [QUI71] (see also chapter 4.6.1) remains in that position in all spectra.

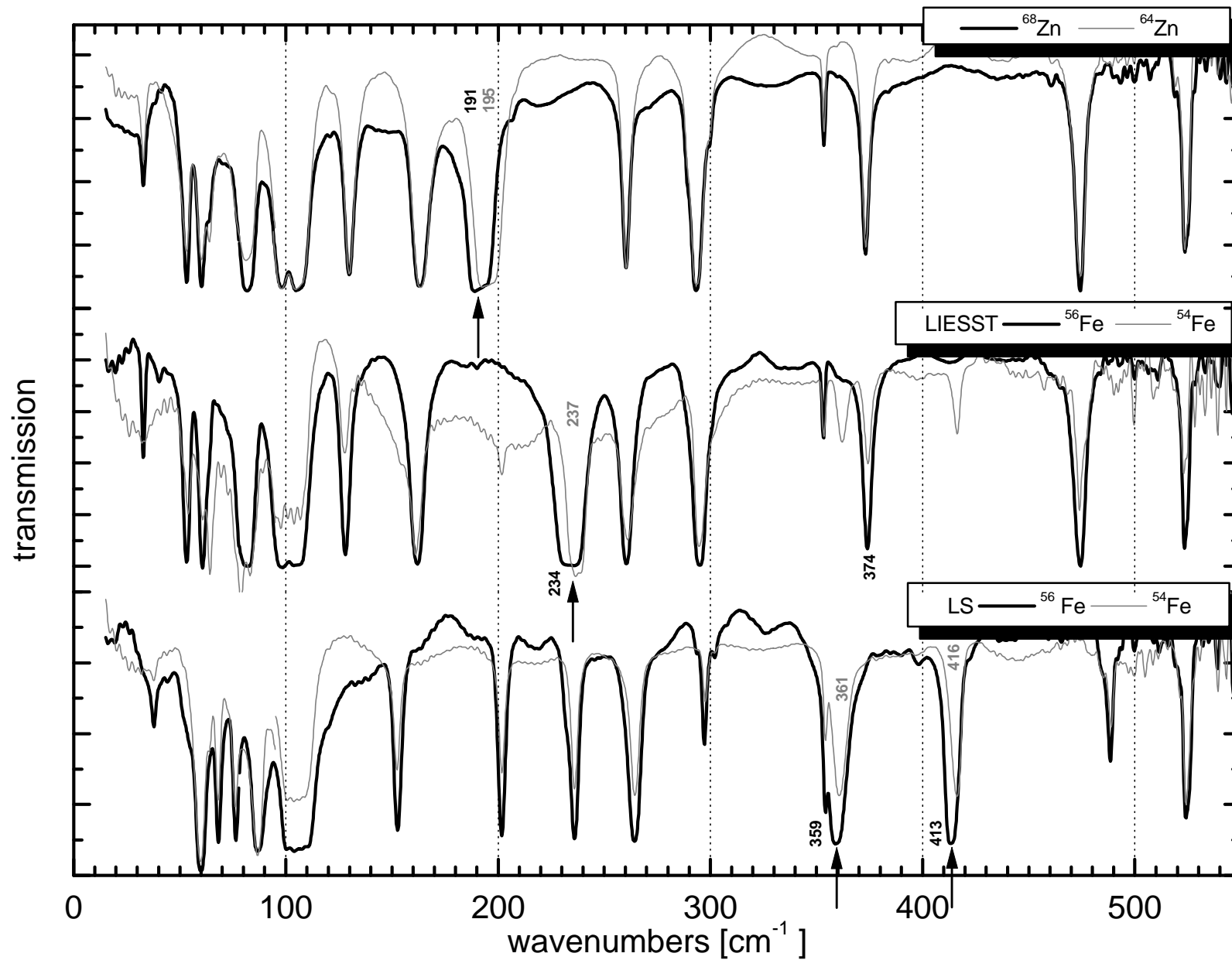


Figure 4.4: Isotope labelled single crystal FT-FIR spectra of $[M^{II}(\text{ptz})_6](\text{BF}_4)_2$ at 30 K (arrows indicate isotope shifts).

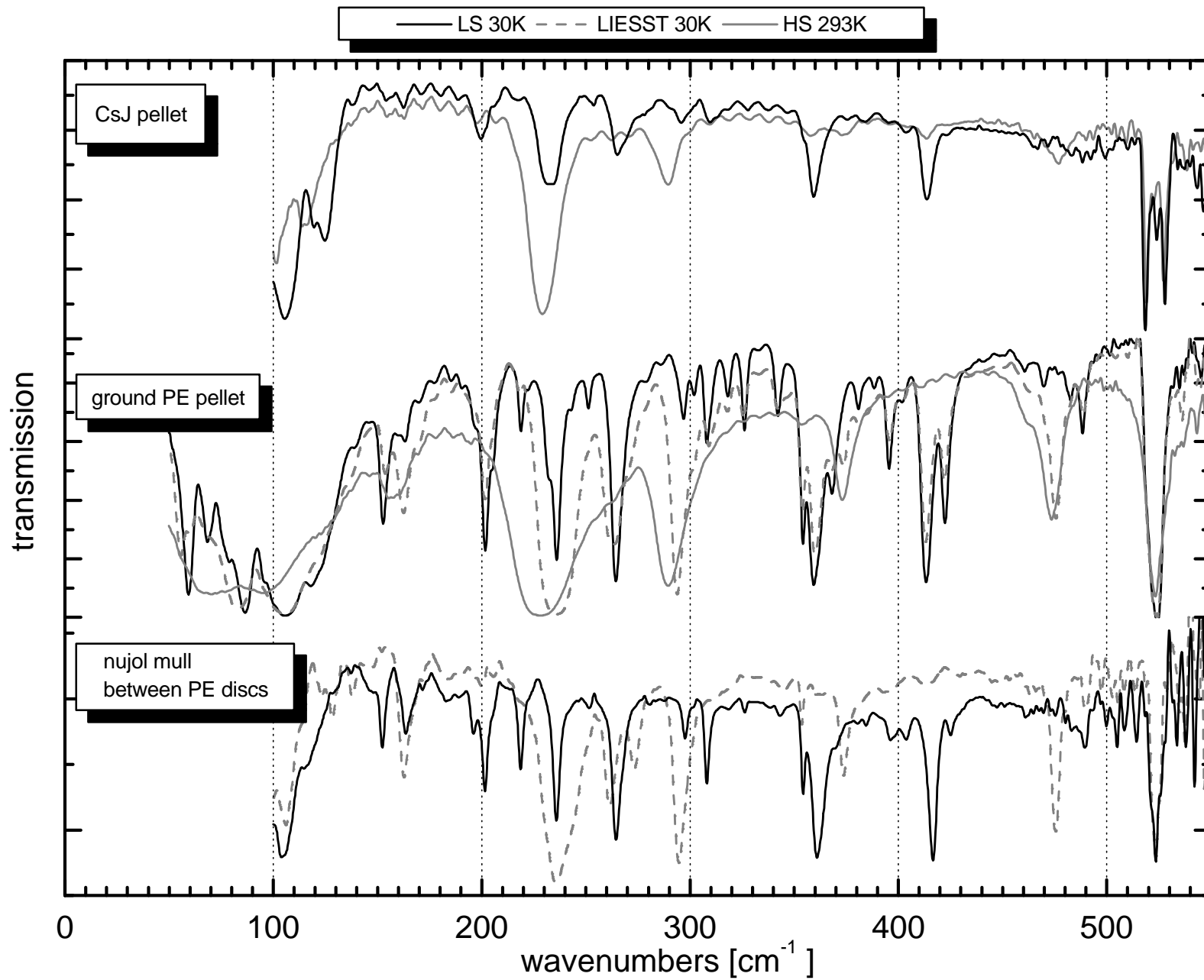


Figure 4.5: $[\text{Fe}(\text{ptz})_6](\text{BF}_4)_2$ FIR spectra as CsI- and PE pellets and nujol mull between PE discs at 30 K.

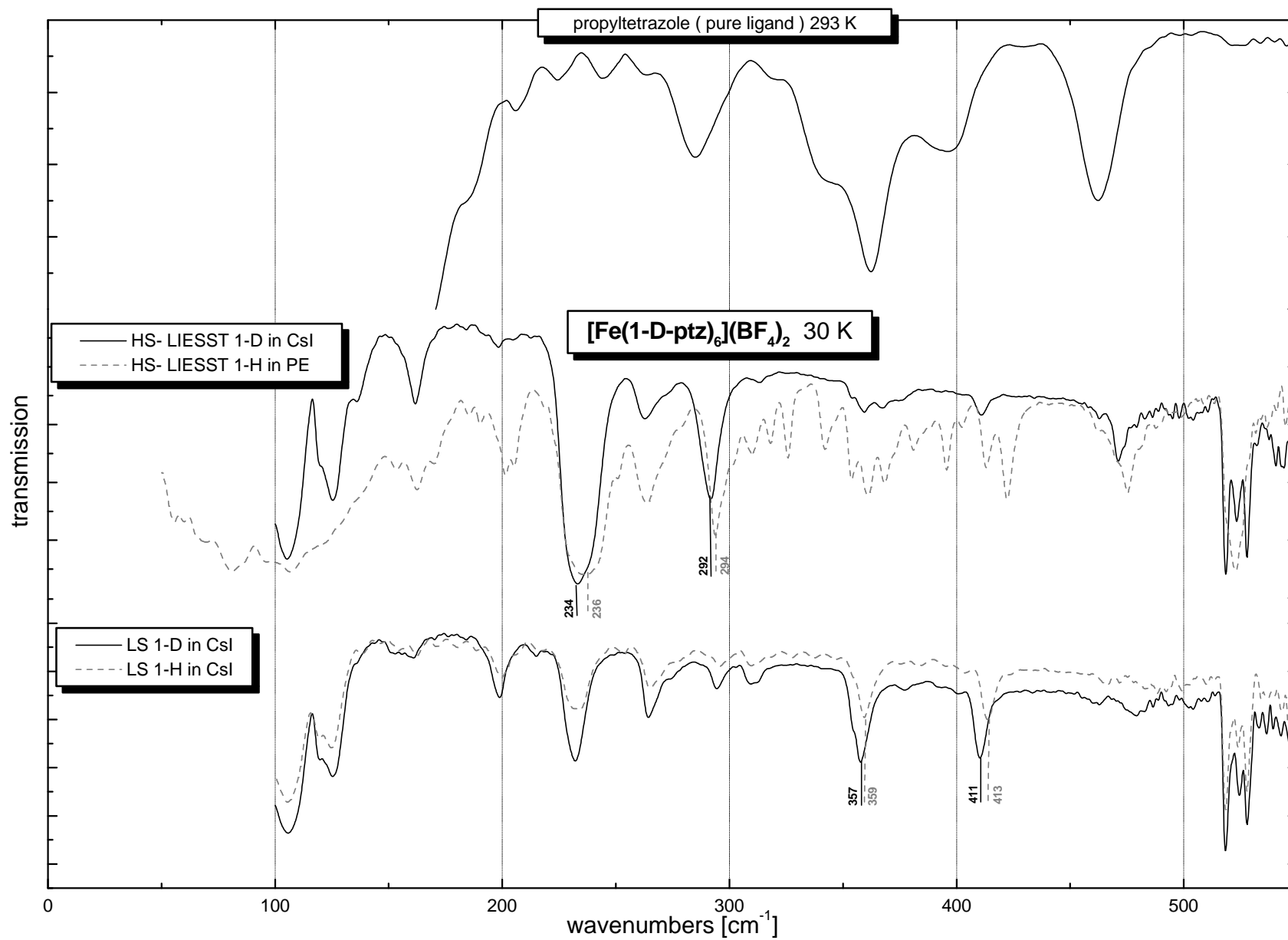


Figure 4.6: FIR spectra of $[\text{Fe}(1\text{-D-ptz})_6](\text{BF}_4)_2$ in comparison with the unlabelled complex and the pure ligand propyltetrazole.

All other compounds presented in chapters 5 - 8 and the deuterated $[\text{Fe}(1\text{-D-ptz})_6](\text{BF}_4)_2$ presented below are only available as powder samples. In order to allow an appropriate comparison with the spectra presented so far, the spectra of $[\text{Fe}(\text{ptz})_6](\text{BF}_4)_2$ have been recorded embedded in CsI- and polyethylene pellets as well as in a nujol mull between PE disks. These are presented in figure 4.5:

Most of the spectral differences between high spin and low spin state above 100 cm^{-1} can be seen as well. The ground sample in polyethylene shows some splitting of the peaks due to the change in the lattice affected by the mechanical treatment. The LIESST experiment is incomplete in the PE case showing some residual LS. The lines in the CsI pellet are broadened and the bands between $130\text{-}165\text{ cm}^{-1}$ which are well visible in the other matrices are missing or are of very low intensity. This may be attributed to the fact that the CsI pellet is more a solid solution than the sample in the other surroundings. This leads to the absence of the lattice modes and other vibrations which are connected to the solid state.

Comparing these spectra with those of the single crystals makes clear that one really has to care about the sample preparation when interpreting infrared data. For powder samples a nujol mull between PE disks resembles the single crystal data most. One general problem that arises with pellets in FT-IR spectroscopy is a periodical background especially below 300 cm^{-1} . It is due to the interference of the internally reflected IR light between the plane parallel surfaces of the pellet. This might be overcome by the preparation of wedge-shaped pellets [KNÖ71], but there are no standard tools for doing so.

For further assistance on the assignments made so far, the FIR spectra of the pure ligand propyltetrazole (liquid between PE discs) and the isotope labelled iron-complexes with deuterium at the ring hydrogen position (obtained as powder out of EtOD) have been measured and are presented in figure 4.6:

The ligand spectrum (with its bands at $285, 342, 362, 396,$ and 463 cm^{-1}) indicates that at least the modes at $295, 354, 374,$ and 474 cm^{-1} (HS) and 488 cm^{-1} (LS) in the single crystal spectra of the iron complex are **intra-ligand vibrations**, which nevertheless might shift slightly between HS and LS state.

The deuterated compound reveals small isotope shifts of about 2 cm^{-1} for the bands which appear at 236 and 294 cm^{-1} (HS-LIESST) and 359 and 413 cm^{-1} (LS) in the non-deuterated samples. Besides the metal-nitrogen stretch, which is expected to show such an effect when changing the mass of a more or less rigid ligand, the vibration at 294 cm^{-1} , which does not show an effect on metal isotope substitution, should be connected to an intra-ligand motion.

Another system which can be used for comparison is the methyl substituted tetrazole system $[\text{Fe}(\text{mtz})_6](\text{BF}_4)_2$ (mtz = 1-methyl-tetrazole). The molecule itself is even simpler than the ptz one, but the crystal symmetry is lower thus showing two different lattice sites [WIE93] and a thermal spin crossover only at the iron atom in one site, leading to a γ_{HS} value of 0.5 at low temperatures ($T_{1/2} = 75\text{ K}$). However, by means of irradiation with green or red light, both sites can be converted into HS or LS state, respectively [POG90], with a steady state value after

reverse-LIESST of about $\gamma_{LS} \approx 0.7$. The corresponding single crystal FIR spectra are shown in figure 4.7.

In the range below 150 cm^{-1} they are not that good as the analogue $[\text{Fe}(\text{ptz})_6](\text{BF}_4)_2$ spectra, because of a less nice crystal quality. Nevertheless, the peak patterns above 150 cm^{-1} in HS and LS state look very similar to those in $[\text{Fe}(\text{ptz})_6](\text{BF}_4)_2$. In analogy, the infrared active 'T_{1u}' iron-nitrogen stretch is assigned to the modes at **223 / 236 cm^{-1}** (HS) and **$\sim 356 / 423 / 426 \text{ cm}^{-1}$** (LS). So, the coupling in LS state with the former (i.e. in HS state) intra-ligand mode at 373 cm^{-1} is a bit stronger, leading to a slightly larger splitting of the resulting vibrations. Additionally, a splitting of the modes according to the lower site-symmetry is observed. The fact that the intra-ligand mode at 373 cm^{-1} in $[\text{Fe}(\text{mtz})_6](\text{BF}_4)_2$ is practically at the same position as in $[\text{Fe}(\text{ptz})_6](\text{BF}_4)_2$ in the HS state shows that the length of the alkyl-chain is of minor importance for this vibration.

The band at 295 cm^{-1} that strongly loses intensity in the ptz system when going from HS to LS is not present in the mtz system in the HS state but at $292 / 297 \text{ cm}^{-1}$ for the LS complex. So this vibration might be connected to the alkyl rest of the ligand. This also holds for the mode at 474 cm^{-1} (HS) and 488 cm^{-1} (LS) in ptz, that is completely absent in the mtz spectra. Due to the smaller ligand mass the modes at 162 and 261 cm^{-1} (HS) or 153 and 202 cm^{-1} (LS) in the ptz complex shift to 171 and $270 / 280 \text{ cm}^{-1}$ (HS) or 167 and $200 / 208 \text{ cm}^{-1}$ (LS) in the mtz compound. Additionally, most vibrations in $[\text{Fe}(\text{mtz})_6](\text{BF}_4)_2$ are split according to the lower site-symmetry.

DFT and NCA calculations in chapters 4.6 and 4.7 have to be taken into account for further enlightenment of the low-frequency assignments.

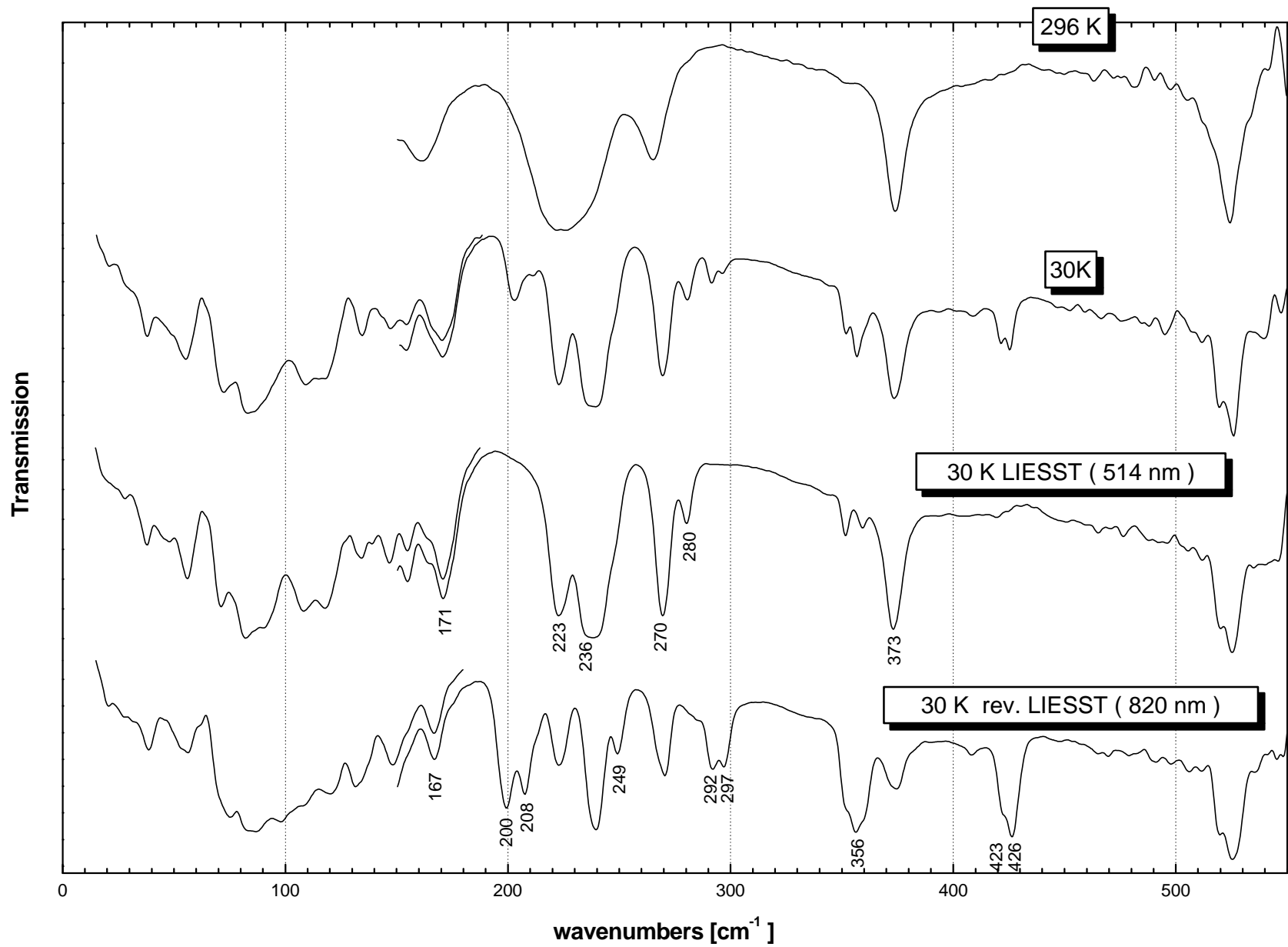


Figure 4.7: Single crystal FIR spectra of $[\text{Fe}(\text{mtz})_6](\text{BF}_4)_2$ at 296 K and 30 K before and after irradiation with 514 or 820 nm.

4.4 Middle infrared spectra

In figure 4.8 the single crystal MIR data of $[M(\text{ptz})_6](\text{BF}_4)_2$ with $M = \text{Fe}$ and Zn are shown. Whereas the HS and the isostructural Zn system are practically identical in the MIR, the two different spin states slightly vary in only a few modes: mainly the bands at 909, 1002, and 1023 cm^{-1} (HS) vanish for the benefit of those at 944, 982, 1006, 1017, and 1029 cm^{-1} (LS). The peaks at $\sim 1200 \text{ cm}^{-1}$ and $\sim 1300 \text{ cm}^{-1}$ change their intensity ratios and therefore the shape of their envelope. The bands at 1550, 1580, 1625, and 1789 cm^{-1} gain some intensity when going from HS to LS state.

In the next figure (4.9) besides the spectrum of the pure ligand propyltetrazole, a comparison between the deuterated and the unlabelled iron complex both as CsI pellets in both spin states is depicted. One can clearly see the mass effect of deuteration on quite a few vibrations (the 1-D compound still contains some amount of natural hydrogen):

The C-H stretch at 3093 / 3146 cm^{-1} shifts to 2314 / 2348 cm^{-1} on deuteration of the HS complex at ambient temperatures. Other observable shifts which occur are 1508 \rightarrow 1490 / 1477 cm^{-1} , 1440 \rightarrow 1411 cm^{-1} , 997 \rightarrow 875 / 856 cm^{-1} and 675 \rightarrow 589 cm^{-1} for the HS compound. Because of these rather large shifts those vibrations must be connected to movements of the H/D atom, i.e. C-H in-plane and out-of-plane bending vibrations or ring modes with a partial movement of the H/D atom. These modes are only slightly modified in the LS state at 30 K.

In figure 4.10 the single crystal MIR spectra of $[\text{Fe}(\text{mtz})_6](\text{BF}_4)_2$ at 30K before and after LIESST and rev. LIESST are compared with those of $[\text{Zn}(\text{etz})_6](\text{BF}_4)_2$ (which contains one more CH_2 group in the alkyl chain). Only very few slight changes at ~ 900 , 1250 and 1800 cm^{-1} can be found between the HS (LIESST) and the mere LS state (rev. LIESST), similar to the shifts observed in the propyl tetrazole complexes. The peak pattern at around 1800 cm^{-1} must be due to overtones and combinations, possibly of a fundamental in the very intense band envelope between 1000 - 1100 cm^{-1} .

The ethyl tetrazole complex $[\text{Zn}(\text{etz})_6](\text{BF}_4)_2$ reveals some additional vibrations at ~ 800 , 960, and between 1300-1400 cm^{-1} , because of further bending modes of the extended alkyl chain and the influence of the larger mass of the alkyl rest on the ring modes. This is even more pronounced in the $[M(\text{ptz})_6](\text{BF}_4)_2$ spectra with another additional chain link (cf. figure 4.8).

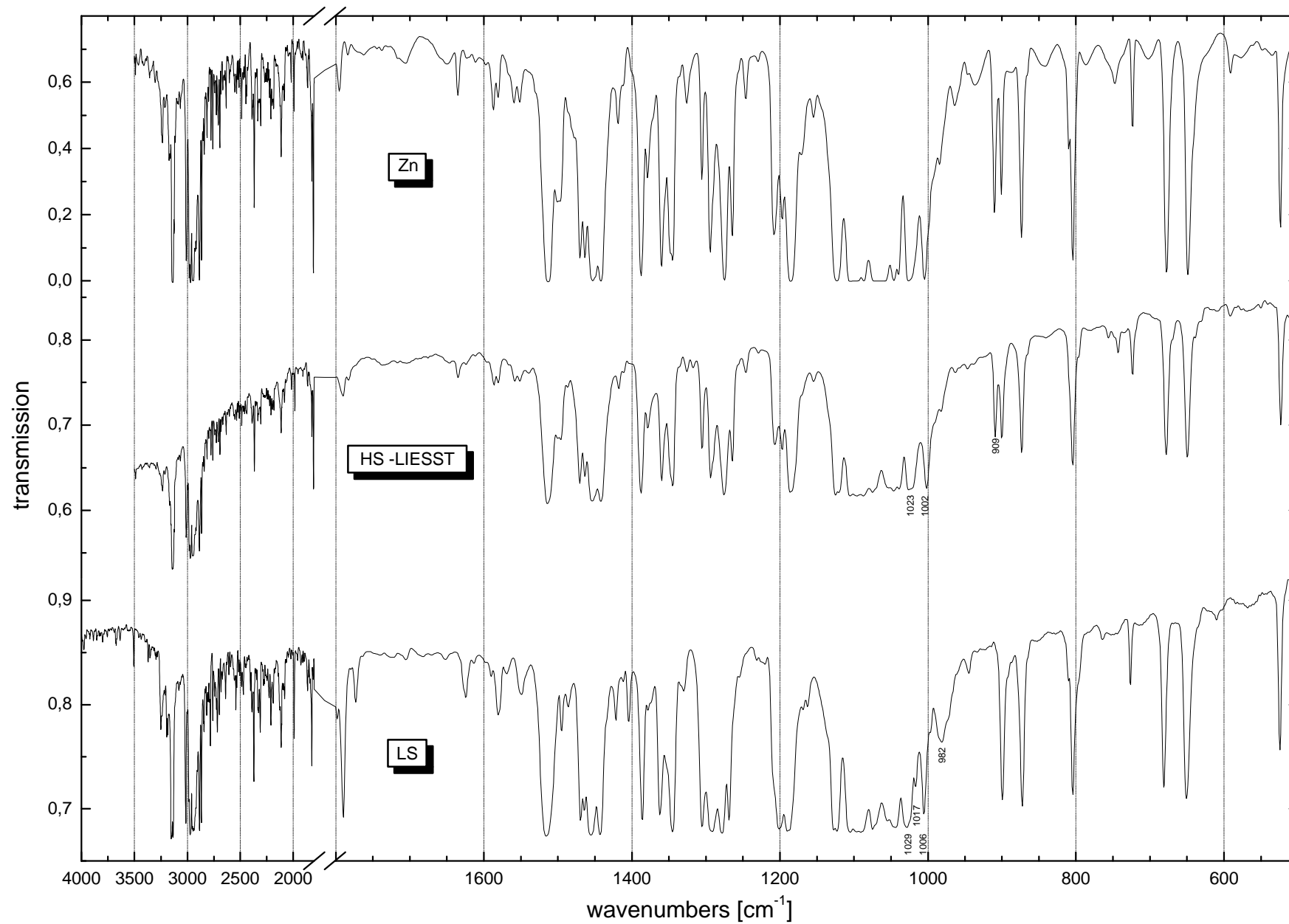


Figure 4.8: Single crystal FT-MIR spectra of $[M^{II}(\text{ptz})_6](\text{BF}_4)_2$ at 30 K.

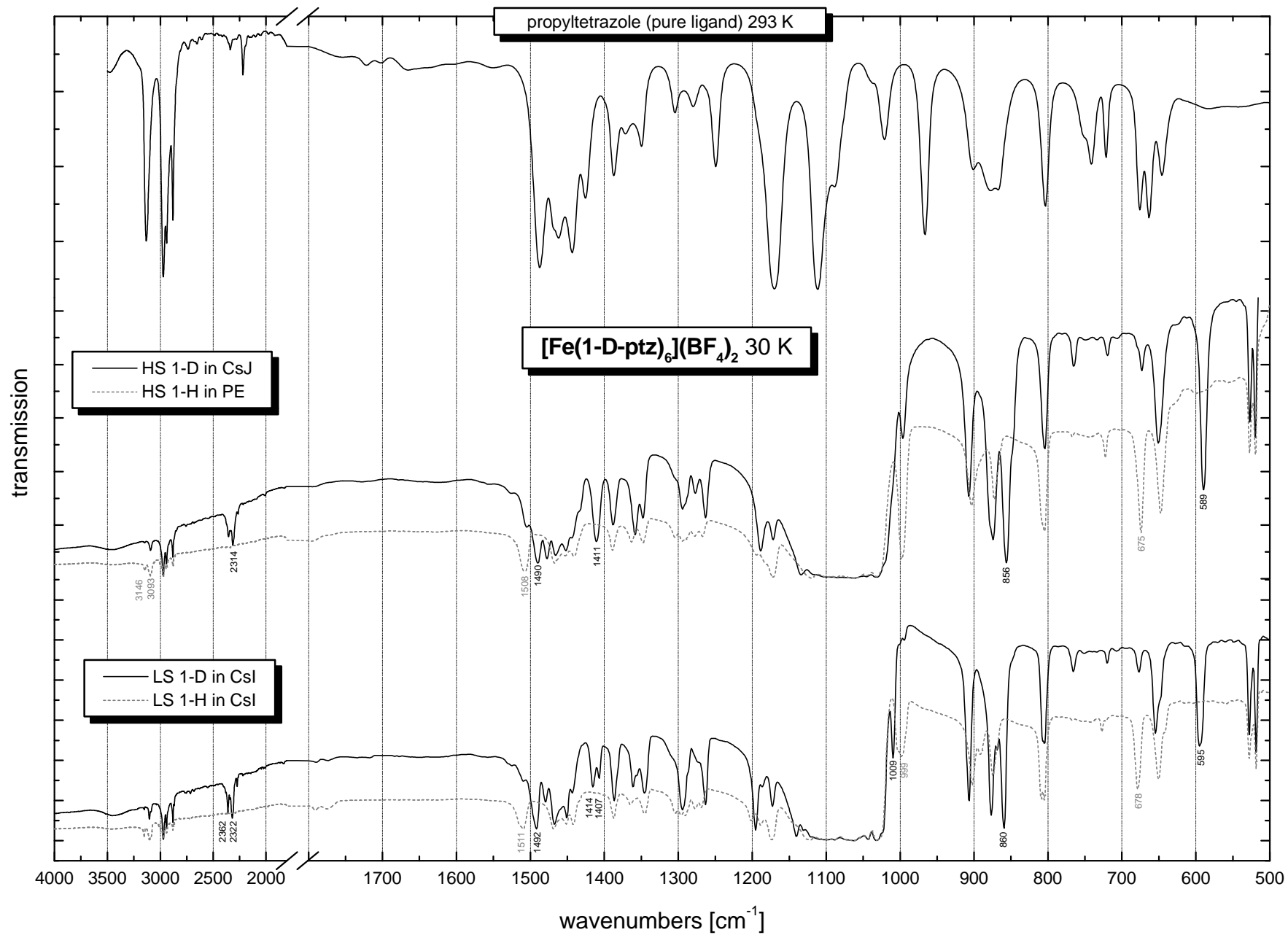


Figure 4.9 : MIR spectra of $[\text{Fe}(1\text{-D-ptz})_6](\text{BF}_4)_2$ in comparison with the unlabelled complex and the pure ligand propyltetrazole.

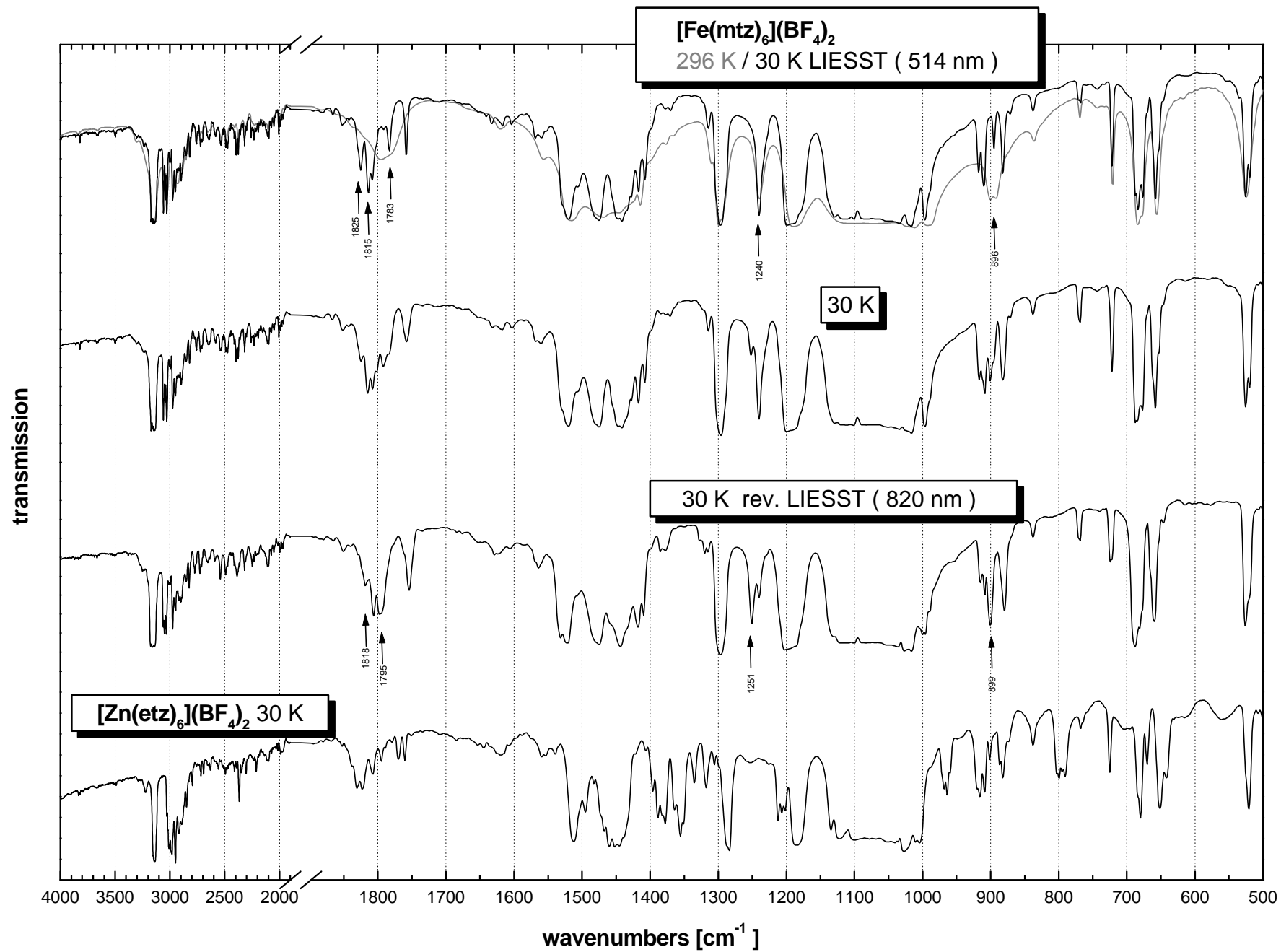


Figure 4.10: Single crystal MIR spectra of $[\text{Fe}(\text{mtz})_6](\text{BF}_4)_2$ before and after LIESST and rev. LIESST in comparison with $[\text{Zn}(\text{etz})_6](\text{BF}_4)_2$.

4.5 Raman spectra of $[\text{Fe}(\text{mtz})_6](\text{BF}_4)_2$

In order to assign the totally symmetric stretch in the Raman spectra of $[\text{Fe}(\text{ptz})_6](\text{BF}_4)_2$ [HOE95] the light scattering of $[\text{Fe}(\text{mtz})_6](\text{BF}_4)_2$ with an excitation wavelength of 514 nm at 200, 60 and 10 K has been observed. This should correspond to the thermal HS (200 K), hopefully about 50% LS (60 K) and a pure HS-LIESST state (10 K). There remains an uncertainty about the values of γ_{HS} at the different temperatures, because no probe vibration is known for this system to determine the HS fraction.

These spectra are depicted in figure 4.11:

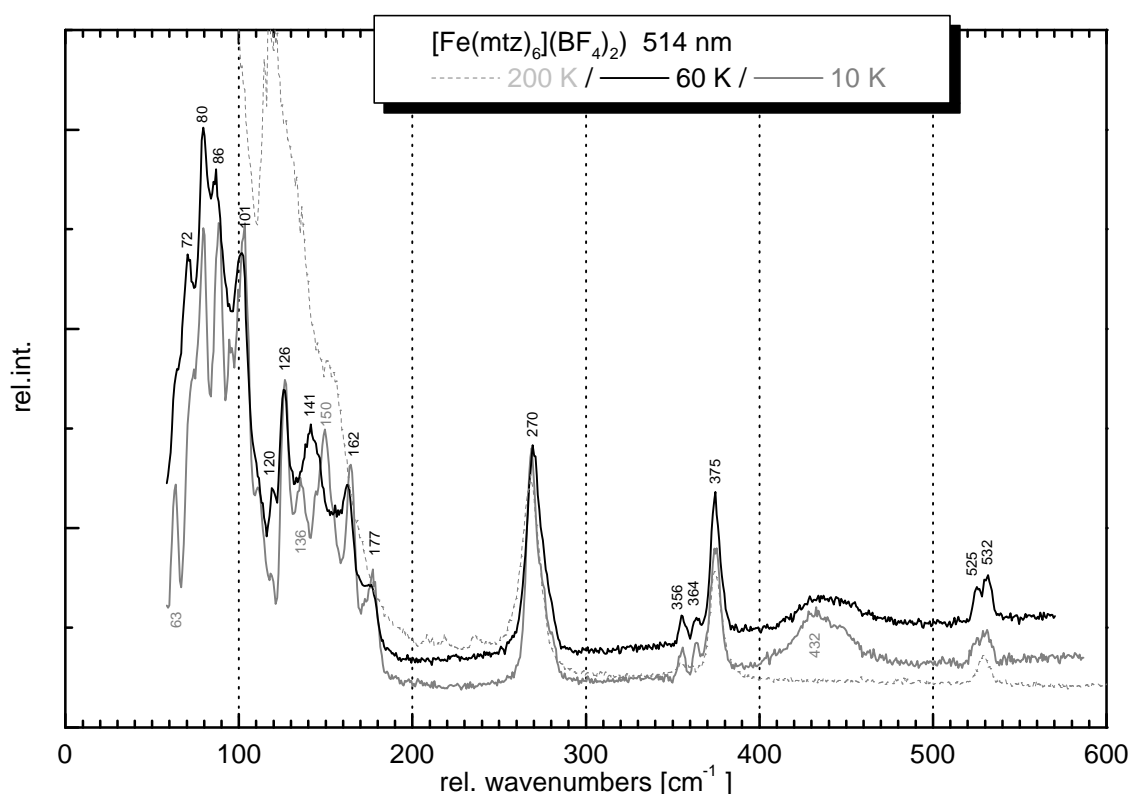


Figure 4.11: Low frequency Raman spectra of $[\text{Fe}(\text{mtz})_6](\text{BF}_4)_2$ at 200, 60 and 10 K.

The only striking difference is a peak at 141 cm^{-1} stemming from the LS state compared to the two bands at 136 and 150 cm^{-1} in the HS-LIESST state. The mode at 432 cm^{-1} at 10 K is entirely missing in the spectrum of the thermal HS.

Figure 4.12 shows the high frequency Raman spectra of $[\text{Fe}(\text{mtz})_6](\text{BF}_4)_2$ at the three different temperatures, revealing no differences in the $600 - 2000 \text{ cm}^{-1}$ region.

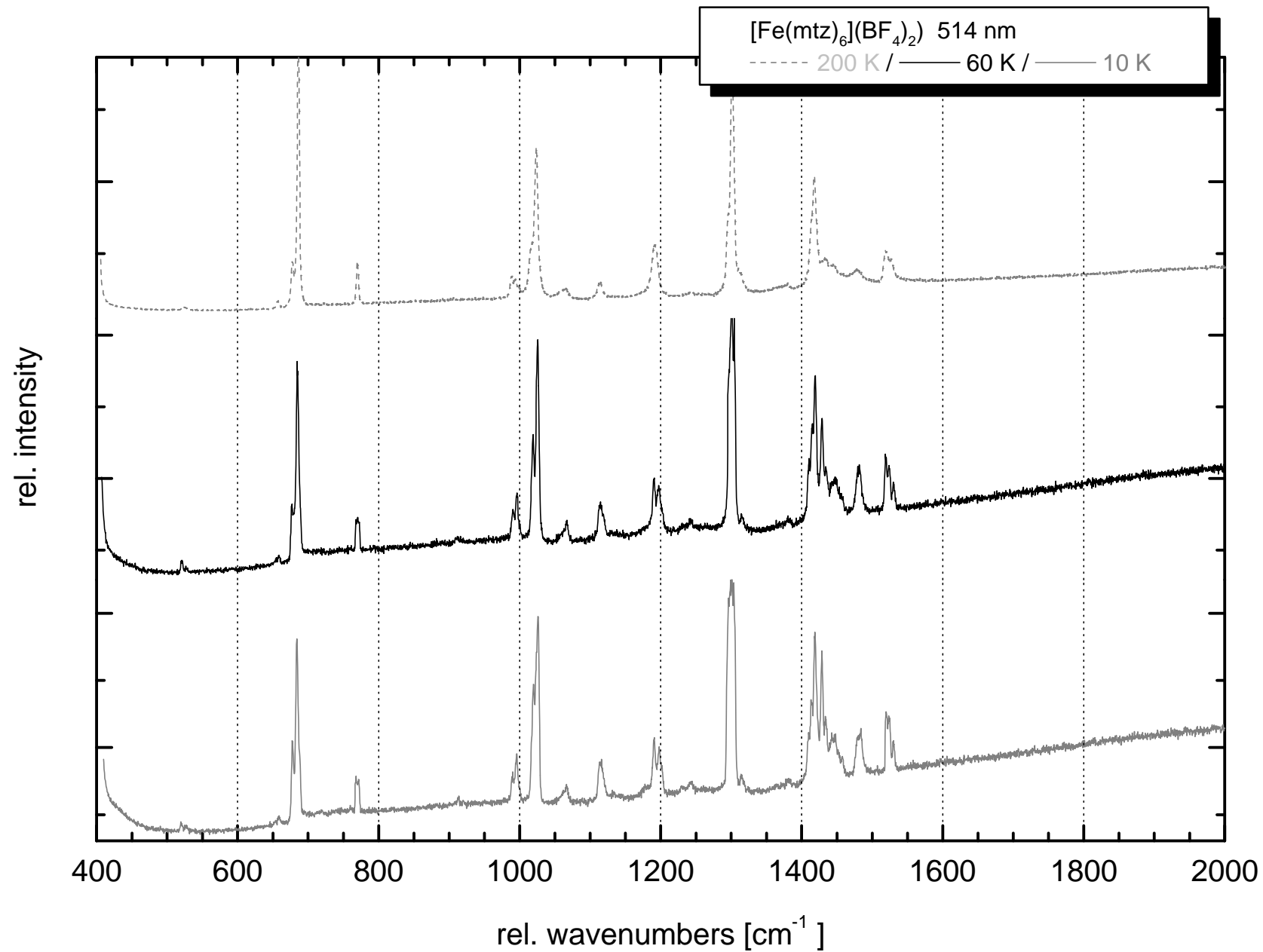


Figure 4.12: High frequency Raman spectra of $[\text{Fe}(\text{mtz})_6](\text{BF}_4)_2$ at 200, 60 and 10 K.

4.6 Density functional calculations

In this section density functional calculations on different systems are presented. First of all, the anion BF_4^- is calculated to compare the vibrational frequencies with the experimental ones and to demonstrate the accuracy of the employed method. Afterwards the simple octahedral complex molecule $[\text{M}(\text{NH}_3)_6]^{2+}$ and the pure organic ligand are calculated. At the end of this chapter the results of the calculation of two different larger models of the real system including two tetrazole ligands in trans position are presented.

The results, which are taken from the GAUSSIAN output files, are the optimized structural data, the vibrational frequencies of the normal modes and their eigenvectors, and different thermodynamic data. The thermodynamic data include the electronic energy $E(\text{B}+\text{HF-LYP})$, the Zero-point-vibrational energy and the electronic and vibrational component of the entropy. For comparison of the HS and the LS state of a calculated model the electronic energy and the Zero-point-vibrational energy are summed up to show the energy difference of the two spin states at 0 K. The entropy values for the complex molecule containing tetrazole ligands are given at the transition temperature of the $[\text{Fe}(\text{ptz})_6](\text{BF}_4)_2$ system of ~ 130 K, otherwise at the default temperature of 298.15 K.

The force constants in the tables are obtained by transformation of the force field from cartesian coordinates to self-defined internal coordinates with the use of the program REDONG, as explained in chapter 2.

4.6.1 The anion BF_4^-

The anion BF_4^- with its T_d symmetry has four vibrational modes with the A_1 and E ones being Raman and the two T_2 modes IR active, respectively. These modes have been calculated with the B3LYP functional and two different basis sets (LanL2DZ and 6-31G*). The results are compared with some experimental data in table 4.1. The atom displacement vectors of the resulting normal modes are plotted in figure 4.13.

mode	calculated		experimental		
	LANL2DZ	6-31G*	[QUI71]	$[\text{Fe}(\text{ptz})_6](\text{BF}_4)_2$ [this work / HOE95]	NaBF_4 [HOE95]
$\nu_s (A_1) (\text{R})$	701	763	777	770	784
$\nu_d (T_2) (\text{IR})$	1060	1134	1070	~ 1070	~ 1050
$\delta_d (E) (\text{R})$	309	348	360	354	343/369
$\delta_d (T_2) (\text{IR})$	478	517	533	524	531/553
$r (\text{B-F})$	1.445 Å	1.41 Å		1.317 Å [WIE93]	

Table 4.1: Calculated and observed frequencies [cm^{-1}] and bond length of the BF_4^- -anion.

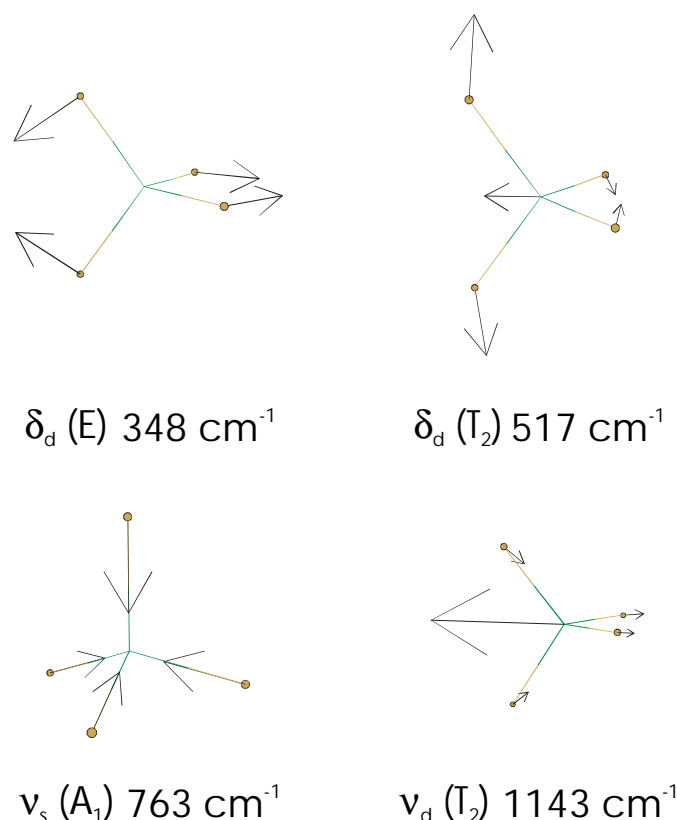


Figure 4.13: Eigenvectors of BF_4^- as calculated with B3LYP/6-31G*.

The calculated frequencies are in quite good agreement with the observed ones.

4.6.2 $[M(\text{NH}_3)_6]^{2+}$

The first model for an octahedral spin crossover system which has been calculated is the $[\text{M}(\text{NH}_3)_6]^{2+}$ system with $M = \text{Zn}$ and Fe in the HS and LS state. The geometry optimisations using C_1 symmetry led to stationary points with one (HS) or two (Zn) imaginary frequencies of about -35 cm^{-1} , i.e. a saddle point in the potential energy surface instead of a real minimum. The corresponding coordinates are connected to rotations of the NH_3 ligand along this very flat surface. The low imaginary frequencies (smaller than $\sim 50 \text{ cm}^{-1}$) can be neglected when looking at the vibrational properties of the octahedral MN_6 core, without loss of information [OCH99] (i.e. the geometry might be considered close enough to the minimum of the potential energy). Table 4.2 summarises the obtained results. The stated force constants belong to a force field with off-diagonal elements less than 17 % (HS, Zn) and less than 5 % (LS) of the corresponding diagonal elements, respectively. The thermodynamic values are given at 298.15 K.

The results of the thermodynamic data clearly show the HS state to be the ground state of this model complex ($\Delta E_{\text{HL}} = -59,05 \text{ kJ/mol} = -4934 \text{ cm}^{-1}$). The electronic component of the entropy is the spin-only value (i.e. for a $S = 2$ system, $S_{\text{elec.}} = k \ln 5$). The calculated bond length of the HS complex is a bit larger (i.e. $\sim 0.1 \text{ \AA}$) than the value from X-ray measurements

of 2.19 Å [NOY62]. Therefore, the calculated frequencies are somewhat lower than the experimental ones. Nevertheless, the vibrational results agree well with the experimental values and especially shifts (e.g. from Zn to HS or from HS to LS) can be considered as reliable outcomes.

$[M(\text{NH}_3)_6]^{2+}$	Zn	HS	LS	exp. [SCH76]		D_{HL}
				$[\text{Fe}(\text{NH}_3)_6]^{2+}$	$[\text{Zn}(\text{NH}_3)_6]^{2+}$	
E (B+HF-LYP) [H/particle]	-404.5517	-462.4048	-462.3882			-43.54 kJ/mol
Zero-point-vib. energy [kJ/mol]	607.8879	609.9009	625.4063			-15.51 kJ/mol
$S_{\text{elec.}}$ [cal/mol/K]	0	3.198	0			13.39 J/mol/K
$S_{\text{vib.}}$ [cal/mol/K]	58.39	62.455	53.439			37.75 J/mol/K
r (M-N) [Å]	2.29	2.3	2.11			
f [r(M-N)] [mdyn/Å]	0.53	0.6	1.02	0.7 (GVFF)	0.6 (GVFF)	
f [α (N-M-N)] [mdyn·Å]	0.22	0.29	0.58			
ν (A_{1g}) [cm^{-1}]	301	309	357	344		
ν (E_g) [cm^{-1}]	182	193/210	310			
ν (T_{1u}) [cm^{-1}]	253/258	275/290	364/373	315	300	

Table 4.2: Computational results and literature data on $[M(\text{NH}_3)_6]^{2+}$.

The infrared active T_{1u} stretching mode is slightly split due to a lower than octahedral symmetry. These calculations cannot explain the large splitting into two modes sensitive to metal isotope substitution, as observed in the low spin case of $[\text{Fe}(\text{ptz})_6](\text{BF}_4)_2$.

The calculated **factor of 1.7** between the HS and LS force constants of the metal-ligand bonds for this very simple model system is a first approach to the situation in a spin crossover complex. The different kind of bonding in a spin-crossover system, especially the additional d_{π} - p_{π} -backbonding, should result in a higher factor between the force constants of the HS and LS state.

More details on the obtained force field in internal coordinates are given in the NCA section (see chapter 4.7), where these results are compared to a force field of a more complex model system.

4.6.3 Propyl tetrazole (pure ligand)

In order to get first informations on the vibrational properties of the tetrazole ring calculations on the pure ligand itself have been performed. In Table 4.3 the results of the DFT calculations on methyl-tetrazole (mtz) and H-tetrazole (htz) using different kinds of basis sets are shown (for comparison of calculated geometries see appendix).

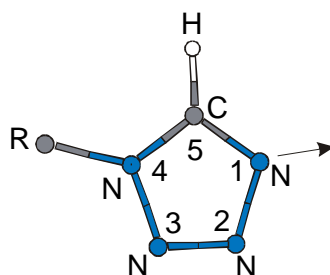


Figure 4.14: Numbering scheme of the tetrazole ring.

	assignment	mtz			htz	
		STO-3G	6-311G(d)	LanL2DZ	3-21G	LanL2DZ
1	CH3-Rot.	73	-29 !!	57	73	
2	4-R-oop	185	224	236	214	(742)
3	4-R-ip	315	357	348	331	
4	4-3/5 oop	572	665	656	641	655
5	4-R str.	670	692	673	645	(3703)
6	ring oop	640	734	701	681	703
7	5-H oop	828	851	857	777	857
8	1-2 str.	904	975	901	869	886
9	3-4 (+1-2) sym.str.	977	1006	948	907	959/993
10	2-1/3 str.	1050	1067	1030	1019	1023
11	C-H(R)/H-5 sym.ip	1083	1121	1084	1072	
12	2-3 str./H-5 ip	1154	1158	1157	1084	1134
13	CH (R) w ag	1176	1196	1164	1161	
14	CH (R) w ag + H-5 ip	1215	1261	1202	1192	1181
15	CH (R) w ag + ring breath	1308	1328	1254	1229	1230
16	5-1/5-4 sym.str.	1441	1437	1394	1376	
17	(CH3 (R) umbrella + H-5 ip) asym	1511	1464	1441	1408	(1386)
18	(CH3 (R) umbrella + H-5 ip) sym	1549	1507	1504	1499	(1466)
19	CH bend (R)	1622	1520	1519	1555	
20	CH bend (R)	1634	1526	1524	1562	
21	C-H stretch (R) sym	3300	3062	3073	3074	
22	C-H stretch (R) asym	3461	3129	3162	3139	
23	C-H stretch (R) asym	3489	3169	3199	3176	
24	H-5 str.	3492	3274	3332	3316	3339

Table 4.3: Calculated frequencies [cm^{-1}] of simplified ligand models using different basis sets (‘ip’ denotes an in-plane and ‘oop’ an out-of-plane bend, ‘wag’ an out-of-plane wagging).

When comparing the basis sets it is to note that the results using the LanL2DZ basis set lie in good agreement with those of the largest basis (6-311G*), whereas the poorer basis sets (STO-3G and 3-21G) differ somewhat more. The core potential basis set LanL2DZ has been proved to be superior to 3-21G or 3-21G** by comparative calculations especially in systems containing transition metals [LEH99]. Therefore, this basis set has been employed exclusively for the systems containing transition metals. The calculated normal modes of htz are plotted in the appendix (figure A.2).

In table 4.4 the results of propyl-tetrazole (ptz) are summarised and compared with experimental data (Raman spectra of ptz at 30 K from 20 - 1300 cm^{-1} [HOE95] and of the iron complex from 1300 - 3500 cm^{-1} as well as IR spectra of ptz from 100 - 3500 cm^{-1} [this work]):

	Mode	STO-3G	6-311G(d)	exp.(IR)	exp.(Raman)
1	CH ₂ (R) Rot (1)	21	35		52/57
2	Alk.-Ring bend	82	92		63/75
3	4-R oop (2)	124	142		94/108/117
4	CH ₃ (R) rot	215	237		136/149/157
5	4-R ip (3)	272	290	285	259
6	4-R ip (3)	338	370	343/362	315/357
7	Alk. Ring bend	450	456	396/462	395
8	4-3/5 oop (4)	588	645	646	
9	2/1 oop (6)	640	692	664/675	673
10	2-1/3 oop	661	708	721/742	724/743
11	5-H oop (7)	827	824	804	764
12	C-C (R) w ag	856	856		
13	1-2 str (8)	907	868	868	
14	C-C str. (R)	920	875	878	
15	C-C (R) w ag	965	910	901	905
16	1-2/3-4 sym	986	969	966	975
17	1-2/3-4 asym	1066	1051	1021	1033/1044
18	CH (R) bend/5-H ip	1110	1060	1089	1090/1096
19	CH (R) bend/5-H ip (11)	1130	1107	1111	1120/1125
20	2-3 str/ 5-H ip (12)	1157	1140		
21	C-H (R) w ag (13)	1194	1163	1170	1172
22	H-5 ip (14)	1219	1199		1204
23	C-H (R) w ag / ring breath (15)	1276	1228	1249	1252
24	C-H (R) w ag / ring breath	1348	1305	1280/1305	1308
25	C-H (R) w ag / ring breath	1391	1338	1350	1345
26	5-4/5-1 sym str. + C-H (R) ip (16)	1453	1390	1371/1388	1390
27	C-H bend (R)	1470	1417	1426	
28	C-H bend (R)	1502	1433	1444	1442
29	5-4/5-1 asym str. + C-H (R) ip (17)	1513	1460	1462	
30	CH ₃ (R) umbrella	1579	1464	1468	
31	C-H bend (R)	1610	1525	1487	
32	C-H bend (R)	1654	1533		1513
33	C-H bend (R)	1680	1542		
34	C-H bend (R)	1688	1545		
35	C-H stretch (R)	3319	3011	2876	2890
36	C-H stretch (R)	3338	3024	2940	
37	C-H stretch (R)	3342	3043	2970	2952
38	C-H stretch (R)	3445	3060		2983
39	C-H stretch (R)	3455	3092		3015
40	C-H stretch (R)	3486	3102		
41	C-H stretch (R)	3488	3117		
42	H-5 str (24)	3492	3304	3130	3148

Table 4.4: Calculated and observed vibrational frequencies [cm^{-1}] of propyl-tetrazole. (Numbers in brackets denote the number of the analogous mode in table 4.3 on mtz/htz.)

There is a good agreement between the measured and the DFT frequencies.

Based on the above calculations, the intra-ligand mode, which appears at 374 cm^{-1} in the HS state of $[\text{Fe}(\text{ptz})_6](\text{BF}_4)_2$, and is thought to couple with the iron-nitrogen stretch in the LS state to $359/413 \text{ cm}^{-1}$, is assigned to the in-plane bend of the alkyl rest of the ligand. But to proof this coupling, further calculations on models of a complex molecule containing tetrazole ligands have to be employed. These are presented in the following sections.

4.6.4 $[M(N_3)_4(htz)_2]^{2-}$

In order to include properties of the propyltetrazole ligand, an octahedral complex with six tetrazoles (htz), thus only ignoring the alkyl substituent of the real system, has been calculated. Merely the zinc system could be optimised to a saddle point (one imaginary frequency of 363 cm^{-1}). These calculations turned out to be too complex for the available computer resources. Therefore, the model had to be further simplified. A system with two tetrazole ligands in trans position was chosen. Because of the problems with rotations in the NH_3 ligand calculations before, azide (N_3^-) ligands were selected for saturating the equatorial plane of the complex.

The LS system could be fully optimised in C_1 symmetry. The transformation of the force field to internal coordinates yields metal-ligand force constants of **1.609 mdyn/Å** (htz) and 1.009 mdyn/Å (azide), respectively. The corresponding off-diagonal elements are smaller than 20 % of the diagonal elements. The obtained potential energy distribution (PED) shows modes with remarkable Fe-N participation at 145, 201, 207, 343 and 393 cm^{-1} for the bond to the tetrazole ligand.

From these the vibrations at 201 cm^{-1} and $343/393\text{ cm}^{-1}$ are attributed to the symmetric and the antisymmetric Fe-N stretch of the trans tetrazole unit, respectively. The splitting of the antisymmetric stretch stems from a coupling with an in-plane tetrazole rotation.

Nevertheless, the results have to be taken with care, because the analogous $[Zn(N_3)_4(htz)_2]^{2-}$ splits off both tetrazoles during geometry optimisation.

4.6.5 $[M(diimine)_2(htz)_2]^{2+}$

Because of the failure of the zinc system of the previous model, another molecule was employed in the calculations, i.e. $[M(diimine)_2(htz)_2]^{2+}$ with the two-dentate diimine = $HN=CH-CH=NH$ in order to avoid complications with ligand rotations as in the hexammine complex. The geometry optimisations led to local minima for the LS and the zinc case and to a saddle point with one imaginary frequency of 53 cm^{-1} in the HS state. The results of these calculations together with the ratios of the LS to HS and LS to Zn values of the force constants are summarised in table 4.5. The off-diagonal elements of the force field in the used internal coordinates do not exceed 20 % (HS, Zn) or 10 % (LS) of the given diagonal elements (cf. also the force constants transferred to the simplified NCA model in the following section).

	<i>Zn</i>	<i>LS</i>	<i>HS</i> [1x -53cm ⁻¹]	LS/HS	LS/Zn
r [M-N(Htz)]	2.282 Å	2.010 Å	2.28 Å		
r [M-N(diimine)]	2.199 Å	1.982 Å	2.16 Å		
f [M-N(Htz)]	0.607 mdyn/Å	1.448 mdyn/Å	0.696/0.678	2.08/2.14	2.39
f [M-N(diimine)]	0.928 mdyn/Å	1.397 mdyn/Å	0.97/1.02/1.05	1.44-1.33	1.51
ν_s (Htz)	115 cm ⁻¹	185 cm ⁻¹	120 cm ⁻¹	(1.54) ² = 2.38	(1.6) ² = 2.56
ν_s (diimine)	207 cm ⁻¹ / (212 cm ⁻¹)	281 cm ⁻¹ / (353 cm ⁻¹)	213 cm ⁻¹ / (262 cm ⁻¹)	(1.31) ² = 1.74	(1.36) ² = 1.84
ν_{as} (Htz)	169 cm ⁻¹	263/428 cm ⁻¹	188 cm ⁻¹		
ν_{as} (diimine)	282/287 cm ⁻¹	449/456 cm ⁻¹	322 / 330 cm ⁻¹	1.9	2.5
					D_{HL}
E (B+HF-LYP) [H/particle]	-957.71	-1015.57	-1015.56		21.36 kJ/mol
Zero-point-vib. Energy [kJ/mol]	602.93	615.62	605.15		-10.47 kJ/mol
S _{elec.} [cal/mol/K]	0	0	3.198		13.39 J/mol/K
S _{vib.} [cal/mol/K]	38.15	26.13	31.28		21.56 J/mol/K

Table 4.5: Results of DFT calculations on [M(diimine)₂(htz)₂]²⁺ (thermoanalysis at 130K.)

Again, the metal-nitrogen distance is a bit larger than the values of X-ray structural investigations (HS: 2.176 Å [WIE93], LS: 1.988 Å [KUS99]), and the shortening of the bond during the spin transition is overestimated, too (for the tetrazole ligand).

The calculated energies sum up to a difference in zero-point energies of $\Delta E_{HL} = 10.89$ kJ/mol (i.e. 910 cm⁻¹). This, as well as the entropy changes [at 298 K: ΔS_{HL} (vib.) = 30.47 J/mol/K] fit very nicely to the known thermodynamic values of spin crossover compounds [HAU91, ROM93, GÜT96].

The extracted force fields yield a **factor of 2.1** in the metal-ligand bonding force constant to the tetrazole ligand. The very large splitting of the antisymmetric stretching mode (much larger than the experimentally observed one of 359/413 cm⁻¹) in this model is caused by interactions with the bending modes of the octahedron, which here are strongly influenced by the diimine bridges. In order to exclude this influence the gained force field has been used for classical NCA calculations of a further simplified model without the two-dentate bridges. These are presented in the next chapter.

One further vibration (which is slightly split into two modes, i.e. the symmetric and the antisymmetric combination) in the higher frequency range is to mention here, as well. It is an intra-ligand mode of the tetrazole ring with an in-plane motion of the coordinating nitrogen thus leading to a remarkable metal-nitrogen involvement:

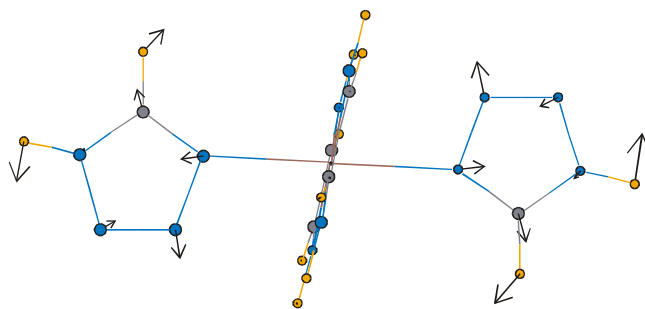


Figure 4.15: Intra-ligand mode with M-N contribution.

Because of the M-N contribution this mode feels the strengthening of the coordination bond when going from HS to LS. The DFT calculations yield energies of 1012/1030 cm^{-1} (Zn), 1012/1032 cm^{-1} (HS) and 1017/1041 cm^{-1} (LS) for this vibration. Therefore, this mode might be assigned to the observed shift of 1002/1023 cm^{-1} (HS) to 1006/1017/1029 cm^{-1} (LS) in $[\text{Fe}(\text{ptz})_6](\text{BF}_4)_2$. This is a further example of an intra-ligand mode sensitive to the spin transition in a similar way as the well-known shift of the C-N stretch in NCS containing spin cross-over compounds (cf. chapters 6 to 8).

The tetrazole coordinating system described in chapter 5, $\{\text{Fe}[(\text{entz}_3\text{N})]_2\}(\text{BF}_4)_2$, shows a shift in this energy regime [i.e. 1016 cm^{-1} (LS) and 1031 cm^{-1} (HS)], which is used there for monitoring the spin state in the Raman spectra. This shift is the opposite direction to the calculated one in this model, but in a comparable order of magnitude. Maybe the two-dimensional structure of this compound leads to the change of the Raman intensities of the different combinations of this vibration. From these calculations no definite explanation is available for this behaviour.

Selected eigenvectors obtained by the above calculations are plotted in the appendix.

4.7 Normal coordinate calculations

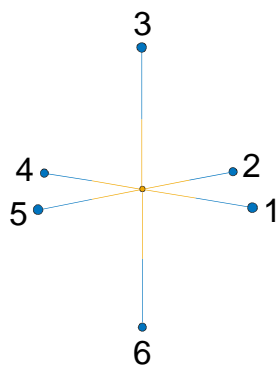
The results of the DFT calculations on the complex molecule with two tetrazole ligands in trans position in chapter 4.6.5 have been used to perform normal coordinate calculations on simplified models. This has been done in order to gain results for the simple case of an octahedron, which is usually discussed when talking about vibrational properties of spin-crossover molecules (chapter 4.7.1), and to eliminate the influence of the two-dentate diimine ligands on the more complex model with tetrazole ligands (chapter 4.7.2).

For this reason, the force field, which was obtained by the DFT calculations in cartesian coordinates, was transformed into a force field in (redundant) internal coordinates, which have to be chosen in an appropriate way, as described in chapter 2. This has been done with the program REDONG [ALL93].

The obtained force field was adapted to the symmetry of the molecule by taking the average of the affected force constants, which are not absolutely identical after the DFT calculations in C_1 symmetry, but should be identical in the symmetry of the molecule. For simplification, all values below 0.01 (i.e. $\sim 0.16\%$ of the largest force constant) are neglected and set to zero. With reduction of the model size parts of the force constant matrix are cut (i.e. the remaining internal coordinates are preserved as chosen for the transformation from cartesian coordinates). The reduction of the model size leads to higher symmetry of the model. This was taken into account by averaging out the corresponding force constants. The Fe-N force constant to the tetrazole ligand was used for all six Fe-N bonds (not the force constant to the diimine-ligand), i.e. the Fe-N force constants to the diimine ligands, which served as auxiliary ligands for the DFT calculations, are replaced by the Fe-N(tetrazole) force constant.

4.7.1 *FeN₆ core*

First of all, a normal coordinate analysis of the pure FeN₆ core was done with the force constants from DFT calculations as described above. This yields a good approach to the vibrational properties of the simplified complex. Of course the influences of the intra-ligand modes are excluded by these calculations, thus revealing the mere octahedral changes during the spin transition.

Figure 4.16: Numbering scheme of the FeN_6 core.

	r_1	r_2	r_3	r_4	r_5	r_6	α_{12}	α_{24}	α_{45}	α_{51}	α_{13}	α_{34}	α_{46}	α_{61}	α_{23}	α_{35}	α_{56}	α_{62}	
r_1	R																		
r_2	r	R																	
r_3	r	r	R																
r_4	0	r	r	R															
r_5	r	0	r	r	R														
r_6	r	r	0	r	r	R													
α_{12}	i	i	0	0	0	0	A												
α_{24}	0	i	0	i	0	0	a	A											
α_{45}	0	0	0	i	i	0	0	a	A										
α_{51}	i	0	0	0	i	0	a	0	a	A									
α_{13}	i	0	i	0	0	0	a	0	0	a	A								
α_{34}	0	0	i	i	0	0	0	a	a	0	a	A							
α_{46}	0	0	0	i	0	i	0	a	a	0	0	a	A						
α_{61}	i	0	0	0	0	i	a	0	0	a	a	0	a	A					
α_{23}	0	i	i	0	0	0	a	a	0	0	a	a	0	0	A				
α_{35}	0	0	i	0	i	0	0	0	a	a	a	a	0	0	a	A			
α_{56}	0	0	0	0	i	i	0	0	a	a	0	0	a	a	0	a	A		
α_{62}	0	i	0	0	0	i	a	a	0	0	0	0	a	a	a	0	a	A	

Scheme 4.1: Symbolic \mathbf{f} matrix for FeN_6 in O_h symmetry.

In scheme 4.1 the \mathbf{f} matrix in internal coordinates is presented with r_i being the variation of the bond distance from Fe to atom i , and α_{ij} that of the angle $i\text{-Fe-}j$. The internal force constants f are abbreviated as follows: $f_r = R$, $f_{r/r} = r$, $f_\alpha = A$, $f_{\alpha/\alpha} = a$, $f_{r/\alpha} = i$.

$S_1^{A_{1g}} = \frac{1}{\sqrt{6}}(r_1 + r_2 + r_3 + r_4 + r_5 + r_6)$ $S_2^{A_{1g}} = \frac{1}{\sqrt{12}}(a_{12} + a_{24} + a_{45} + a_{51} + a_{13} + a_{34} + a_{46} + a_{61} + a_{23} + a_{35} + a_{56} + a_{62})$
$S_1^{E_g} = \frac{1}{\sqrt{12}}(r_1 + r_2 - 2r_3 + r_4 + r_5 - 2r_6)$ $S_2^{E_g} = \frac{1}{2\sqrt{6}}(2a_{12} + 2a_{24} + 2a_{45} + 2a_{51} - a_{13} - a_{34} - a_{46} - a_{61} - a_{23} - a_{35} - a_{56} - a_{62})$ $S_3^{E_g} = \frac{1}{2}(r_2 - r_1 - r_4 + r_5)$ $S_4^{E_g} = \frac{1}{\sqrt{8}}(a_{23} + a_{35} + a_{56} + a_{62} - a_{12} - a_{24} - a_{45} - a_{51})$
$S_1^{T_{2g}} = \frac{1}{2}(a_{23} - a_{35} + a_{56} - a_{62})$ $S_2^{T_{2g}} = \frac{1}{2}(a_{13} - a_{34} + a_{46} - a_{61})$ $S_3^{T_{2g}} = \frac{1}{2}(a_{12} - a_{24} + a_{45} - a_{51})$
$S_1^{T_{1u}} = \frac{1}{\sqrt{2}}(r_1 - r_4)$ $S_2^{T_{1u}} = \frac{1}{\sqrt{8}}(a_{12} - a_{24} - a_{45} + a_{51} + a_{13} - a_{34} - a_{46} + a_{61})$ $S_3^{T_{1u}} = \frac{1}{\sqrt{2}}(r_2 - r_5)$ $S_4^{T_{1u}} = \frac{1}{\sqrt{8}}(a_{12} + a_{24} - a_{45} - a_{51} + a_{23} - a_{35} - a_{56} + a_{62})$ $S_5^{T_{1u}} = \frac{1}{\sqrt{2}}(r_3 - r_6)$ $S_6^{T_{1u}} = \frac{1}{\sqrt{8}}(a_{13} + a_{34} - a_{46} - a_{61} + a_{23} + a_{35} - a_{56} - a_{62})$
$S_1^{T_{2u}} = \frac{1}{\sqrt{8}}(a_{12} - a_{24} - a_{45} + a_{51} - a_{13} + a_{34} + a_{46} - a_{61})$ $S_2^{T_{2u}} = \frac{1}{\sqrt{8}}(a_{23} - a_{35} - a_{56} + a_{62} - a_{12} - a_{24} + a_{45} + a_{51})$ $S_3^{T_{2u}} = \frac{1}{\sqrt{8}}(a_{13} + a_{34} - a_{46} - a_{61} - a_{23} - a_{35} + a_{56} + a_{62})$

Table 4.6: Symmetry coordinates of FeN₆ in O_h symmetry in terms of internal coordinates.

The transformation to symmetry coordinates in O_h symmetry with the redundant coordinates $S_2^{A_{1g}}$, $S_2^{E_g}$, $S_4^{E_g}$ yields the **F** matrix (scheme 4.2) with its elements expressed in terms of the internal force constants f_{ij} as defined in scheme 4.1.

$$S_1^{A_{1g}} \ S_2^{A_{1g}} \ S_1^{E_g} \ S_2^{E_g} \ S_3^{E_g} \ S_4^{E_g} \ S_1^{T_{2g}} \ S_2^{T_{2g}} \ S_3^{T_{2g}} \ S_1^{T_{1u}} \ S_1^{T_{1u}} \ S_3^{T_{1u}} \ S_4^{T_{1u}} \ S_5^{T_{1u}} \ S_6^{T_{1u}} \ S_1^{T_{2u}} \ S_2^{T_{2u}} \ S_3^{T_{2u}}$$

R+4r																
$\sqrt{8}i \ A+6a$																
0	0	R-2r														
0	0	$\sqrt{2}i$	A													
0	0	0	0	R-2r												
0	0	0	0	$\sqrt{2}i$	A											
0	0	0	0	0	0	A-2a										
0	0	0	0	0	0	0	0	A-2a								
0	0	0	0	0	0	0	0	0	0	A-2a						
0	0	0	0	0	0	0	0	0	0	0	R					
0	0	0	0	0	0	0	0	0	0	0	2i	A+2a				
0	0	0	0	0	0	0	0	0	0	0	0	R				
0	0	0	0	0	0	0	0	0	0	0	0	2i	A+2a			
0	0	0	0	0	0	0	0	0	0	0	0	0	0	R		
0	0	0	0	0	0	0	0	0	0	0	0	0	0	2i	A+2a	
0	0	0	0	0	0	0	0	0	0	0	0	0	0	0	A-2a	
0	0	0	0	0	0	0	0	0	0	0	0	0	0	0	0	A-2a
0	0	0	0	0	0	0	0	0	0	0	0	0	0	0	0	A-2a

Scheme 4.2: Symbolic \mathbf{F} matrix expressed in terms of elements of \mathbf{f} .

With a metal nitrogen distance of 2.0 Å (LS) and 2.2 Å (HS), respectively, the processing of the NCA using the force constants stated in table 4.7 leads to the vibrational energies, presented in table 4.8 with the complete ligand mass of 112u (ptz) and 84u (mtz) at the single point of the coordinating atom.

\mathbf{f}	\mathbf{R}	\mathbf{A}	\mathbf{r}	\mathbf{a}	\mathbf{i}
HS	0.7	0.3	0.04	0.04	0.06
LS	1.5	0.6	0.1	0.04	0.06

Table 4.7: Internal force constants of HS and LS FeN_6 core NCA [units are $\text{mdyn}/\text{Å}$ for stretches, $\text{mdyn} \cdot \text{Å}$ for bends and mdyn for stretch-bend interactions].

	HS (ptz)	HS (mtz)	$\text{Dn}^{\text{HS}}(54-56)$	LS (ptz)	LS (mtz)	$\text{Dn}^{\text{LS}}(54-56)$
ν (M-N) T_{1u}	236	241	4	366	374	6
ν (M-N) A_{1g}	114	132	0	170	196	0
ν (M-N) E_g	97	112	0	140	162	0
δ (M-N) T_{1u}	75	85	0.1	106	121	0.1
δ (M-N) T_{2g}	52	61	0	89	103	0
δ (M-N) T_{2u}	37	43	0	63	72	0

Table 4.8: Calculated vibrational energies and isotope shifts (^{54}Fe - ^{56}Fe) in $[\text{cm}^{-1}]$.

The corresponding eigenvectors have already been plotted in chapter 2 (figure 2.1). The obtained vibrational energies as well as the calculated isotope shifts for labelling with ^{54}Fe fit

very well to the experimentally observed and assigned values of the T_{1u} stretch in the propyl-tetrazole complex system. Also the shift due to the lighter ligand mtz of 5 cm^{-1} (HS) and 8 cm^{-1} (LS), respectively, match the measured ones.

These comparisons suggest that the other calculated vibrations which have not been assigned unequivocally in the measured infrared or Raman spectra should fit to the observable modes of the real system, too.

The explanation for the splitting of the T_{1u} stretch in the LS state, however, requires a more complex system including tetrazole ligands. The results of these calculations are presented in the next section.

4.7.2 $Fe(Rtz)_2N_{(eq)4}$

For taking into account some contributions of the ligand modes to the low frequency vibrations of the complex molecule (in addition to the pure octahedral modes derived in the previous section) and to eliminate the influence of the diimine bridges included in the performed DFT calculations, a model system with two trans tetrazole rings containing an alkyl chain simplified by a single atom substituent R, and four equatorial atoms N carrying the complete ligand mass, is considered in the following calculations.

The chosen internal coordinates are presented in table 4.9 [for atom numbering scheme see figure A.1 (appendix); here e.g. '1-2' means the stretching of the 1-2 bond, 'wag 1' the out-of-plane bend of atom 1 and 'ip 1' the in-plane bend of the angle at atom 1]. The \mathbf{f} matrix is shown in scheme 4.3. Here, the internal coordinates as well as the force constants are not denominated by letters but by numbers. The values of the force constants in comparison with those of the DFT calculations on the pure ligand and the $[M(NH_3)_6]^{2+}$ system are listed in table 4.10. The values of the force constants of the N-R stretch (#6) and of the R-wagging (#13) differ a lot between the complex molecule (R=H) and the pure ligand (R=propyl). In order to get closer to the real system the values of the pure ligand calculation have been used in the NCA calculations.

#	Internal coordinate	#	Internal coordinate	#	Internal coordinate
1	Fe-N(Tz) A (r_1)	26	wag 3 A	51	ip H B2
2	Fe-N(Tz) B (r_4)	27	wag 4 A	52	ip Fe-3 A
3	1-2 A	28	wag 5 A	53	ip Fe-5 A
4	1-2 B	29	wag 1 B	54	ip Fe-3 B
5	2-3 A	30	wag 2 B	55	ip Fe-5 B
6	2-3 B	31	wag 3 B	56	Fe-N(eq)3 (r_3)
7	3-4 A	32	wag 4 B	57	Fe-N(eq)4 (r_6)
8	3-4 B	33	wag 5 B	58	oct-angle 1 (α_{12})
9	4-R A	34	ip R A1	59	oct-angle 2 (α_{24})
10	4-R B	35	ip H A1	60	oct-angle 3 (α_{45})
11	4-5 A	36	ip R B1	61	oct-angle 4 (α_{51})
12	4-5 B	37	ip H B1	62	oct-angle 5 (α_{13})
13	5-H A	38	ip 1 A	63	oct-angle 6 (α_{34})
14	5-H B	39	ip 2 A	64	oct-angle 7 (α_{46})
15	5-1 A	40	ip 3 A	65	oct-angle 8 (α_{61})
16	5-1 B	41	ip 4 A	66	oct-angle 9 (α_{23})
17	Fe-N(eq)1 (r_2)	42	ip 5 A	67	oct-angle 10 (α_{35})
18	Fe-N(eq)2 (r_5)	43	ip 1 B	68	oct-angle 11 (α_{56})
19	torsion Tz-Fe-Tz	44	ip 2 B	69	oct-angle 12 (α_{62})
20	wag R A	45	ip 3 B	70	torsion A vs N_{eq4}
21	wag R B	46	ip 4 B	71	torsion A vs N_{eq4}
22	wag H A	47	ip 5 B	72	Tz A torsion 1
23	wag H B	48	ip R A2	73	Tz A torsion 2
24	wag 1 A	49	ip H A2	74	Tz B torsion 1
25	wag 2 A	50	ip R B2	75	Tz B torsion 2

Table 4.9: Numbering and definition of the internal coordinates of $Fe(Rtz)_2N_{eq4}$. (The names in brackets refer to the denomination in scheme 4.1 of the simpler model.)

	61	62	63	64	65	66	67	68	69	70	71	72	73	74	75
61	40														
62	43	40													
63	-43	44	40												
64	-43	44	44	40											
65	43	44	44	44	40										
66	-43	-43	-43	43	43	40									
67	-43	43	43	-43	-43	44	40								
68	43	43	43	-43	-43	44	44	40							
69	43	-43	-43	43	43	44	44	44	40						
70	0	0	0	0	0	0	0	0	0	0	47				
71	0	0	0	0	0	0	0	0	0	0	0	47			
72	0	0	0	0	0	0	0	0	0	0	0	0	48		
73	0	0	0	0	0	0	0	0	0	0	0	0	0	48	
74	0	0	0	0	0	0	0	0	0	0	0	0	0	0	48
75	0	0	0	0	0	0	0	0	0	0	0	0	0	0	48

Scheme 4.3: \mathbf{f} matrix in terms of the 75 internals defined in table 4.9 with its 48 different force constants for $Fe(Rtz)_2N_{eq4}$.

f #	description	Fe(Rtz) ₂ N _{eq4} (NCA)		[M(NH ₃) ₆] (DFT)		
		HS	LS	HS	LS	Zn
	r (M-N(Tz)) [Å]	2.2	2	2.3	2.11	2.29
1	Fe-N(Tz)	0.7	1.45	0.6	1.03	0.53
10	off diag.	0.04	0.1	0.09	0.06	0.1
2	Fe-N _{eq}	0.7	1.45	0.6	1.03	0.53
11 41	off diag. trans	0.04	0.1	0.09	0.06	0.1
42	off diag. (Tz)	0.04	0.1			
40	oct. Angle	0.3	0.6	0.29	0.58	0.29
44	off In plane	-0.1		- 0.1	- 0.2	-0.1
43	off ^	0.04		0.02	0.02	0.02
45	off oct/Fe-N	0.06		0.05	0.05	0.06
<i>Ligand Ptz (6-311G) :</i>						
3	1-2-str.	2.8			2.759	
4	2-3-str.	4.9			4.388	
30	inter (1-2)	0.25			0.3	
5	3-4-str.	3.4			3.35	
22	inter (1-2)	1.39			1.29	
31	inter (2-3)	0.25			0.4	
6	N-R-str.	4.77			4.887	
7	4-5-str.	4.95			4.69	
23	inter (1-2)	1.3			1.21	
24	inter (2-3)	1.95			1.86	
8	C-H-str.	6.1			5.375	
9	5-1-str.	5.3			5.228	
30	inter (1-2)	0.25			0.3	
25	inter (2-3)	1.9			1.75	
26	inter (3-4)	1.55			1.4	
29	inter (4-5)	0.25			0.2	
12	Torsion 2-3	0.03		0.003	0.05	0.009
13	wag R	0.4			0.4	
46	wag H	0.4				
14	wag 1,2,3,4,5	0.16			0.2	
27		0.1			0.1	
28		0.15			0.15	
15	ip R	0.5			0.55	
16	ip H	0.47			0.46	
17	ip 1	0.87			1.31	
18	ip 2	1.44			1.559	
19	ip 3	1.42			1.47	
20	ip 4	0.88			0.89	
21	ip 5	0.89			0.9	
38	ip Fe-3	0.45				
39	ip Fe-5	0.35				
47	Tors. 2 vs. N _{eq4}	0.07				
48	ptz-Tors. 2-5 5-9	0.3				
32		0.3				
33		0.55			0.64	
34		0.93			0.82	
35		0.72			1.01	
36		1.36			1.33	
37		1.5			1.53	

Table 4.10: Comparison of the force constants used for the NCA with those of the DFT calculations of the pure ligand and of [M(NH₃)₆]²⁺. (For clarity the LS NCA column only contains the values different from HS).

M (N_{eq}/R)	HS-ptz	HS-mtz	LS-ptz	LS-mtz	HS	Dn	LS	Dn	HS	LS	LS
f(Fe-N) [mdyn/Å]	112/43	84/15	112/43	84/15	112/12		112/12		112/12	112/12	112/12
assignment											
5-H	3354	3354	3354	3354	3354		3354		3354	3354	3354
4-R	1501	1511	1505	1514	1518		1520		1518	1521	1523
1-5	1395	1408	1401	1416	1414		1422		1415	1427	1431
2-3	1261	1263	1261	1264	1266		1267		1266	1268	1269
1-2/3-4	1214	1234	1218	1236	1241		1243		1242	1244	1245
wag H	1163	1163	1163	1164	1164		1164		1164	1164	1164
ip H	1148	1152	1150	1155	1154		1157		1154	1159	1161
ip 2	1071	1072	1080	1080	1072		1080		1073	1085	1090
3-4	973	975	974	976	975		976		975	977	977
1-2	916	923	930	938	926		941		928	949	956
wag 3	790	791	790	792	792		792		792	792	792
ip 4	472	650	484	653	697		699		697	700	701
wag 1	681	681	685	685	681		685		681	685	685
ip R _{as}	332	365			378				378		
ip R _s	322	360	325	362	374	0.3	376	0.0	374	376	377
Fe-(N _{eq}) _{as}	236	249	371	386	250	3.3	392	2.1	262	416	448
Fe-(N _{eq}) _s	219	225	346	353	223	3.4	348	4.8	238	394	434
Fe-N(tz) _{as}	213	218	321	340	219	3.4	341	4.0	235	379	408
Fe-N(tz) _s			300	324			326	4.5		356	365
wag R _{a/b}	276/271	295/292	279/273	298/293	303/300	0.3	305/298	0.6	303/300	305/303	305/304
Fe-N (tz) _s	95	112	178/126	196/155	124		175		131	201	215
Fe-(N _{eq}) _s	114	132	160	181	106		151		113	184	196
Fe-(N _{eq}) _s + ip R	100	115	143	160	100		143		107	173/167	187
	151/137	168/154	160	182	172/150	0.3	189/178		172/156	184	187/181
'T _{1u} ' bend	90	104	108	125	100		121		101	123	124
'T _{2g} ' bend	72/67/65	84/79/70	96/85/82	111/99/92	72/71/65		96/89/83		72/71/65	96/89/83	96/89/83
'T _{2u} ' bend	48/40/27	56/46/35	59/57/28	71/69/36	54/40/34		65/59/35		54/40/34	65/59/35	66/59/35
oop tz rot.	126/123/ 51/45/15	136/133/ 59/47/20	149/ 55/46/16	165/162/ 58/48/23	131/ 56/46/21		159/157/ 59/47/23		134/131/ 56/46/21	161/160/ 59/47/23	162/159/ 59/47/23
ip tz rot.	21	28	28	36	28		38		28	38	38

Table 4.11: NCA calculated vibrational energies [cm^{-1}] with varying masses of R and two different sets of metal-ligand force constants for HS and LS. Dn denotes the calculated frequency shift on isotope substitution: Fe⁵⁴-Fe⁵⁶.

Table 4.11 summarises the results of the NCA calculations with different masses of the equatorial nitrogens N_{eq} (112 for ptz and 84 for mtz) and of the alkyl rest R (43 for ptz, 15 for mtz and 12 for just the bonded carbon atom). In addition, the last five columns contain the results with slightly changed metal-ligand force constants (#1 and #2 in the calculations) of 0.8 mdyne/Å (HS) and 1.95 or 2.40 mdyne/Å (LS), which have been chosen to adjust the anti-symmetric Fe-N stretch to the experimental values of 234 cm^{-1} (HS) and 359/413 cm^{-1} (LS). This last value of 2.4 mdyne/Å should be a maximum to the possible values as stated in the very beginning of the introduction, because it corresponds to the value of the strong-field $[\text{Fe}(\text{CN})_6]^{4-}$ complex and to a factor of three between the force constants of the high-spin and low-spin Fe-N bond. It can be seen in the resulting vibrational energies, that the sole variation of the Fe-N force constant does not influence the Fe-N-vibrations that strongly. The ‘ T_{2g} ’ and ‘ T_{2u} ’ bends, which have been named from O_h symmetry, are split due to lower local symmetry. Figures 4.17 and 4.18 show the atom displacements of the most important modes in HS (0.8 mdyne/Å) and LS (1.95 mdyne/Å) state.

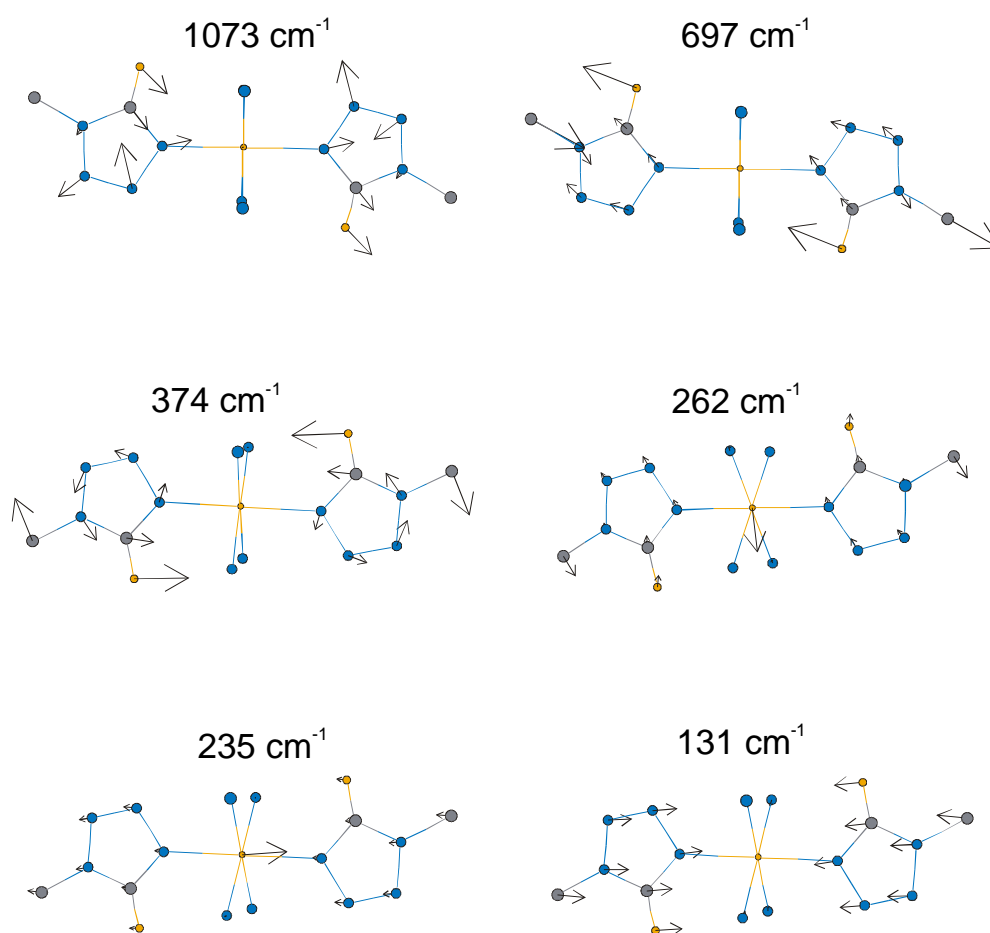


Figure 4.17: Selected eigenvectors of the HS model (0.8 mdyne/Å).

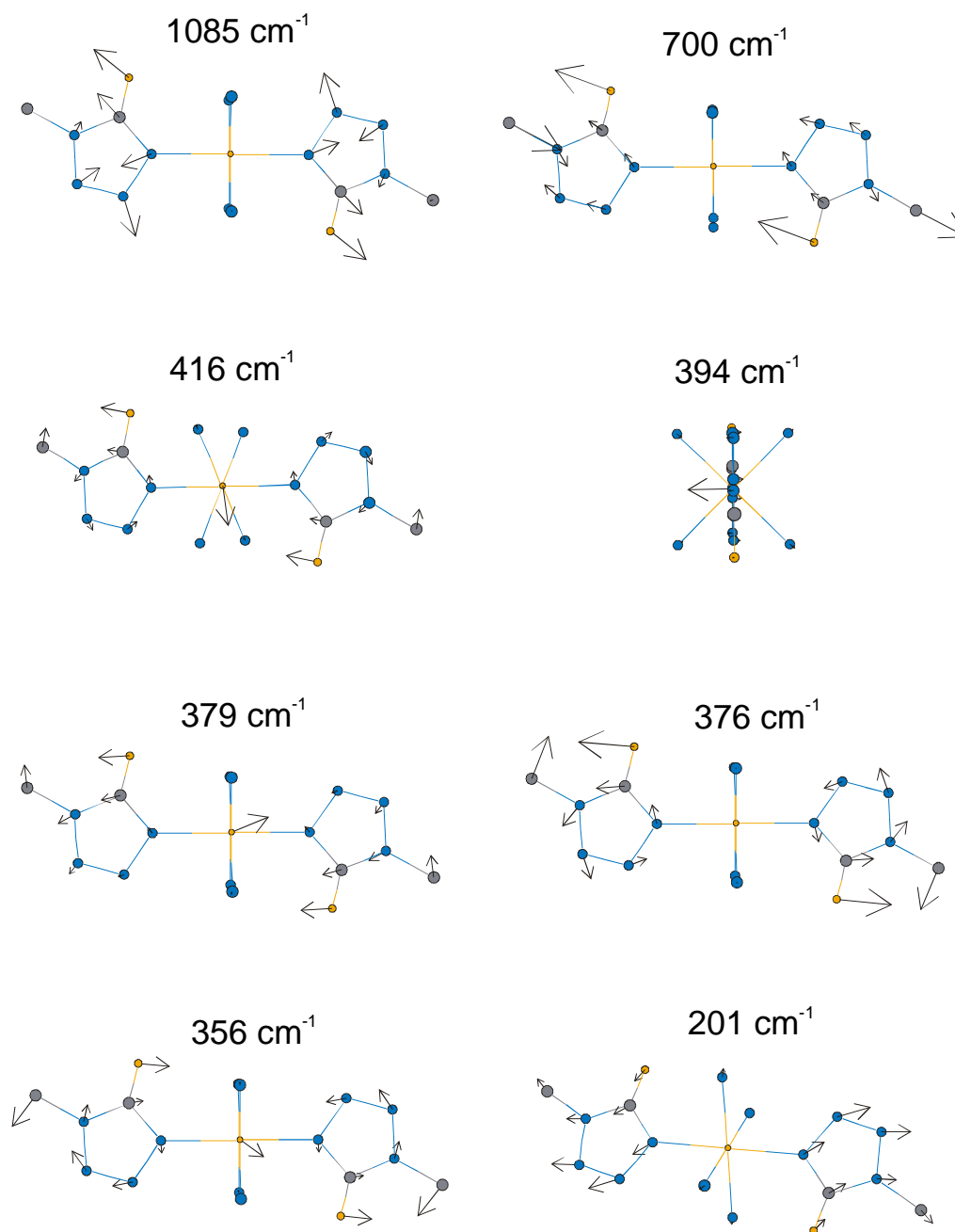


Figure 4.18: Selected eigenvectors of the LS model (1.95 mdyne/Å).

Like in the DFT calculations on the analogue system (with diimine bridges), a ring mode contains a rather large movement of the coordinating atom thus resulting in a shift from 1073 cm^{-1} (HS) to 1085 cm^{-1} (LS). Unfortunately, the MIR spectra of the complexes in this region are governed by the intense absorption of the BF_4^- anion, making a detailed comparison with the experimental values impossible. But the Raman spectra of $[\text{Fe}(\text{ptz})_6](\text{BF}_4)_2$ reveal a shift from 1088/1124 cm^{-1} (HS) to 1094/1118 cm^{-1} (LS) [HOE95] which fits perfectly to the calculated values. The modes at 700 or 697 cm^{-1} , respectively, which are denoted as ‘ip 4’, i.e. a bend of the angle at atom 4, also involve a large movement of the alkyl substituent R, so that the frequencies strongly depend on the used mass for this substituent. With the complete

propyl mass of 43u this vibration shows a shift from 472 cm^{-1} (HS) to 484 cm^{-1} (LS). Probably, this motion together with an alkyl-ring bend (as calculated for the pure ptz ligand) is responsible for the experimental shift of 474 cm^{-1} (HS) to 488 cm^{-1} (LS) in the single crystal FIR spectra. But the mass of 43u is too large for simulating the in-plane R movement. This can be understood in terms of an effective mass, which is dependent on the direction of the motion: the 'ip 4' bend is a motion parallel to the C-C bond of the alkyl chain, whereas the ip-R motion is more or less perpendicular to the C-C bond. These two motions are described by the two extrema of the mass of the substituent R, i.e. the complete ligand mass for the parallel motion with large force constants in the alkyl chain and only the mass of the bonded C atom for the motion perpendicular to the chain, which has weak restoring forces for the bend, respectively.

The mixing especially in the low-spin state of the anti-symmetric Fe-N stretch with the in-plane R movement located at around 375 cm^{-1} (HS) clearly explains the appearance of two modes sensitive to metal-isotope substitution. Due to symmetry, the 'gerade' combination of this mode (concerning the two different rings) remains at 376 cm^{-1} in this model of the LS state. The ip-R vibration contributes to the Fe-N_{eq} stretch within the tetrazole plane (416 cm^{-1}), as well.

Finally, the symmetric Fe-N(tz) stretch, which is the reaction coordinate of the spin transition, is calculated to be 131 cm^{-1} (HS) and 201 cm^{-1} (LS), respectively. Unfortunately, this result does not facilitate an unequivocal assignment of the 'A_{1g}' mode in the polarised Raman spectra [HOE95]. Possibly, the zz-polarised modes at **141 cm^{-1} (HS)** and **236 cm^{-1} (LS)** have to be attributed to the totally symmetric stretching mode.

The further 'octahedral' modes, i.e. the three different octahedral bends, can be clearly identified in the NCA calculations in contrast to the DFT calculations (cf. table 4.11 for the calculated values). In the DFT calculations interaction with the two-dentate diimine ligands leads to a strong mixing of modes.

5 The System $\{\text{Fe}[(\text{entz})_3\text{N}]_2\}(\text{BF}_4)$

5.1 Physical properties

Samples of $\alpha\text{-}\{\text{Fe}[(\text{entz})_3\text{N}]_2\}(\text{BF}_4)_2$ with $(\text{entz})_3\text{N}$ (**L3**) = tris(tetrazol-1-yl-ethane)amine show a complete, abrupt thermal spin transition at $T_{1/2}^{\downarrow} = 162.5 \text{ K}$ / $T_{1/2}^{\uparrow} = 170.2 \text{ K}$ [RUD95]. The three-dentate ligand binds on three different iron atoms thus forming a two-dimensional network (Fig. 5.1) [BRO96].

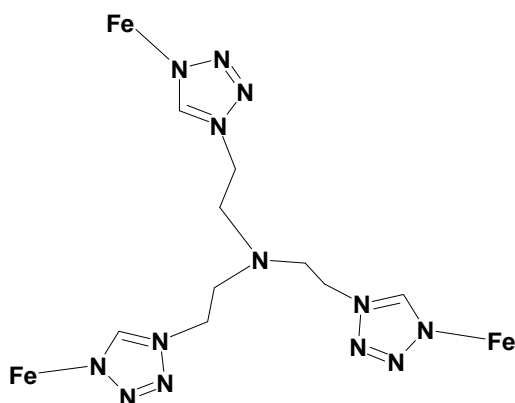


Figure 5.1: Connectivity of the L3 ligand.

Each iron atom is coordinated by six ligands in an octahedral manner. Therefore, the complex molecule is very closely related to the $[\text{Fe}(\text{ptz})_6](\text{BF}_4)_2$ system treated in chapter 4. The colours of the two compounds in the two spin states are very similar as well: the white powder of $[\text{Fe}(\text{L3})_2](\text{BF}_4)_2$ at room temperature becomes deep purple at temperatures below the spin transition at around 160 K.

X-ray structural measurements of the system in both spin states show that the spin change is connected to a structural change in the lattice, essentially a "switch" of one ethyl group per ligand of 90 degrees and one tetrazole ring of 45 degrees retaining the space group $P\bar{1}$ (fig. 5.2) [BRO96]. The metal-ligand bond length decreases from 2,18 Å to 1,99 Å when going from 293 K to 110 K.

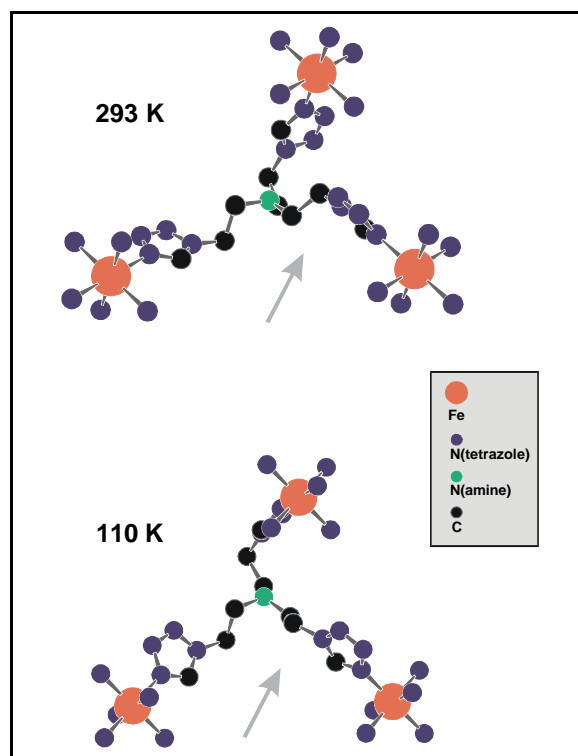


Figure 5.2: Structure of $[\text{Fe}(\mathbf{L3})_2](\text{BF}_4)_2$ at 293 and 110 K [BRO96]. The arrows indicate the structural changes mentioned in the text.

The analogous Zn system is isostructural with distances comparable to the HS structure.

5.2 Raman spectroscopy

5.2.1 Spectral features

The Raman spectra of $\alpha\text{-}\{\text{Fe}[(\text{entz})_3\text{N}]_2\}(\text{BF}_4)_2$ have been recorded at different temperatures using 514 or 752 nm excitation wavelengths. Also the corresponding Zn system as well as the pure ligand **L3** which has a tripod-like geometry have been investigated.

Besides quite a few changes in the low frequency region, some features in the 500-1200 cm^{-1} range clearly indicate the different spin states and the variation of the lattices: a mode at 1031 cm^{-1} (HS) and 1016 cm^{-1} (LS), which is assigned to an in-plane deformation of the tetrazole ring, and vibrations at 850 cm^{-1} (low spin lattice: LSL) and 822/864 cm^{-1} (high spin lattice: HSL) have been used to monitor the spin transition. These latter modes are believed to be connected to a CH_2 -rocking mode which shifts due to the "switch" of the ethyl group and the structural transition of the lattice, respectively.

5.2.2 Light induced structural phase transitions

Depending on various experimental parameters three different states have been achieved at low temperatures while irradiating with green light:

Keeping the excitation beam at 514 nm and constant power of 50 mW a series of spectra between 20 and 42,5 K has been measured. These spectra are depicted in figure 5.3.

At 20 K the resulting metastable LIESST state is immediately populated and has a lifetime of minutes as monitored by the recovering of the purple colour of the LS state by eyes.

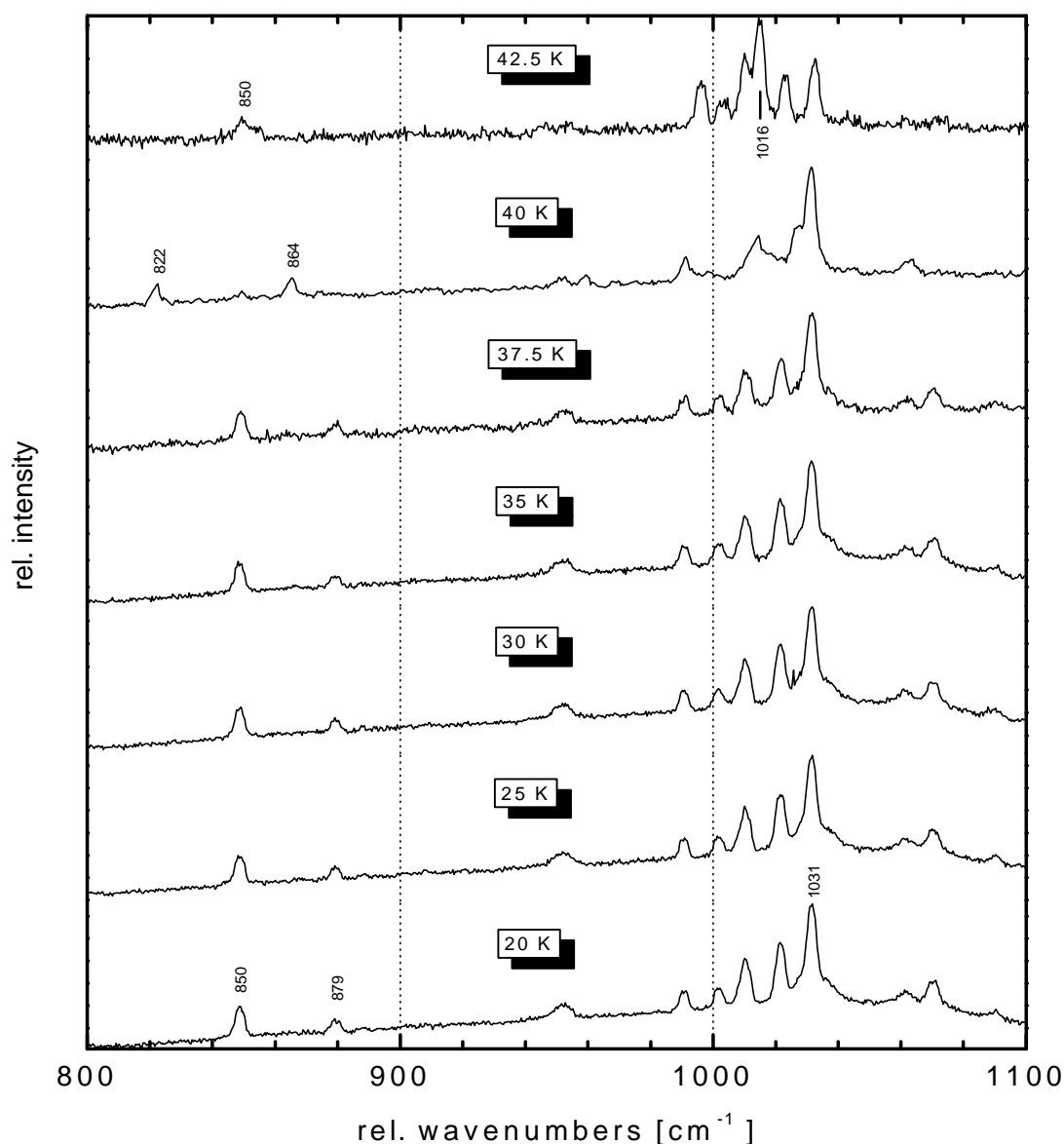


Figure 5.3: Raman spectra of $[\text{Fe}(\text{L3})_2](\text{BF}_4)_2$ at different temperatures and constant power of 50 mW at $\lambda = 514$ nm.

When increasing the temperature up to 37,5 K (always starting again from the LS state) the spectra still look the same as at 20 K. A decreasing decay time of the LIESST state with

increasing temperature is noticed by looking at the colour of the sample after stopping the irradiation. At 40 K the white colour of the powder still indicates the LIESST state of the complex molecule, but the spectrum differs in the 1000 - 1050 cm^{-1} region, lacks the modes at 850 and 879 cm^{-1} and shows two additional modes at 822 and 864 cm^{-1} as compared to the spectra at lower temperature. This LIESST state decays within days. Above 55 K this state decays on the minute time scale.

Irradiating at 42,5 K the compound remains in the LS state as indicated by the deep purple colour of the sample. The spectrum again shows the mode at 850 cm^{-1} (without the peaks at 822 and 864 cm^{-1}) but now exhibits a different peak pattern in the 980 - 1100 cm^{-1} region.

This means, that within a range of 5 K three different spectra have been obtained under the same irradiation conditions. So, four situations are differentiated: HS/LS molecules in the HS lattice (HSL) and HS/LS molecules in the LS lattice (LSL). Three of them are met.

Obviously, a specific peak pattern in the 980 - 1100 cm^{-1} region refers to the spin state of the molecule, which was identified by the colour of the sample. As a working hypothesis the vibrations between 820 and 870 cm^{-1} are taken to depend on the structural state of the lattice and not on the spin state of the molecule.

This working hypothesis is proven by the spectrum above the transition temperature with the structure of the lattice in the HSL at 200 K, and the spectrum of the pure LS state in the LSL as achieved by irradiation at $\lambda_{\text{exc.}} = 752 \text{ nm}$ at 10 K. A comparison with the three different spectra obtained at low temperatures at $\lambda_{\text{exc.}} = 514 \text{ nm}$ is presented in figure 5.4. It clearly shows, that the vibrations at 1016 cm^{-1} (LS) and 1031 cm^{-1} (HS) can be used to monitor the spin state of the molecule, whereas the modes at 850 cm^{-1} (LSL) and 822/864 cm^{-1} (HSL) reflect the structural state of the lattice. The low-spin lattice (LSL) with the molecule in the HS state is supposed to show an additional mode at 879 cm^{-1} .

In summary, three different states of the compound have been obtained at temperatures below 50 K by irradiation at 514 nm with constant power of 50 mW: at 20 K a metastable LIESST state in the LSL is populated with a lifetime in the range of minutes. At 40 K the lattice switches to its high-spin lattice state and a LIESST state in the HSL with a lifetime in the range of days is produced, which is stable up to a temperature of $\sim 55 \text{ K}$. At 42,5 K the LS state in the LSL is obtained. The fourth conceivable state, LS molecules in the HSL via reverse-LIESST with red light could not be achieved even at 10 K, because the lattice always switches back to the LSL form.

Regarding the LIESST state at 40 K with its long lifetime, it was not expected to find a pure LS state at 42,5 K. This leads to the presumption that the interplay between the lifetime of the populated LIESST state and the laser power plays an important role for the achieved state. In order to better understand this interplay a series of spectra at 40 K with varying laser powers has been measured. The spectra are displayed in figure 5.5.

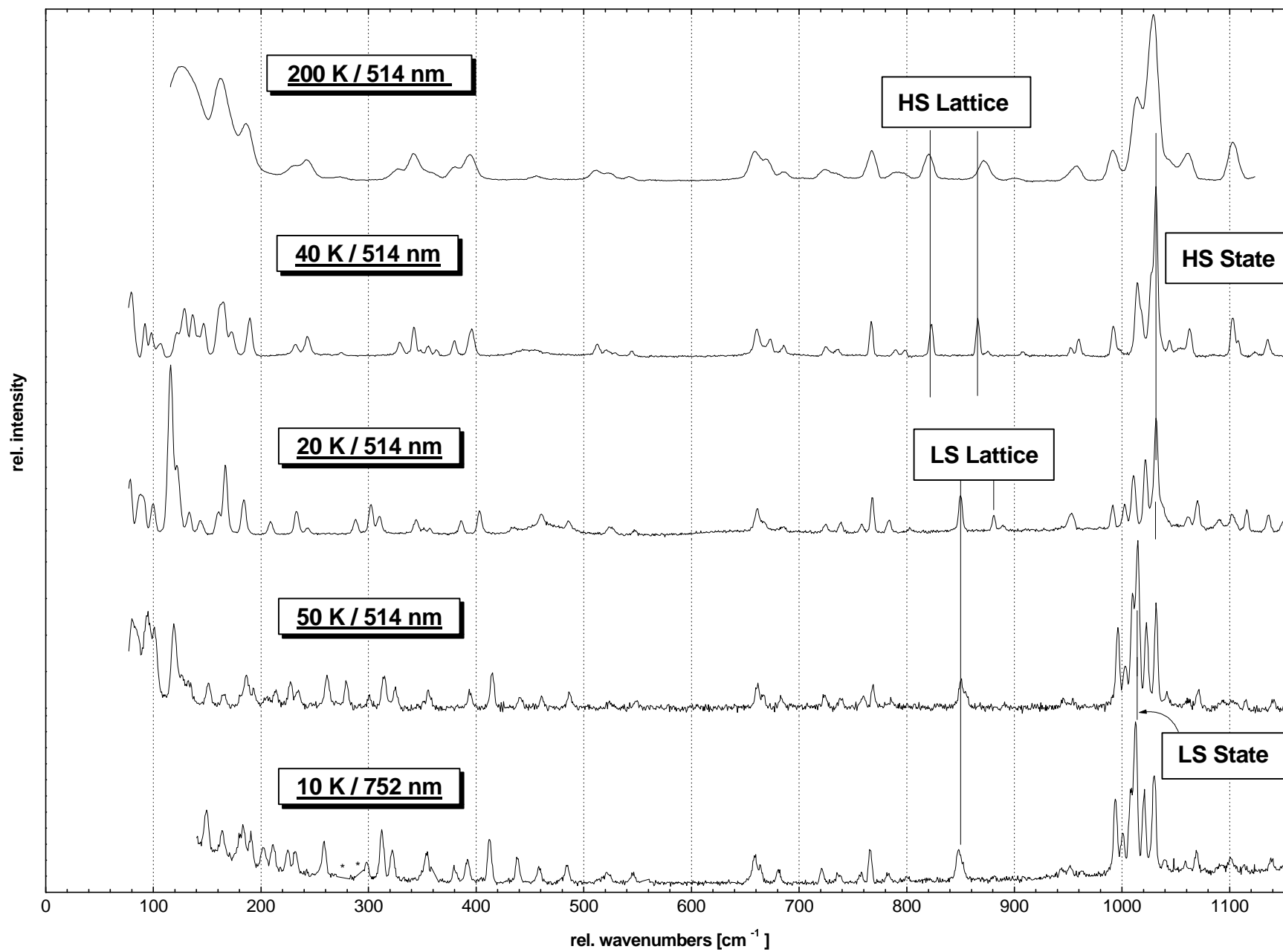


Figure 5.4: Raman spectra of the different accessible species of $[\text{Fe}(\text{L3})_2](\text{BF}_4)_2$ (* indicates removed Kr^+ laser plasma lines).

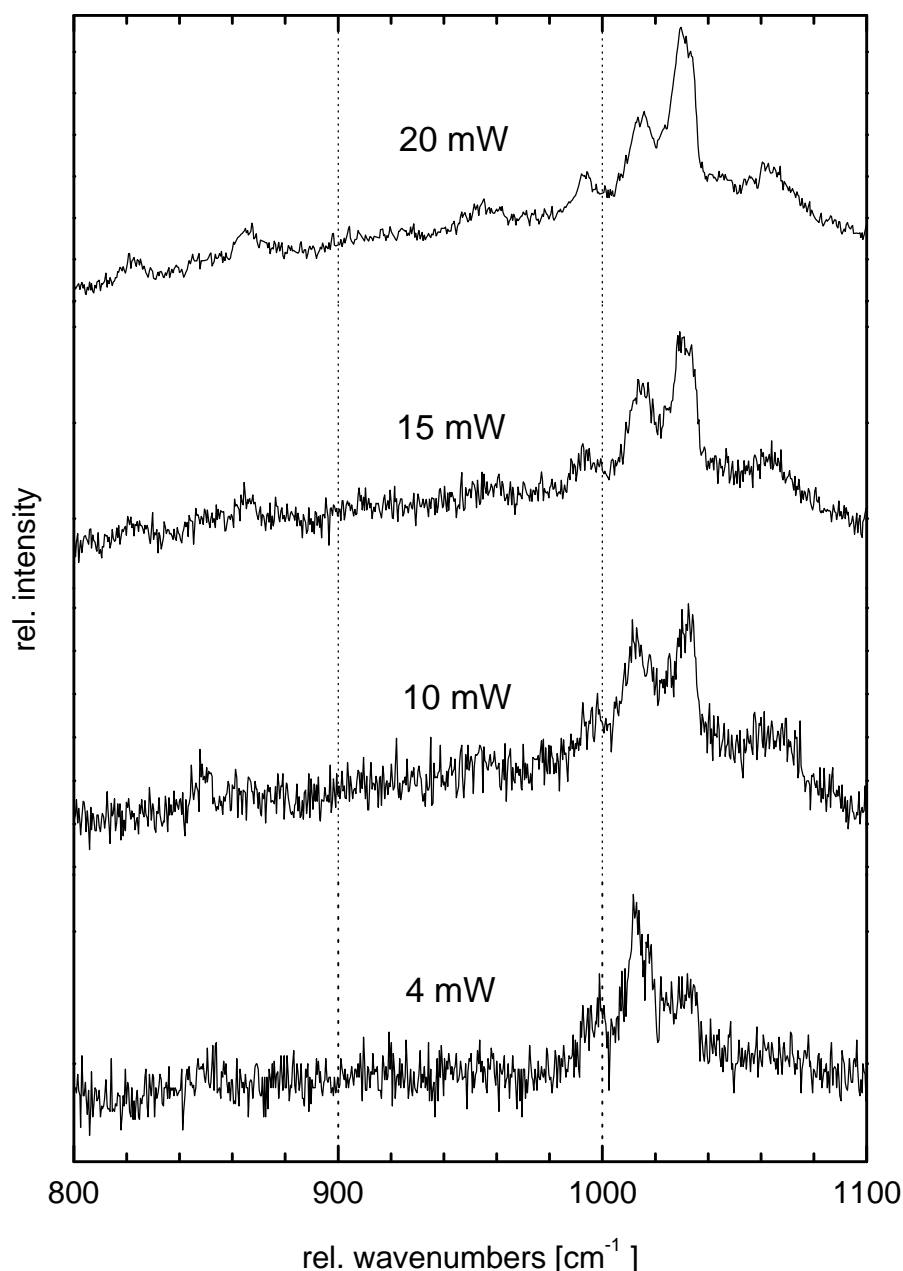


Figure 5.5: Dependence of the Raman spectra on the laser power at 40 K.

At very low laser powers (4mW) the LIESST state decays too fast such that it could be sufficiently populated to be observed in the Raman spectrum. Increasing light intensity (10 mW) leads to a remarkable HS fraction incorporated into the LS-lattice still decaying within minutes.

Only further gaining of a larger fraction of molecules in the HS state by higher excitation power enables the switching of the lattice to its HSL form (cf. spectrum at 20 mW). Now the LIESST state is stable for days up to approximately 55 K. This dependence on power shows, that a certain amount of molecules in the LIESST state is necessary to switch the lattice to its HSL form at a given temperature. This makes clear, why at 42,5 K only LS has been

observed: the number of excited molecules is too small to be observed in Raman spectroscopy, and especially too small to switch the lattice to the HSL form, in which the lifetime is much longer.

It is interesting to state that only one combination of experimental parameters (i.e. 50 mW, 514 nm at a temperature of 40 K) led to the observed light induced structural phase transition with a very long-lived LIESST state. With deviations from these parameters the state could not be reached: e.g. 4 mW excitation does not produce enough HS molecules to let the lattice „switch” at any temperature; 200 mW laser light locally overheats the sample, leading to already mostly LS state at a nominal temperature of 30 K. This clearly indicates that the activation barrier of this structural phase transition can only be overcome at moderately higher (homogeneous) temperatures (i.e. at 40 K and not at 20 K !).

This complex behaviour can be understood in terms of a complicated co-operation of temperature, laser power, light absorbance, cooling rate and lifetime of the metastable state. All these parameters also influence the penetration depth of the laser beam and therefore the amount of the surface that is taken into account during the measurement.

The scheme in figure 5.6 summarizes the experimentally accessible species.

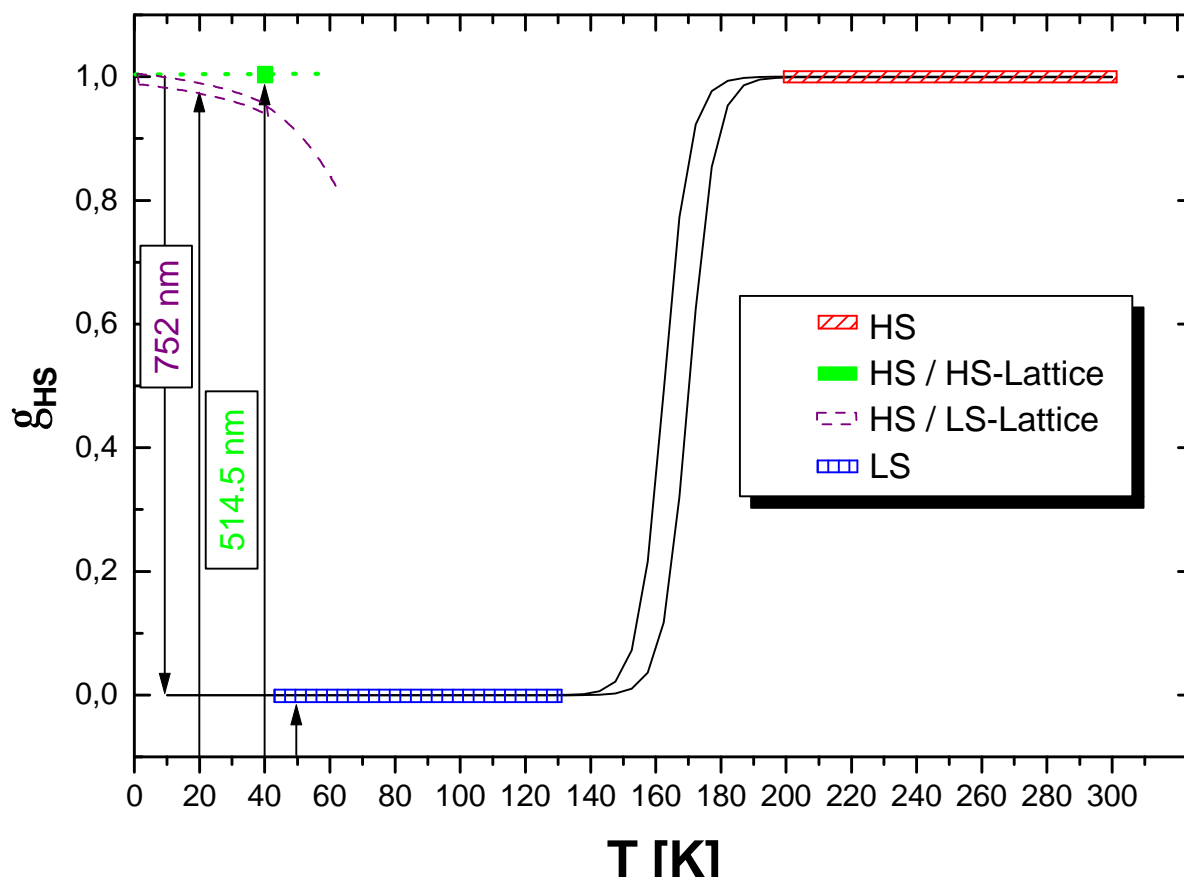


Figure 5.6: Scheme of the accessible species of $[\text{Fe}(\text{L}3)_2](\text{BF}_4)_2$ during Raman spectroscopic measurements.

5.2.3 *Low energy spectra of accessible species*

Figure 5.7 shows the Raman spectra of all accessible species of $\alpha\text{-}\{\text{Fe}[(\text{entz})_3\text{N}]_2\}(\text{BF}_4)_2$ in the range of $75 - 600 \text{ cm}^{-1}$ in comparison with the analogous zinc system and the pure ligand **L3**. The differences in the low frequency range should be analysed regarding the Fe-N stretching mode.

At first glance the spectra with different lattices show more variations than the spectra of different spin states in the same lattice. The main dissimilarities between the HS and the LS state in the LSL are bands at **167 cm^{-1}** (HS) and **$261/279 \text{ cm}^{-1}$** (LS) which should consequently be assigned to the Fe-N stretch. This corresponds to an average bond strengthening of the Fe-N bond by a factor of 2.6 (v^2).

All other modes more or less stay constant when going from HS to LS state. During this transition the complete peak pattern from $288 - 403 \text{ cm}^{-1}$ (HS) shifts about 10 cm^{-1} upwards, whereas the pattern between $230 - 250 \text{ cm}^{-1}$ shifts 10 cm^{-1} downwards. This can be understood in terms of a coupling with the Fe-N stretch which lies in between these two peak patterns in the LS state. Additionally, small shifts of vibrations below 160 cm^{-1} to slightly higher energy can be observed.

When changing the lattice while staying in the HS state the low frequency spectrum is modified quite strongly due to differences in the intra-ligand modes in the two geometric conformations and the low energetic lattice modes. This seems to have nearly no effect on the assigned Fe-N stretch at 167 cm^{-1} .

Comparing the HS and the Zn system in the corresponding lattices reveals very few changes. The Zn-N stretch that is expected slightly lower in energy than the $\text{Fe}^{\text{HS}}\text{-N}$ stretch should then consequently be assigned to the mode at **160 cm^{-1}** .

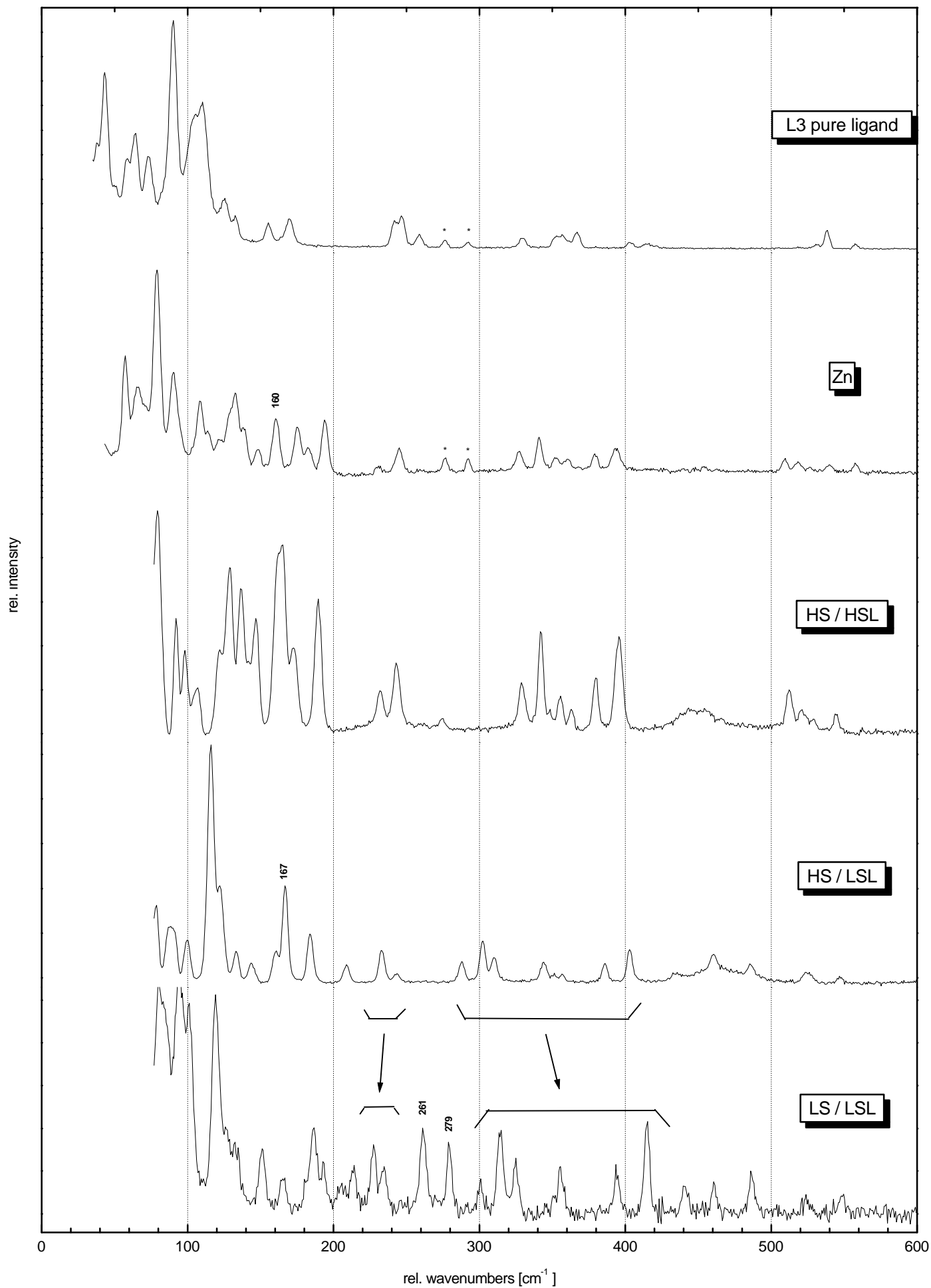


Figure 5.7: Low frequency range Raman spectra of $[\text{Fe}(\text{L3})_2](\text{BF}_4)_2$, its Zn analogue and the pure ligand **L3** (* indicates Kr^+ laser plasma lines).

5.3 Infrared spectra

Figures 5.8 and 5.9 show the middle and far infrared spectra of $[\text{Fe}(\mathbf{L3})_2](\text{BF}_4)_2$ in the HS and LS state and of the hydrochloride of the pure ligand measured as CsJ pellets.

The MIR spectra at 270 K (HS) and 40 K (LS) show practically no differences apart from smaller linewidths because of the decreasing temperature. Only the vibrations between 830 - 920 cm^{-1} show slight shifts / splittings again due to the CH_2 rocking modes of the ethyl bridge. The BF_4 mode at about 1070 cm^{-1} in the two spectra of the complexes is far too intense to be resolved here and hides the in-plane bend, which was used to monitor the spin transition in Raman spectroscopy.

Because of the lack of a clear spin state indicating probe in the MIR range it is not clear how large the amount of residual HS at 40 K is (see also chapters 6 and 8 for the influence of pressing pellets on the residual HS fraction at low temperatures).

In the FIR region (fig. 5.9) many more changes in the spectra can be noticed when cooling down from 270 to 40 K. Regarding the assignments in $[\text{Fe}(\text{ptz})_6](\text{BF}_4)_2$ the Fe-N stretch of the molecules in the HS state might be assigned to **236 cm^{-1}** (40 K) and **231 cm^{-1}** (270 K). This mode then clearly indicates a rather large amount of residual HS at 40 K.

When carefully comparing the spectra of the complex molecule at the two temperatures and the pure ligand, having in mind the $[\text{Fe}(\text{ptz})_6](\text{BF}_4)_2$ modes, besides an enhancement of some inner ligand bands at low temperatures, one can attribute the bands at **369, 386, 412 and 425 cm^{-1}** to Fe-N stretching modes of the molecules in the LS state. Again these modes are coupled with inner ligand vibrations, which are therefore shifted compared to the spectrum of the pure ligand and the complex molecule in the HS state.

In view of the conditions which have been found in the Raman experiments for reaching a long-lived LIESST state, it is not very astonishing that no LIESST effect could be observed during the IR measurements in a pellet even under constant laser irradiation during measurement. Therefore, only the spectra at different temperatures can be compared when looking at the two spin states.

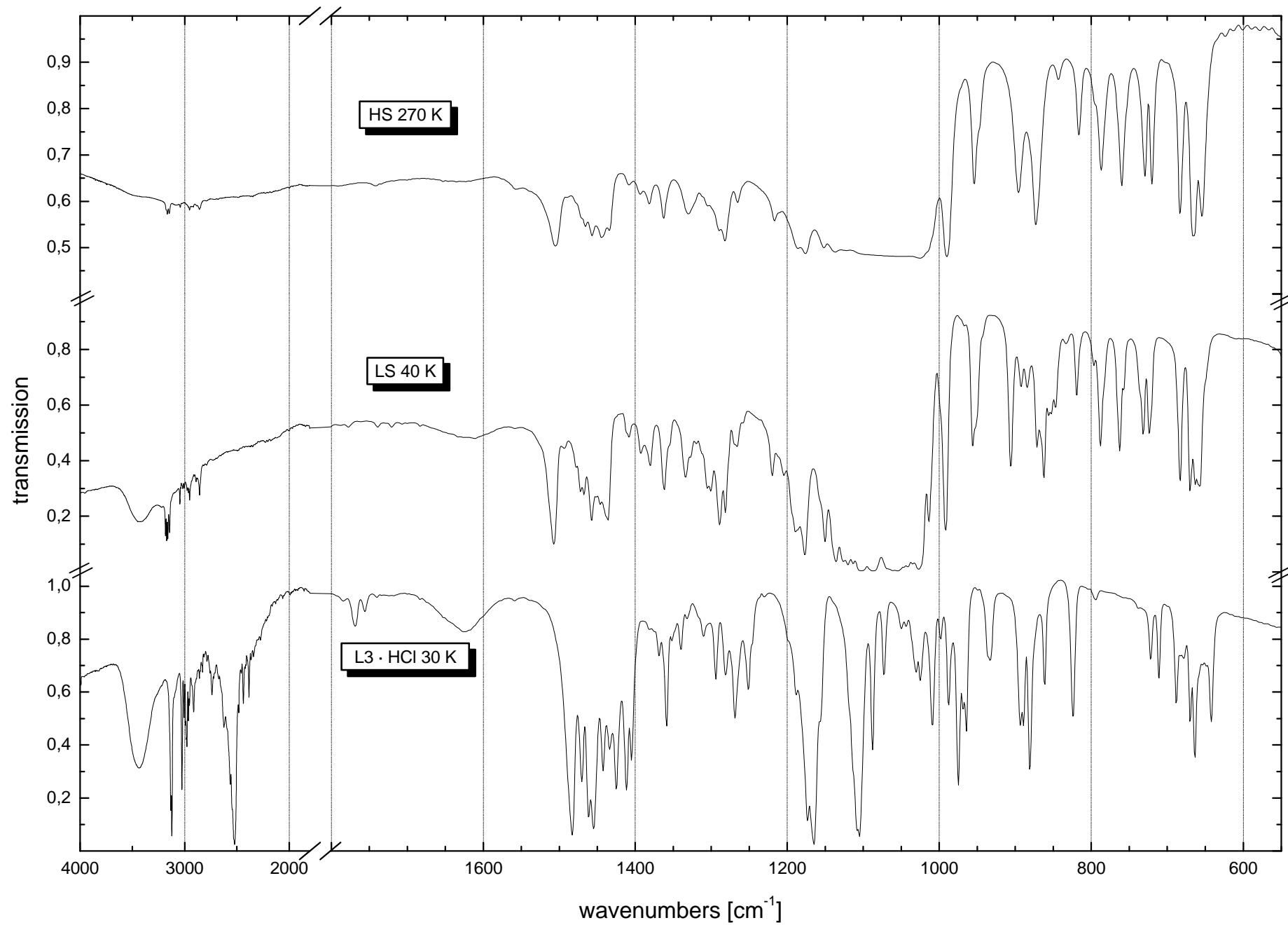


Figure 5.8: MIR spectra of $[\text{Fe}(\mathbf{L3})_2](\text{BF}_4)_2$ in HS and LS state and the hydrochloride of the pure ligand.

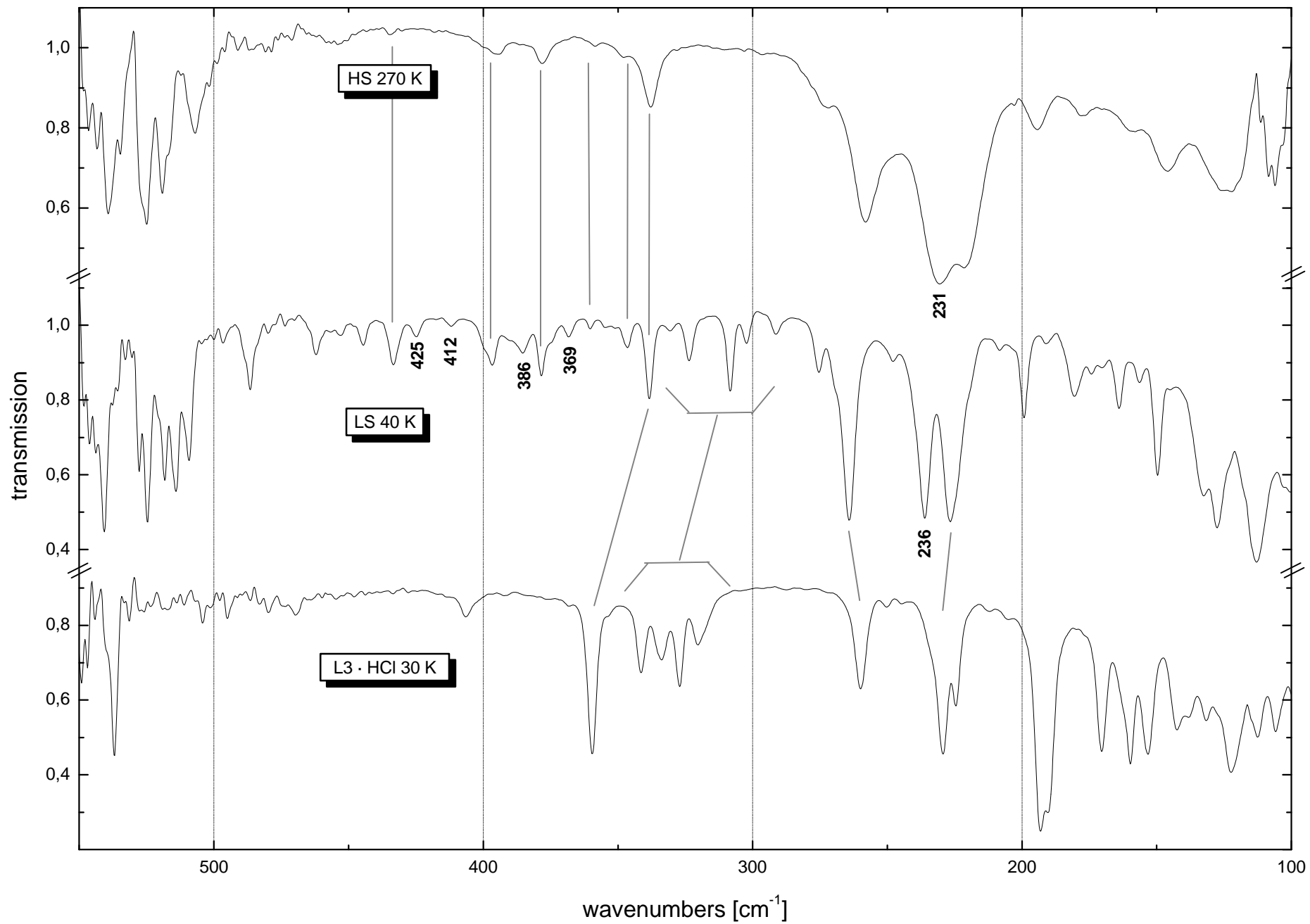


Figure 5.9: FIR spectra of $[\text{Fe}(\mathbf{L3})_2](\text{BF}_4)_2$ in HS and LS state and the hydrochloride of the pure ligand.

5.4 DFT calculations on (entz)₃N

In order to get some further information on the vibrational properties of the system the pure ligand (entz)₃N has been calculated with B3LYP/LanL2DZ. In table 5.1 the results are compared with the Raman and IR spectra of the pure ligand:

#	B3LYP/LanL2DZ	Raman (L3)	IR (L3 · HCl)	assignment
1	15,22,28,32,39, 45,63,73,79			torsions
2	100,116,156, 192,212,241	105,110,125,133, 155,170,242, 247, 259	106,113,122,132,138, 143,153,160,170,190, 193,225,230,260	Tz ip-rot. / ethyl rot.
3	304	277, 292		Tz oop-rot. / CH ₂ - rot.
4	335,358,363,380,412, 441,475	329,355,367,404, 415	320,327,334,341,359, 407,470	CH ₂ -rot. (+ Tz ip/ooop rot.)
5	546	531,538,558	536	CH ₂ -rot. + C-C-N bend
6	640			H wag. + CH ₂ -rot.
7	651, 665	644, 652	643,663,670	Tz wag. + CH ₂ -rot.
8	683,689,701,702,703	681	688	Tz wag.
9	719	725	711, 722	ip 1 / N-C str. (bridge)
10	783, 799	740	739, 795	CH ₂ -rot.
11	858,860,862	878	824,862,881	H wag.
12	888	893, 898	890, 894	CH ₂ -rot.
13	903,906,911			3-4 str.
14	936			C-C str.
15	944	943, 949	934	Ring str.+ CH ₂ rocking
16	965			C-C str.
17	970, 973	962,969,975	964,969,975	1-2 str.
18	996	981, 1000	987, 1009	ip 5 + ethyl bends
19	1029,1034,1041	1030	1025, 1031	ip 4 / ip 1
20	1051	1053		C-C str.
21	1067, 1079,1086		1073, 1087	CH ₂ - CH ₂ rocking
22	1126	1103,1108,1119	1107	ip H + 1-5 str. + CH ₂ rockg.
23	1138,1140,1154,1166, 1204,1210	1155, 1168	1158, 1166,1173,1187	2-3 str.
24	1220, 1237			H-C bend
25	1272,1305,1311,1324, 1345,1365,1377		1252,1269,1282,1294, 1310,1332,1341,1352, 1359,1369	H-C bend
26	1393,1399,1405,1414, 1416,1419,1425,1435		1405,1412,1425, 1433, 1443	H-C bend + ip H + 4-5 str.
27	1450,1456,1497,1512, 1516,1526,1529,1541		1455,1461,1471,1484	H-C bend + ip H + 1-5 str.
28	3018,3044,3049,3095, 3100,3109,3113,3164, 3172		2915,2955,2964, 2980,2983,2990, 3005, 3027	C-H str. (ethyl br.)
29	3331, 3334		3123, 3133	C-H str. (Tz)

Table 5.1: Calculated and experimental frequencies [cm⁻¹] of the pure ligand **L3** (numbering scheme: see Fig. 5.10).

Again the mode at $\sim 1030\text{ cm}^{-1}$ which has been used to monitor the spin state in the Raman measurements is assigned to a bend of the tetrazole ring, i.e. mainly an in-plane bend at the position of the coordinating nitrogen atom (#1, see fig. 5.10). Therefore, this mode also has Fe-N contributions (cf. the calculations on the $[\text{Fe}(\text{ptz})_6]^{2+}$ models and ligands in chapter 4).

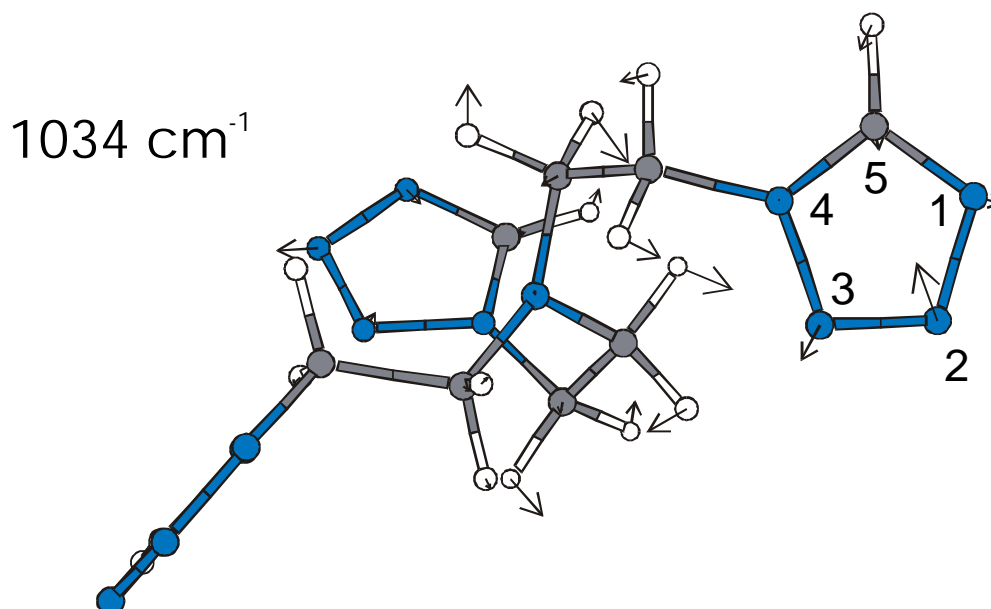


Figure 5.10: Calculated atom displacements of the in-plane tetrazole ring deformation.

The second important feature at around 850 cm^{-1} which was used to follow the structural phase transition, is connected to $\text{CH}_2 - \text{CH}_2$ - twisting rotations of the ethyl bridge, which experiences the 90 degrees “switch”. On the other hand the H - wagging of the tetrazole ring plays a significant role as well. Because of the turning of one tetrazole ring per ligand around 45 degrees during the phase transition, this mode feels the different lattices, too.

6 Results C: [Fe(phen)₂(NCS)₂]

6.1 The system [Fe(phen)₂(NCS)₂]

The first spin crossover system with Fe-II ions discovered in 1964 is the system [Fe(phen)₂(NCS)₂] (phen = 1, 10 - phenanthroline) [BAK64]. This spin crossover compound has been investigated many times.

Two different preparational routes are described in the literature [KÖN67, GAN81]: by precipitation (method A) a dark violet powder is obtained which shows an abrupt but incomplete spin transition with residual high-spin fractions of about 20% at low temperatures. In contrast, by extraction (method B) one obtains a complete spin transition centred around 176 K with a very small hysteresis (< 1 K) [MÜL82]. This spin transition is very sensitive to mechanical treatment of the sample like pressing or grinding [MÜL82], leading to residual HS fractions after the treatment. This fact has to be taken into account when preparing samples for the infrared spectroscopic measurements.

Crystal structures at 293 and 130 K [SOR74, GAL90] reveal shortening of the Fe-N bonds by $\Delta r = 0.2/0.1$ Å for the Fe-phen and the Fe-NCS bond, respectively, when going from HS to LS state [Fe-N(phen) = 2.206 Å (HS) / 2.009 Å (LS) and Fe-N(CS) = 2.057 Å (HS) / 1.958 Å (LS)]. The spin transition is also accompanied by a shortening of the C-N bond length of the thiocyanate group from 1.158 Å (HS) to 1.14 Å (LS) and a slight lengthening of the C-S bond from 1.628 Å (HS) to 1.632 Å (LS). The space group *Pbcn* (*Z*=4) is the same in both spin states. The compound shows the LIESST effect at temperatures below 50K as measured by Mössbauer spectroscopy [DEC85b].

Changes in the thermodynamic data have been determined by heat capacity measurements to be $\Delta H_{HL} = 8.60$ kJ/mol and $\Delta S_{HL} = 48.78$ J/K/mol [SOR74].

Infrared spectroscopic measurements revealed a shift of the C-N stretch in the 2000 cm⁻¹ region of about 40 cm⁻¹ between HS and LS state [KÖN67]. This became a 'probe' vibration for spin crossover systems containing NCS to monitor the spin transition.

In the course of their investigation of vibrational properties using infrared spectroscopy *Takemoto et al.* [TAK72, TAK73, TAK74] assign a shift from 220 cm⁻¹ (HS) to 375 cm⁻¹ (LS) to the Fe-N(phen) and from 252 cm⁻¹ (HS) to 530 cm⁻¹ (LS) to the Fe-N(CS) stretching vibration on the basis of metal isotope substitutions. As explained in the introductory chapter 1.2 especially the latter assignment has to be doubted, because this shift would correspond to a factor of ~4.4 between the harmonic force constants in HS and LS state.

During FT-IR spectroscopic measurements in 1986 *Herber et al.* [HER86] noticed the influence of the He/Ne laser light (632 nm) used for calibration of the interferometer: [Fe(phen)₂(NCS)₂] showed a significant excitation of the meta-stable LIESST-state below 32K. This fact complicates the interpretation of the FT-IR measurements described later on in this chapter.

6.2 Infrared spectroscopy

In figures 6.1 and 6.2 the far and middle infrared spectra of [Fe(phen)₂(NCS)₂] at room temperature and 25 K (before and after irradiation with green light) as well as the pure ligand 1,10-phenanthroline in CsJ pellets are depicted. Bold numbers indicate modes that are sensitive to isotope substitution (i.e. ¹⁵N¹³CS).

Due to the known problems caused by pressing during pellet preparation [MÜL82] as well as the LIESST excitation by the 632 nm He/Ne laser light of the interferometer [HER86] at low temperatures, no spectrum could be obtained that solely contains the LS state. The residual HS fraction can be observed at the C-N-stretch probe vibrations at 2064/2075 cm⁻¹ of the HS state compared to the corresponding vibrations of the LS state at 2106/2113 cm⁻¹ (cf. figure 6.2).

A nujol mull between polyethylene discs at 70 K should only be composed of LS, but here the probe vibration (C-N stretch in the middle infrared) can not be used unequivocally, because of nujol bands in this region. The FIR spectrum of the mull looks more or less the same as the spectrum in CsJ displayed in figure 6.1. The periodic modulation of the background of the spectrum of the pure ligand is due to interference of the IR beam at the parallel surfaces of the pellet.

The spectra obtained are similar to those published by *Takemoto et al.* [TAK72]. Additionally, the FIR and MIR spectra of the LIESST state have been measured. There are only slight differences between the spectra of the LIESST and the thermal HS state. Mainly the low energetic vibrations below 300 cm⁻¹ appear up to 4 cm⁻¹ higher in energy and have a smaller line width.

In the low frequency region (< 300 cm⁻¹) the NCS group is involved in several modes, which also contain other metal-ligand vibrations (e.g. M-phen) and bends of the 'octahedron', i.e. the modes in this region are highly coupled. This leads to isotope shifts (¹⁵N¹³CS substitution) of 1 - 3 cm⁻¹ of the 160, 226 and 254 cm⁻¹ bands in the HS state as well as the 212, 235 and 244 cm⁻¹ modes in the LS state.

In the following, statements and assignments like Fe-N(phen) or Fe-N(CS) mode are proposed with the understanding that the vibrational modes in this spectral region are highly coupled and thereby there could be several vibrations with significant involvement of the elongation of the iron-nitrogen bond. The designation as Fe-N(phen) or Fe-N(CS) mode therefore only means a major involvement of the Fe-N(phen) or Fe-N(CS) bond in the displacement of the addressed vibration.

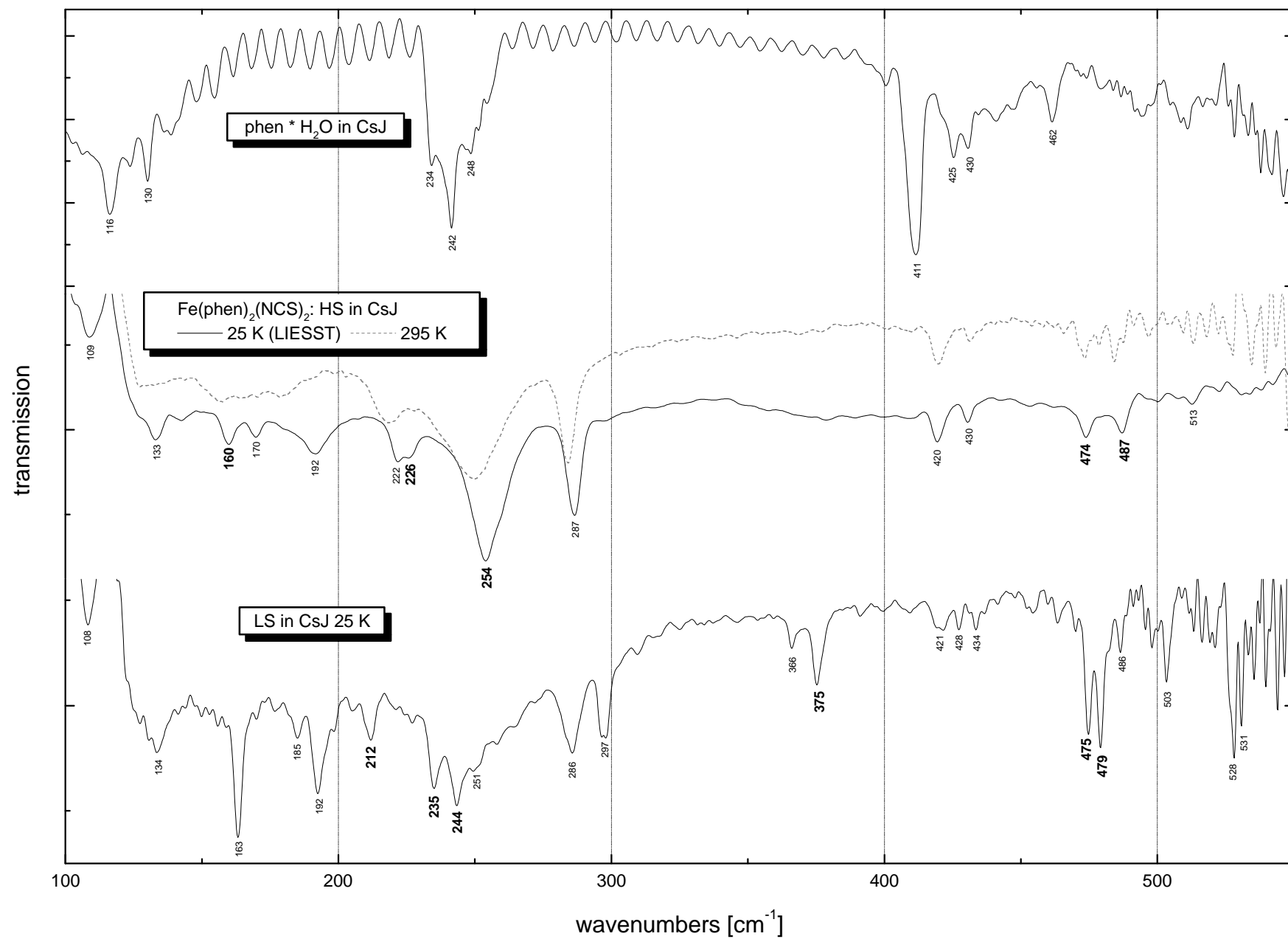


Figure 6.1: Far infrared spectra of [Fe(phen)₂(NCS)₂] and the pure ligand. [Bold numbers indicate modes sensitive to (¹⁵N¹³CS) substitution.]

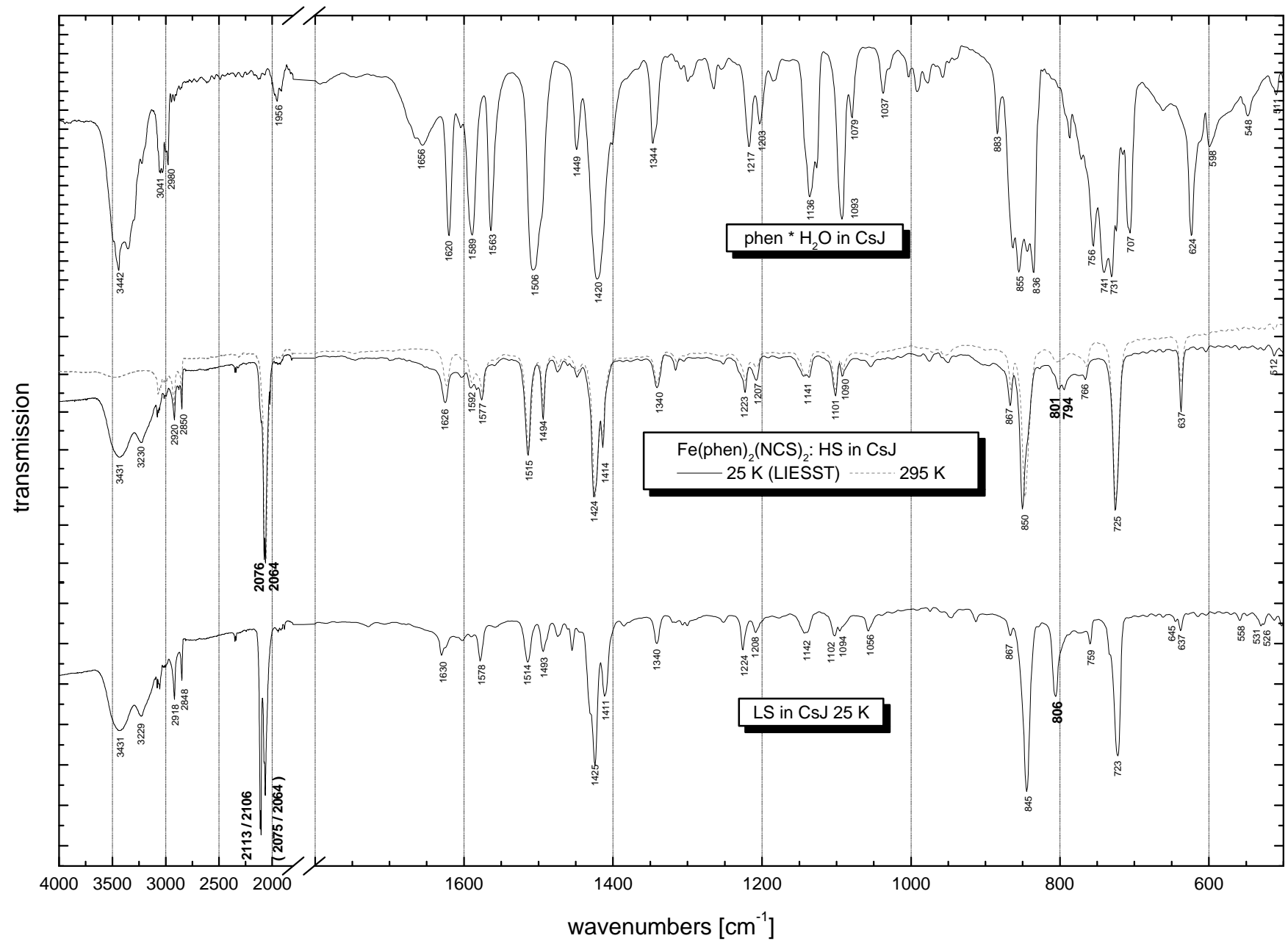


Figure 6.2: Middle infrared spectra of [Fe(phen)₂(NCS)₂] and the pure ligand. [Bold numbers indicate modes sensitive to (¹⁵N¹³CS) substitution.]

6.3 Raman spectroscopy

In figures 6.3 and 6.4 the Raman spectra of $[\text{Fe}(\text{phen})_2(\text{NCS})_2]$ in both spin states and the pure ligand 1,10-phenanthroline monohydrate are presented.

The excitation wavelength of 514 nm even at 80 K leads to a significant population of the LIESST state, seen from the intensity of the C-N-stretch probe vibration of the HS state at 2073 cm^{-1} . A comparison of the spectra of the two spin states is possible using two different excitation wavelengths: 514 nm for the LIESST state at 30 K and 799 nm for the LS state at 80 K. These conditions lead to pure HS and LS spectra, respectively.

Besides the C-N-stretch, significant differences between the spectra of the two spin states can be observed in the low frequency region (figure 6.3). Similar to the noted differences in the infrared spectra (cf. figure 6.1) the pattern at 220 and 252 cm^{-1} in the HS state and the modes at 368 and 376 cm^{-1} in the LS state are observed in the corresponding Raman spectra.

Peaks of bands at 116, 131, 181, 420, 478, 496, 558, 639, and 864 cm^{-1} in the HS spectrum at 30 K are not observed in the LS spectrum at 80 K, and vice versa the modes at 123, 139, 164, 197, 299, 311, 430, 561, 646, 740 and 880 cm^{-1} of the LS spectrum at 80 K are absent in the HS spectrum. Furthermore, some small shifts in the $1000 - 1700\text{ cm}^{-1}$ region are observed (cf. figure 6.4).

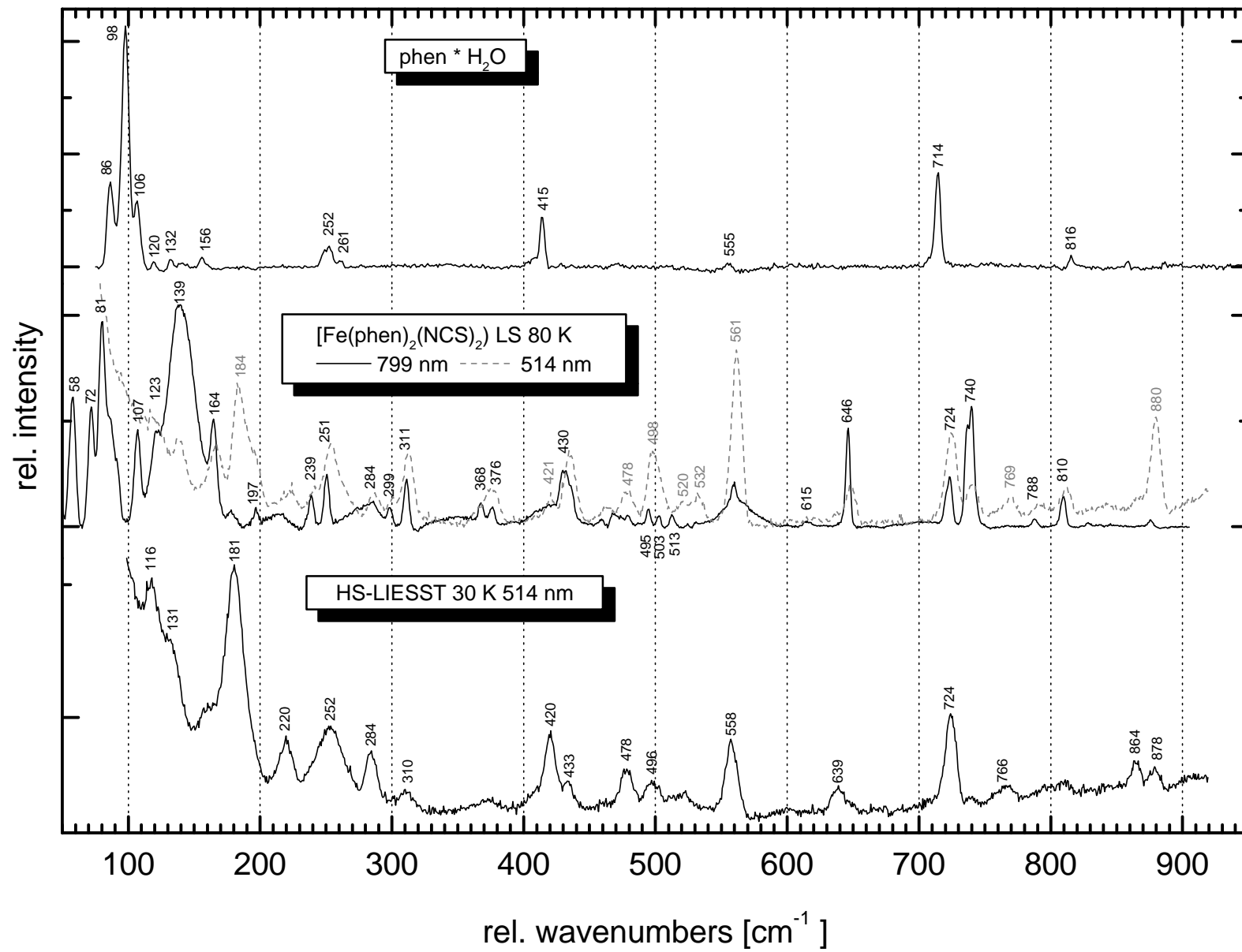


Figure 6.3: Low frequency Raman spectra of [Fe(phen)₂(NCS)₂] and the pure ligand.

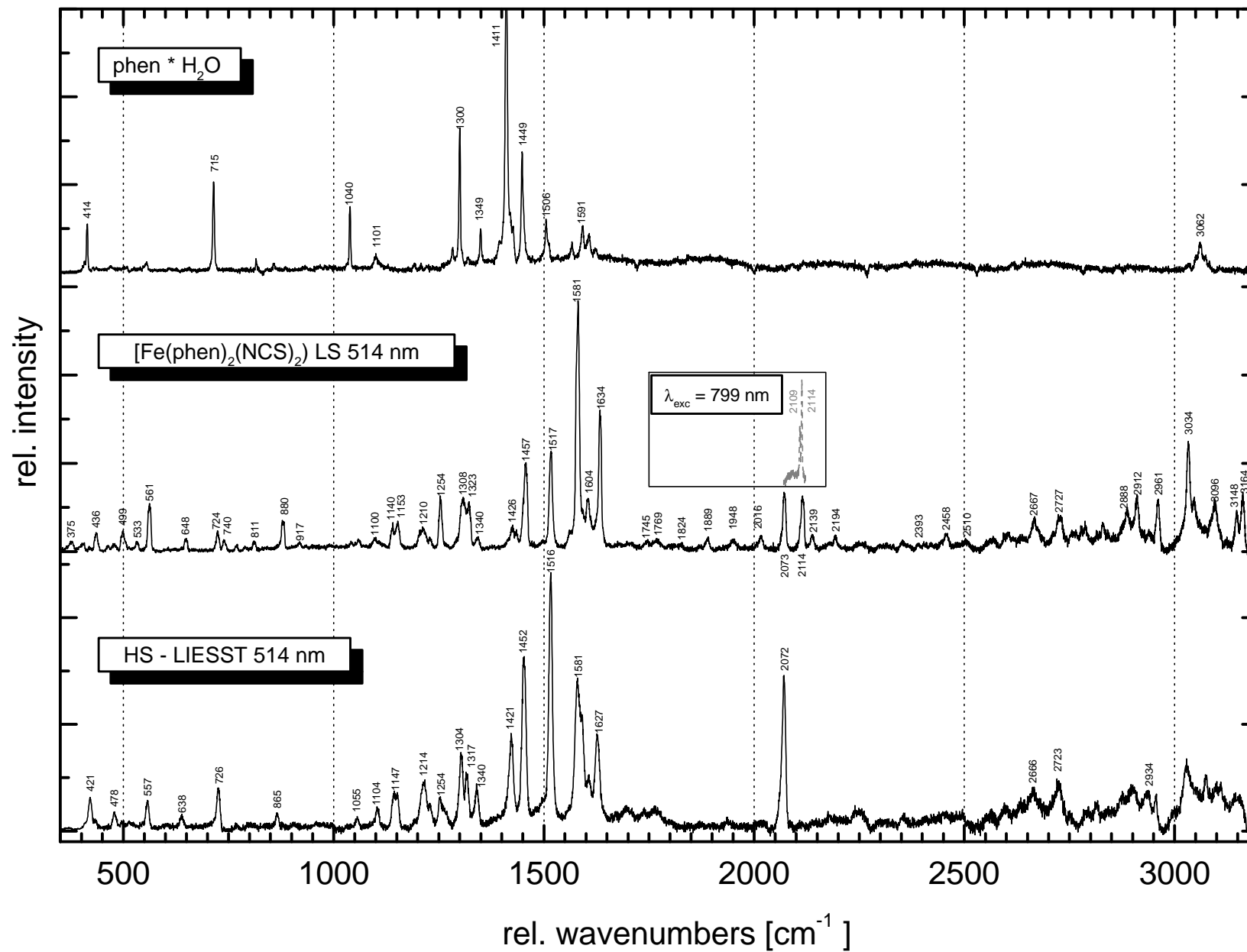


Figure 6.4: High frequency Raman spectra of [Fe(phen)₂(NCS)₂] at 80K (LS) and 30K (HS) and the pure ligand at 80K.

Additional information can be extracted from the spectra at 80 K with the 514 nm excitation in comparison to the spectra with 799 nm excitation wavelength. Due to the iron to phenanthroline charge transfer transition in the green region of the visible light, different vibrations show a resonance enhancement of their intensity.

The resonance Raman scattering in general leads to an intensity enhancement of vibrations which are involved in the displacement of the excited state of the considered charge-transfer. Because of this resonance enhancement combinations and overtones of these modes might be detected as well. Therefore, the observed enhancement might contribute to an assignment of modes connected to the iron to phenanthroline charge transfer.

In order to determine the modes which are resonance enhanced, first of all one has to consider the presence of a HS fraction in the 514 nm spectra. The low frequency spectra show significant HS modes at 181, 220, 252, 284, 478 and 724 cm⁻¹. For comparison with the 799 nm spectrum the 514 nm spectrum at 80 K has to be corrected for a systematic shift of about 3 cm⁻¹ to higher energies caused by an erroneous manual reading of the absolute positions of the gratings of the monochromator. The intensities of the LS vibrations with the two different excitation wavelengths cannot be compared directly, because they do not have an absolute scale. The scaling factor between the intensities at different excitation wavelengths has not been determined. In order to see all details the scaling factor between the two spectra in figure 6.3 is chosen in a way that both spectra use the whole range of space of the plot. This leads to peak heights of the modes at 139, 646 and 740 cm⁻¹ which are larger at $\lambda_{\text{exc}} = 799$ nm than at $\lambda_{\text{exc}} = 514$ nm. Because of a resonance enhancement at $\lambda_{\text{exc}} = 514$ nm intensities of some modes can exceed the intensities measured at $\lambda_{\text{exc}} = 799$ nm, but not the other way round.

Taking these three modes not to be resonance enhanced, the spectrum at $\lambda_{\text{exc}} = 799$ nm must be scaled down by at least a factor of 2. In case there is resonance enhancement of these frequencies the scaling factor is even larger.

Subtracting the HS fraction in the 514 nm spectrum and scaling down the intensities, several modes are obviously enhanced. The modes at 880 and 561 cm⁻¹ are enhanced by almost two and more than one order of magnitude, respectively (cf. figure 6.3). Also the modes at 164, 311, 368, 375, 430, 495, 520, 532 cm⁻¹ are significantly resonance enhanced.

A second hint at resonance enhancement of vibrations is given by the possible occurrence of overtones and combinations of these modes. An assignment of overtones and combinations in connection with the iron to phenanthroline charge transfer has been studied in detail on the [Fe^{LS}(phen)₃]²⁺ ion by *Clark et al.* [CLA77]. In analogy, the observed overtones and combinations of [Fe(phen)₂(NCS)₂] (figure 6.4) are assigned. These assignments are summarised in table 6.1.

[Fe^{LS}(phen)₂(NCS)₂] this work		[Fe^{LS}(phen)₃]²⁺ [CLA77]	
<i>n</i> [cm ⁻¹]	<i>Assignment</i> [cm ⁻¹]	<i>n</i> [cm ⁻¹]	<i>Assignment</i> [cm ⁻¹]
368	Fe-N(phen)	369	
375			
520			
532			
561		560	
646		647	
724		727	
740		739	
880		880	
917	561 + 368	915	
1100	2 x 561	1094	
1745	2 x 880		
1824	1457 + 368 /375		
1889	1517 + 368 /375		
1948	1581 + 368 /375		
2016	1457 + 561	2016	1458 + 560
2073	1517 + 561	2072	1517 + 560
2139	1581 + 561	2138	1582 + 560
2194	1634 + 561	2193	1635 + 560
2334	1457 + 880	2334	1458 + 880
2393	1517 + 880	2393	1517 + 880
2458	1581 + 880	2456	1582 + 880
2510	1634 + 880	2512	1635 + 880
2912	2 x 1457	2911	2 x 1458
2961	1517 + 1457	2966	1517 + 1458
3034	2 x 1517	3032	2 x 1517
3096	1634 + 1457 / 1581 + 1517	3095	1635+1458/1582+1517
3148	1635 + 1517	3151	1635 + 1517
3164	2 x 1581		

Table 6.1: Selected frequencies of resonance enhanced fundamentals, overtones and combinations [cm⁻¹] at 80 K with $\lambda_{\text{exc}}=514\text{nm}$ in comparison with literature data of *Clark* [CLA77].

The resonance enhancement of these modes indicates their involvement into the displacement of the excited state of the iron to phenanthroline charge-transfer. Therefore, it contributes to the assignment, that the metal-nitrogen bond stretch participates significantly in these modes. In particular, the modes at 368 and 561 cm⁻¹ will play an important role (in the next chapter) in the discussion of the infrared spectra and the assignments published in the literature.

6.4 Discussion C

The system [Fe(phen)₂(NCS)₂] and different kinds of derivatives of this compound have extensively been studied by infrared spectroscopy in the literature. *Takemoto et al.* [TAK72] investigated [Fe(phen)₂(NCS)₂] with its metal-isotope shift data (⁵⁴Fe - ⁵⁷Fe) and assigned the metal ligand stretching vibrations according to the shifts on isotope substitution (stated in brackets below) to 220 cm⁻¹ (4.5 cm⁻¹) for [Fe-N(phen)] and 252 cm⁻¹ (4.0 cm⁻¹) for [Fe-N(CS)] in the HS state and 371/379 cm⁻¹ (6.0/5.0 cm⁻¹) for [Fe-N(phen)] and 528/532 cm⁻¹ (1.7/1.8 cm⁻¹) for [Fe-N(CS)] in the LS state (all frequencies correspond to the ⁵⁴Fe isotope spectra).

This latter assignment is inconsistent for the following reasons. According to the small shift due to metal-isotope substitution of about 1.75 cm⁻¹ the Fe-N(CS) stretch in the LS state was assigned to 528/532 cm⁻¹, whereas the analogous mode in the HS state shifts about 4 cm⁻¹. This makes the proposed assignment doubtful. A splitting of the single line at 220 cm⁻¹ in HS state of the metal-phenanthroline stretch into two modes at 375 and 366 cm⁻¹ in the (even higher symmetric, i.e. more regular octahedral shaped [GAL90]) LS state is also not expected.

The data published in the three articles [TAK72, TAK73, TAK74] are inconsistent. The authors compare [Fe(phen)₂(NCS)₂] to [Fe(phen)₂(NCSe)₂], [Fe(bipy)₂(NCS)₂], [Fe(bipy)₂(CN)₂], [Fe^{HS}(phen)₂(NCO)₂], [Fe^{LS}(phen)₂(CNO)₂] and [Fe^{LS}(phen)₂(CN)₂].

Takemoto et al. found no influence on the ~530 cm⁻¹ vibration when replacing NCS by CNO or NCSe. Even [Fe^{LS}(phen)₂(CN)₂] contains two modes in this frequency range at 523/541 cm⁻¹, whereas the Fe-N(CS) stretch on substitution of phenanthroline by bipyridine was assigned to the much lower frequencies at 492/498 cm⁻¹ in [Fe(bipy)₂(NCS)₂]. A metal-ligand stretching vibration must be influenced by such large deviations in the mass of the ligands NCS, CNO or NCSe. On the other hand, different α -diimine ligands are not expected to shift the Fe-N(CS) vibration by even more than 30 cm⁻¹.

Additionally, the infrared spectroscopic data on [Fe(phen)₃]²⁺, [Fe(bipy)₃]²⁺ [HUT70], [Fe^{III}(phen)₃]³⁺ and [Fe^{III}(bipy)₃]³⁺ [SAI72] have been known. The substitution of phenanthroline by bipyridine shifts the Fe-N(α -diimine) stretching vibrations by only 12-17 cm⁻¹. The influence of such a variation in [Fe(phen)₂(NCS)₂] on the Fe-N(CS) vibration should be even smaller.

There exists a further argument comparing Fe(II) and Fe(III) complexes. The spectra of [Fe^{II}(phen)₃](ClO₄)₂ and [Fe^{III}(phen)₃](ClO₄)₃ [HUT70, SAI72] reveal a two mode pattern in the region of interest. In these compounds Fe(II) shows a lower energetic band with high intensity at 359 cm⁻¹ accompanied by a weak higher energetic mode at 374 cm⁻¹, whereas Fe(III) exhibits an intensity ratio just the other way round: a strong line at 374 cm⁻¹ is accompanied by the weak lower energetic vibration at 354 cm⁻¹. Obviously, a two mode pattern belongs to the Fe-phen vibration and its intensity ratio depends on the charge state. In the two mode pattern in [Fe^{II}(phen)₂(NCS)₂] the higher energetic vibration at 375 cm⁻¹ is much more

intense than the one at 366 cm^{-1} . The same structure is found in the HS state at the frequencies 254 and 222 cm^{-1} . (The frequencies of $[\text{Fe}^{\text{II}}(\text{phen})_2(\text{NCS})_2]$ belong to the compound with natural iron isotope composition as displayed in figure 6.1.) If the two mode pattern for the Fe^{II} -phen vibrations in $[\text{Fe}(\text{phen})_2(\text{NCS})_2]$ and in $[\text{Fe}(\text{phen})_3](\text{ClO}_4)_2$ have the same intensity ratios, subtraction of the Fe^{II} -phen pattern of $[\text{Fe}(\text{phen})_3](\text{ClO}_4)_2$ scaled down to the lower energetic mode of $[\text{Fe}(\text{phen})_2(\text{NCS})_2]$ leaves the major part of intensity of the higher energetic mode at 375 cm^{-1} .

The further observation that the 375 cm^{-1} mode shows an isotope shift of 1 cm^{-1} on substitution of the isothiocyanate (i.e. $^{15}\text{N}^{13}\text{CS}$) and the mode at 366 cm^{-1} (cf. figure 6.1) does not, makes it *necessary to assign the Fe-N(CS) stretch to the 375 cm^{-1} mode and the vibration at 366 cm^{-1} to the Fe-N(phen) stretch*. Of course, the denomination of the vibrations again is only meant in terms of a main contribution of this motion to the normal mode, being aware of a strong coupling between the low-energetic modes.

What about the previously assigned feature centred around 530 cm^{-1} ? The pure ligand 1,10-phenanthroline shows modes at 511 , 548 , 598 and 624 cm^{-1} . According to the density functional calculations on a simplified model presented in chapter 7, these modes are assigned to in-plane bends of the aromatic ligand. The corresponding vibrations in the complex molecule are observed at 512 and 637 cm^{-1} (HS) and 503 , 526 , 531 , 637 and 645 cm^{-1} (LS), respectively (cf. figure 6.2). These in-plane bends partly have a remarkable participation of the Fe-N bond (see chapter 7), which results in a still detectable frequency shift on metal isotope substitution. Moreover, the missing influence of the $^{15}\text{N}^{13}\text{CS}$ substitution on these bands clearly rules out an involvement of the isothiocyanate in the modes at 526 and 531 cm^{-1} in the LS spectra.

The resonance enhancement of the 368 , 503 , 520 , 532 and 561 cm^{-1} modes (LS) in the Raman spectra shown in the previous chapter also supports these assignments. The resonance enhancement of the 375 cm^{-1} mode does not necessarily disprove the assignment to the Fe-N(CS) stretch, because of mixing with the Fe-N(phen) stretch.

Table 6.2 summarizes the new assignments in comparison with results of calculations, which are presented in the next chapter.

mode	$[\text{Fe}(\text{phen})_2(\text{NCS})_2]$				$[\text{Fe}(\text{phen})_2$ $(^{15}\text{N}^{13}\text{CS})_2]$		$[\text{Fe}(\text{phen})_2(\text{NCS})_2]$ [PAU99]			
	<i>experimental</i>		<i>calculated *</i>		<i>experimental</i>		<i>calculated **</i>		Dn ($^{15}\text{N}^{13}\text{CS}$)	
	LIESST	LS	HS	LS	LIESST	LS	HS	LS	HS	LS
$\delta(\text{NCS})$	474/ 487	475/ 479	441- 459	425- 449	457/ 469	459/ 462	551/ 543	528/ 513	-29/ -24	-30/ -17
$\nu(\text{C-S})$	794/ 801	806	791/ 806	781/ 788	785	787	883/ 880	867/ 862	-20	-20
$\nu(\text{C-N})$	2064/ 2076	2106/ 2113	2063/ 2081	2123/ 2138	1987/ 1999	2029/ 2037	2128/ 2118	2173/ 2163	-78/ -79	-80
$\nu(\text{Fe-N}(\text{phen}))$	222	366	213/ 225	318/ 416	222	366	290/ 305	375/ 387	0	-1/0
$\nu(\text{Fe-NCS})$	254	375	237/ 286	264/ 371	252	374	274/ 282	392	-1	-1

Table 6.2: Comparison of selected experimental (IR) and calculated vibrations [cm^{-1}].
(* DFT calculations (LanL2DZ) on a simplified model presented in detail in the next chapter. ** DFT calculations (3-21G*) on the complete molecule [PAU99])

In table 6.3 the frequencies of interest of $[\text{Fe}(\text{phen})_2(\text{NCS})_2]$ in both spin states measured by Raman spectroscopy are tabulated. These are compared to the Raman frequencies of KSCN, $[\text{Fe}(\text{phen})_3]^{2+}$ [CLA77] and some values on the isotope labelled complex with $^{15}\text{N}^{13}\text{CS}$ groups [DEN00]. The frequencies of the two spin states are ascribed according to the assignments of the infrared measurements.

mode	$[\text{Fe}(\text{phen})_2(\text{NCS})_2]$		$[\text{Fe}(\text{phen})_2(^{15}\text{N}^{13}\text{CS})_2]$ ([DEN00])		KSCN	$[\text{Fe}(\text{phen})_3]^{2+}$ ([CLA77])
	HS	LS	HS	LS		
$\delta(\text{NCS})$	478/496	478/495		465	488	
$\nu(\text{C-S})$		810	792	794	751	
$\nu(\text{C-N})$	2072	2109/2114	1991	2039	2052/2055	
$\nu(\text{Fe-N}(\text{phen}))$	220	368				369
$\nu(\text{Fe-NCS})$	252	376				

Table 6.3: Assignment of selected experimental values [cm^{-1}] obtained by Raman spectroscopy.

7 DFT calculations on α -diimine systems

As a general simplified model for the previously treated $[\text{Fe}(\text{phen})_2(\text{NCS})_2]$ as well as the series of compounds $[\text{Fe}(\text{PM-R})_2(\text{NCS})_2]$ with different N-(2-pyridylmethylene)amino derivative ligands PM-R presented in the next chapter, the following system (denoted as $[\text{Fe}^{\text{II}}(\text{PM-H})(\text{diimine})(\text{NCS})_2]$) has been calculated for HS and LS with the use of B3LYP/LanL2DZ:

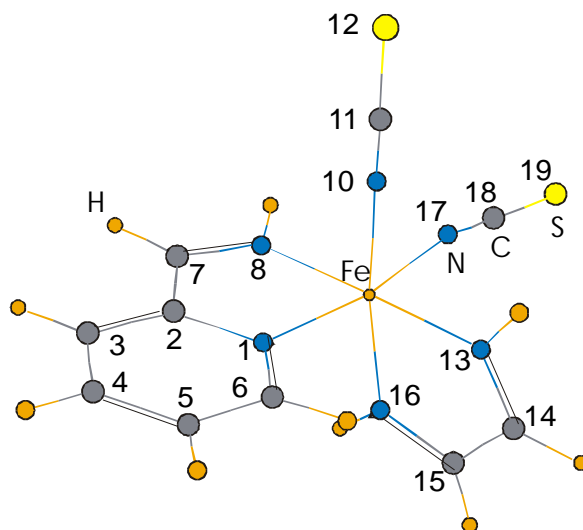


Figure 7.1: Numbering scheme of the model.

	<i>HS</i>	<i>LS</i>
r [Fe-N(PM-H)] [\AA]	2.33/2.20	2.00/1.93
r [Fe-N(diimine)] [\AA]	2.09/2.16	1.93
r [Fe-N(NCS)] [\AA]	2.01/2.03	1.94/1.95
f [Fe-N(PM-H)] [mdyn/\AA]	0.72/0.85	1.508 / 1.862
f [Fe-N(diimine)] [mdyn/\AA]	1.11/0.93	2.08
f [Fe-N(NCS)] [mdyn/\AA]	1.20/1.36	1.39 / 1.50
ν_s (Fe--PM-H/diimine)	213	416
ν_s (Fe--diimine/NCS)	225	318
ν_s (Fe--PM-H/NCS)	237	264
ν_{as} (Fe--PM-H/diimine)	348	467
ν_{as} (Fe--diimine/NCS)	286	371
ν_{as} (Fe--PM-H/NCS)	304	390
δ (NCS)	441/449/454/459	425/433/439/449
ν (NC-S)	791/806	781 / 788
ν (N-CS)	2063/2081	2123 / 2138
i.p.N(PM-H)*	487 / 648 / 1014	521 / 663 / 1031
i.p.N(diimine)*	490	564
α -diimine stretches*	1512 / 1584 / 1604	1528 / 1592 / 1594
(incl. PM-H)	1627 / 1672	1629 / 1653

Table 7.1: Selected calculated bond lengths [\AA], force constants [mdyn/\AA] and vibrational frequencies [cm^{-1}] of the $[\text{Fe}^{\text{II}}(\text{PM-H})(\text{diimine})(\text{NCS})_2]$ model. * indicates ligand modes with partial M-L character (see text).

Table 7.1 summarises the most important frequencies and force constants from these calculations. A survey of all calculated frequencies and their assignment together with the results on the pure ligand PM-H is given in the appendix (cf. chapter A.3).

As already mentioned during the discussion of the assignments on $[\text{Fe}(\text{phen})_2(\text{NCS})_2]$ the intraligand modes with metal-ligand participation (marked by an asterisk in the above table) are of special interest. On the one hand they might get quite low in energy, and therefore have to be taken into account for the low frequency assignments. On the other hand they may serve as a probe vibration in the higher energetic part to monitor the spin transition. One example of such a mode is depicted in figure 7.2.

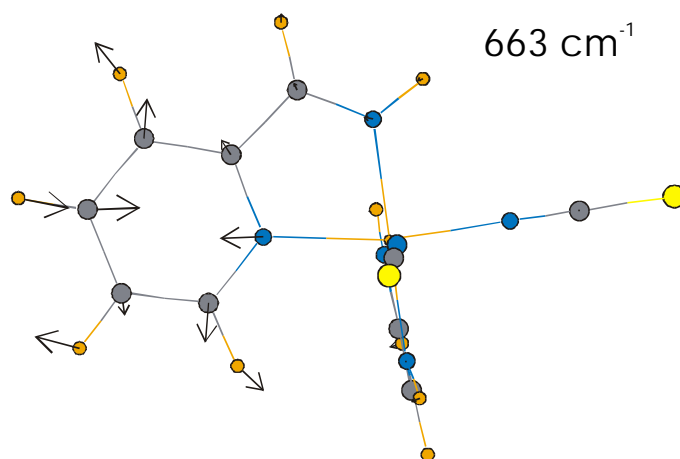


Figure 7.2: Intraligand mode with partial M-L character.

A comparison of the calculated force constants in the high-spin and low-spin state, respectively, reveals a factor of about 2 in the force constants for the metal-diimine bond (including PM-H), whereas the M-N(CS) bond shows only slight variations. This is in agreement with the less pronounced changes in the metal-ligand bond lengths as observed by X-ray crystallography e.g. on $[\text{Fe}(\text{phen})_2(\text{NCS})_2]$ [GAL90]. It must be mentioned, that the extracted force constant matrix in internal coordinates contains partially high off-diagonal elements, i.e. up to 30 % of the diagonal values for the HS and up to 80 % for the LS. Nevertheless, the obtained values for the Fe-N stretching force constants fit perfectly within the range of the comparable quantities obtained so far.

The values for the C-N stretches of the isothiocyanate groups conform very well to those observed and used to monitor the spin crossover by vibrational spectroscopy.

Table 7.2 summarises the calculated electronic energies and the entropies at 170 K of the given model:

	HS	LS	D_{HL}
E(B+HF-LYP)	-859.183148 H/particle	-859.185214 H/particle	5.42 kJ/mol
Zero-point vib.energy	522.3871 kJ/mol	534.4954 kJ/mol	-12.11 kJ/mol
S_{elec.} [J/mol/K]	3.198	0	13.39
S_{vib.} [J/mol/K]	229.072	163.356	65.72

Table 7.2: Thermoanalysis of the model (entropy values at 170 K).

The electronic energies sum up to $\Delta E_{HL} = -6.69$ kJ/mol (i.e. -559 cm⁻¹). This means, that the simplifications introduced on the ligands in this model lead to a high-spin ground state. Nevertheless, the vibrational results can be used for comparison of the two spin states. The rather large vibrational contribution to the entropy difference between the two spin states is in agreement with the big change in bond length measured on [Fe(PM-BiA)₂(NCS)₂] (see below) and matches the value from DSC measurements of $\Delta S = 58.99$ J/mol/K on the same compound [LET98].

8 Results D: $[\text{Fe}^{\text{II}}(\text{PM-R})_2(\text{NCS})_2]$ series

The mononuclear iron(II) complexes with two N-(2-pyridylmethylene)amino derivative ligands and two cis-NCS groups partially show very abrupt spin transitions with differently pronounced thermal hysteresis depending on the ligand substituent [LET97, LET97b, KSE98 LET99]. The metal-ligand distance in one case ($\text{R} = \text{BiA}$) changes by about 0.28 \AA when going from high-spin to low-spin state [LET98]. This is rather high compared to other spin crossover systems and therefore leads to the expectation of even more pronounced frequency shifts in the vibrational spectra.

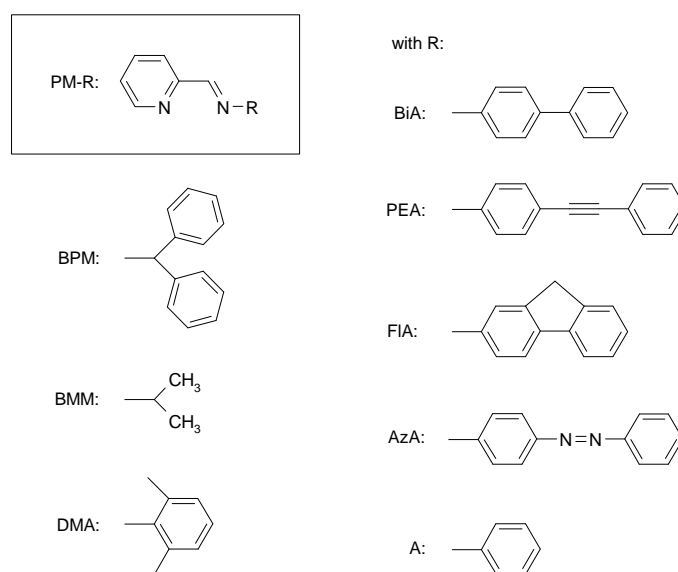


Figure 8.1: Sketches of the different derivatives of the $[\text{Fe}^{\text{II}}(\text{PM-R})_2(\text{NCS})_2]$ series.

In order to assign some of the intramolecular vibrations governing the spin crossover, temperature dependent Raman- and FTIR-spectra (middle and far IR) of the complete series of compounds have been recorded. Additionally, some of the pure ligands have been investigated.

8.1 [Fe^{II}(PM-BiA)₂(NCS)₂]

The first system in this series of compounds, [Fe^{II}(PM-BiA)₂(NCS)₂], shows an abrupt and complete spin transition centred around 170 K with a hysteresis of 5 K [LET97, LET98]. The spin transition is accompanied by a change in the metal-ligand bond length of $\Delta r_{\text{HL}} = 0.266 / 0.285 \text{ \AA}$ (PM-BiA) and $\sim 0.1 \text{ \AA}$ (NCS), respectively, retaining the space group *Pccn*. The largely pronounced differences between the two spin states are also reflected in an entropy change of about 59 J/mol/K.

The UV/Vis spectra are governed by strong MLCT absorptions at all temperatures, which cover the less intense d-d transitions. Therefore, irradiation with any light in the 450-800 nm range leads to the population of the LIESST state at temperatures below 50 K.

Figures 8.2 - 8.5 depict the low and high frequency Raman as well as the far- and middle-infrared spectra in both spin states in comparison with the spectra of the pure ligand PM-BiA. (In the infrared spectra the 'LS' labelled spectrum obviously still contains some amount of HS species, and the 'LIESST' spectrum is not free of LS contributions).

The ligand reveals several modes in the 100 - 500 cm⁻¹ region, too. This makes it difficult to distinguish between intra-ligand vibrations and frequencies of the FeN₆ core. If possible at all, the modes at 151, 207, 326 cm⁻¹ (HS) and 237, 342, 369 cm⁻¹ (LS) in the Raman spectra and 246, 259, 271 (HS) and 342, 364, 368 cm⁻¹ (LS) in the FIR are connected to movements of the octahedral unit. As already described in previous spectra (cf. propyltetrazole system above) an intra-ligand mode (386 cm⁻¹ in the pure ligand FIR spectrum) appears at 379 cm⁻¹ in the HS state and is shifted to 388 cm⁻¹ in the LS spectrum due to interaction with the Fe-N mode.

It is difficult to assign the NCS-bend, because of a PM-BiA ligand mode at 480 cm⁻¹, which is exactly the expected position for the NCS-bend. The quite simple feature at 438, 469 and 478 cm⁻¹ (HS) is shifted to the more complicated pattern of 447, 453, 458, 473 and 487 cm⁻¹ (LS), probably involving the mentioned intra-ligand mode as well as the $\delta(\text{NCS})$ vibration.

In the high energetic region of the spectra several changes occur with the spin conversion. Besides the C-N-stretch at $\sim 2100 \text{ cm}^{-1}$ the significant changes in the α -diimine stretching region (1500 - 1700 cm⁻¹) (as already assigned in the Raman spectra of several low-spin complexes [BAT83] as well as the spin crossover compound [Fe(6Mepy)₃tren]²⁺ [BAT83b]) can be used to monitor the spin transition. Pyridyl stretching bands can be found in the same region and might also show a dependence on the spin state of the metal. In the following the whole group of vibrations in this range is denominated as ' α -diimine stretching'.

An overview of the most important vibrations in comparison with the rest of the series of compounds is given at the end of the chapter.

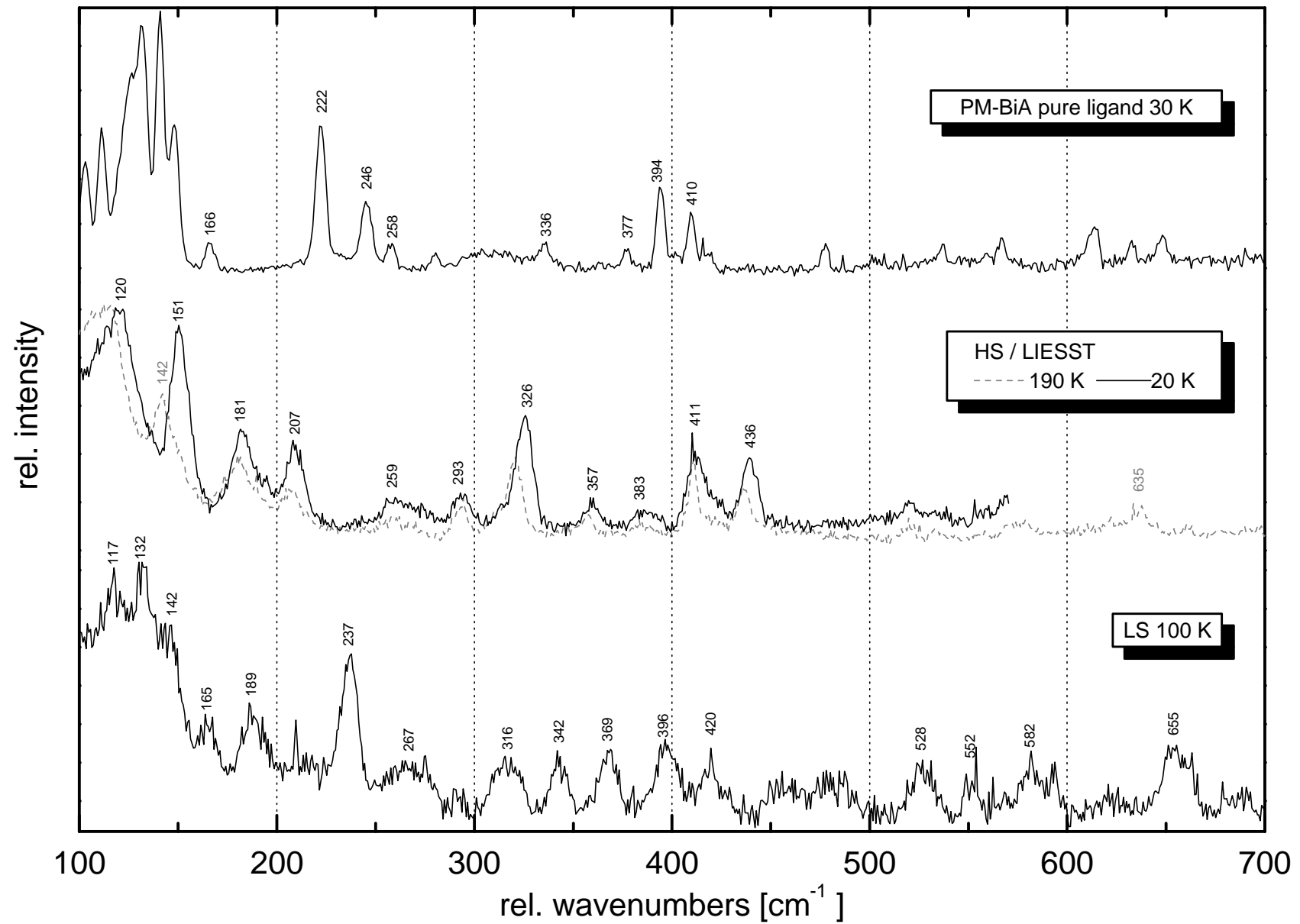


Figure 8.2: Low frequency Raman spectra of $[\text{Fe}(\text{PM-BiA})_2(\text{NCS})_2]$ and the pure ligand PM-BiA.

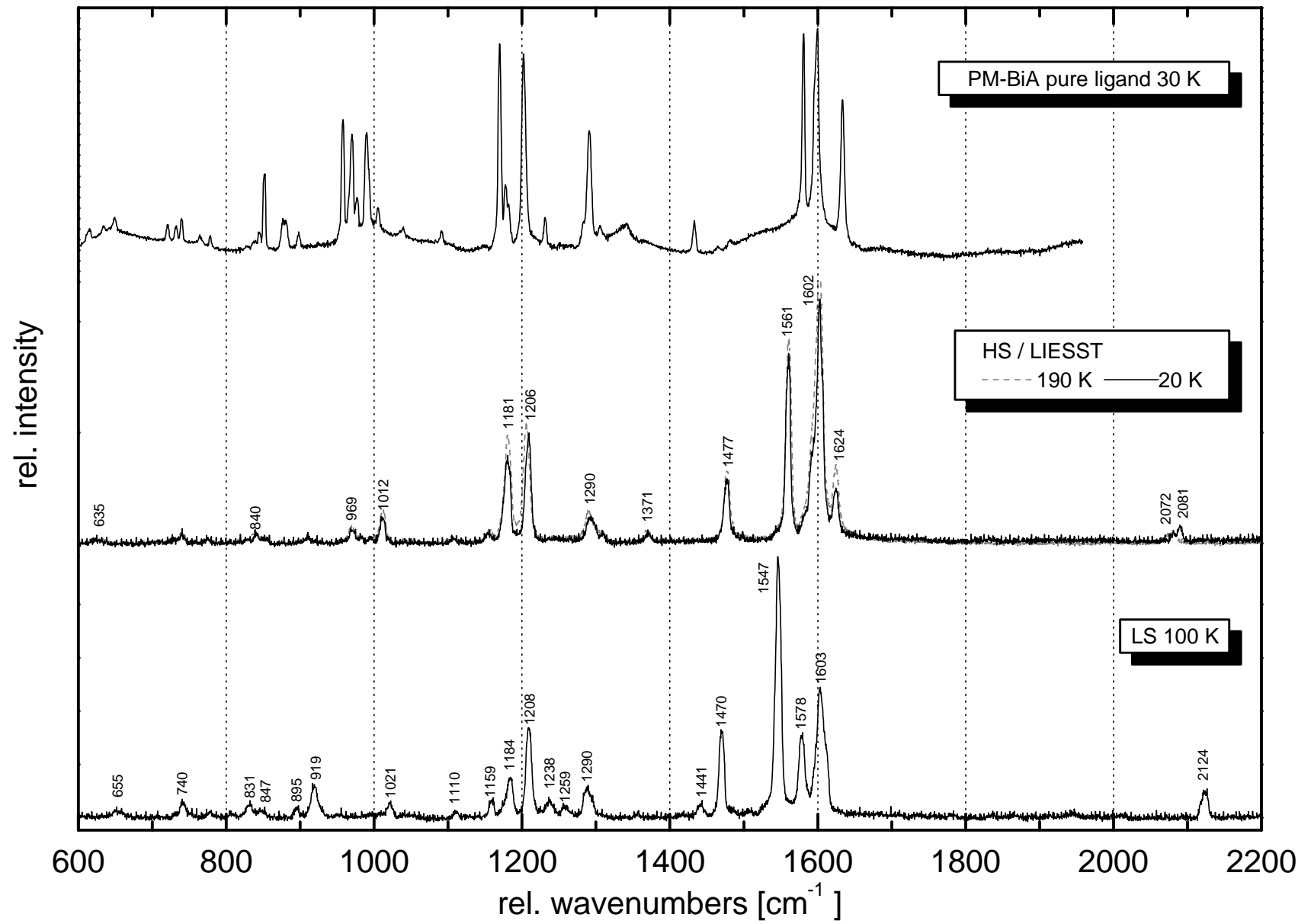


Figure 8.3: High frequency Raman spectra of $[\text{Fe}(\text{PM-BiA})_2(\text{NCS})_2]$ and the pure ligand PM-BiA.

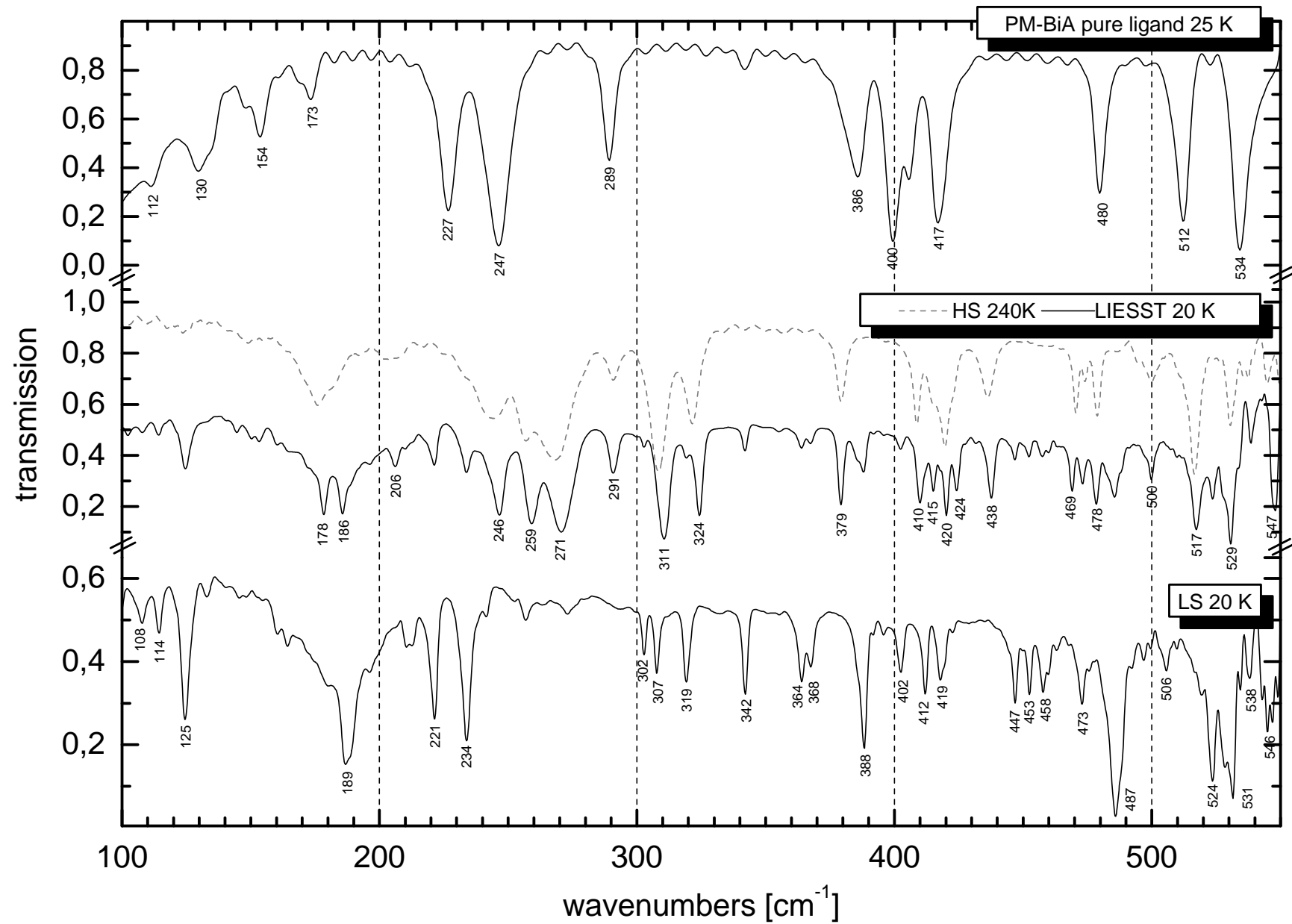


Figure 8.4: FIR spectra of $[\text{Fe}(\text{PM-BiA})_2(\text{NCS})_2]$ (nujol mulls) and the pure ligand PM-BiA (CsJ pellet).

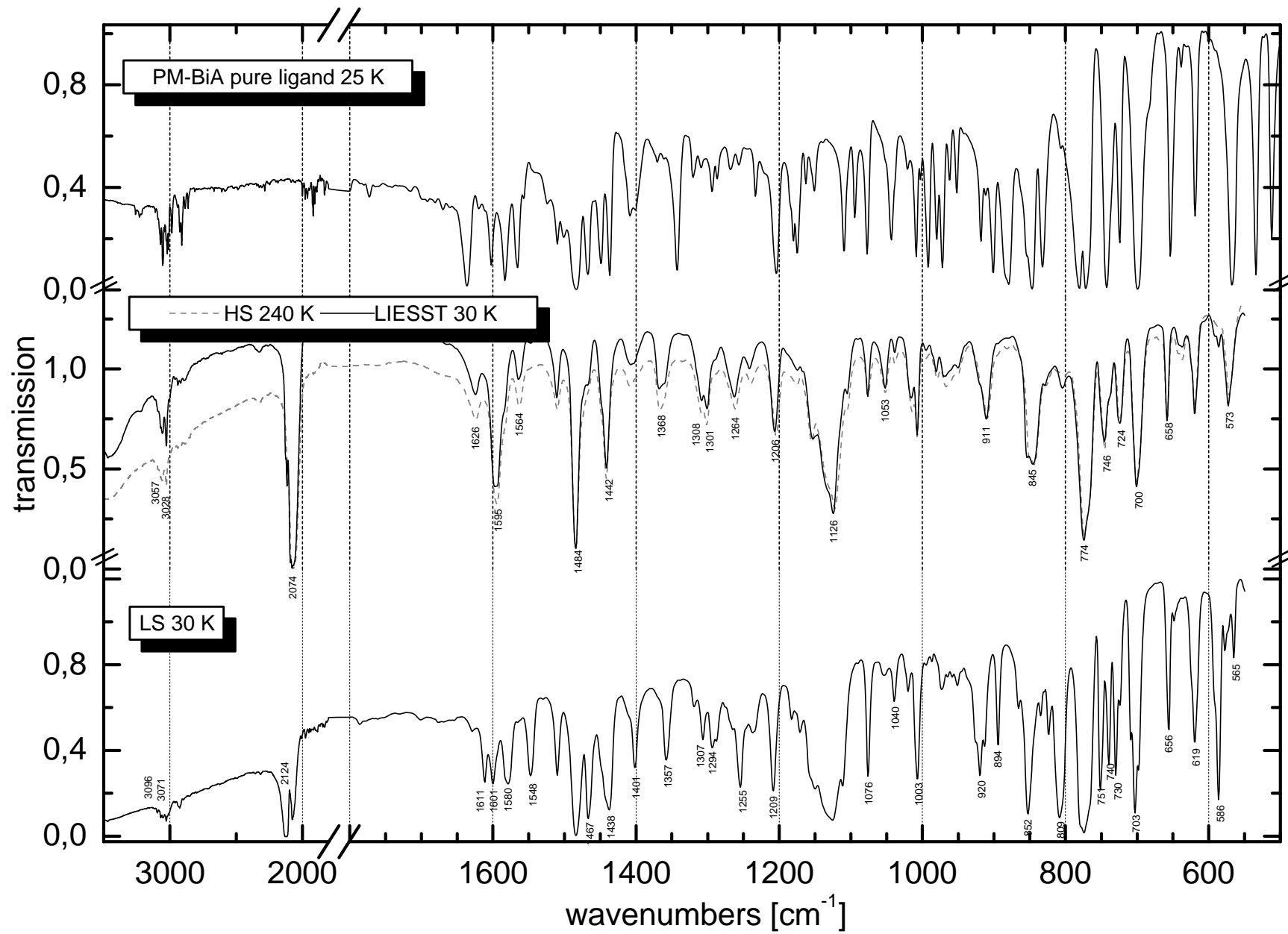


Figure 8.5: MIR spectra of $[\text{Fe}(\text{PM-BiA})_2(\text{NCS})_2]$ and the pure ligand PM-BiA (CsJ pellets).

8.2 [Fe^{II}(PM-PEA)₂(NCS)₂]

Dark green samples of [Fe^{II}(PM-PEA)₂(NCS)₂] show an abrupt and complete spin transition with a large hysteresis of 37 K ($T_{1/2}^{\downarrow} = 194$ K and $T_{1/2}^{\uparrow} = 231$ K). This is accompanied by a crystallographic phase transition between *Pccn* at 140 K and *P2₁/c* at room temperature [LET97b].

The vibrational spectra of this compound and its pure ligand PM-PEA are presented in figures 8.6 - 8.9. The 'LIESST' Raman spectra as well as the FIR spectra still contain some amount of LS. The 752 nm excitation was chosen during the Raman measurements because of a higher HS content as compared to a 514 nm excitation.

The sample treatment leads to some residual HS in the 30 K infrared spectra, which has to be considered for the comparison of the two spin states, too.

In the low energetic Raman spectra the modes at 190 and 202 cm⁻¹ might be attributed to the HS FeN₆ core, whereas the LS reveals significant modes at 210, 312 and 345 cm⁻¹. On the other hand, the two peaks at 396 and 419 cm⁻¹ in the LS spectrum might be some intra ligand modes (as visible in the FIR spectrum of the pure ligand) that are not detectable in the HS state with 752 nm excitation wavelength.

The FIR shows Fe-N modes at 254 and 265 cm⁻¹ in the HS state and 385, 393 and 405 cm⁻¹ in the LS state, respectively. NCS deformation is involved in the 470, 474, 481 and 496 cm⁻¹ modes.

In the higher energetic area again the CN-stretch of the thiocyanate as well as the α -diimine stretches are of importance. Additionally, the stretching of the C-C triple bond appears at 2221 cm⁻¹. It is split into 2224/2230 cm⁻¹ in the Raman spectrum of the LIESST state.

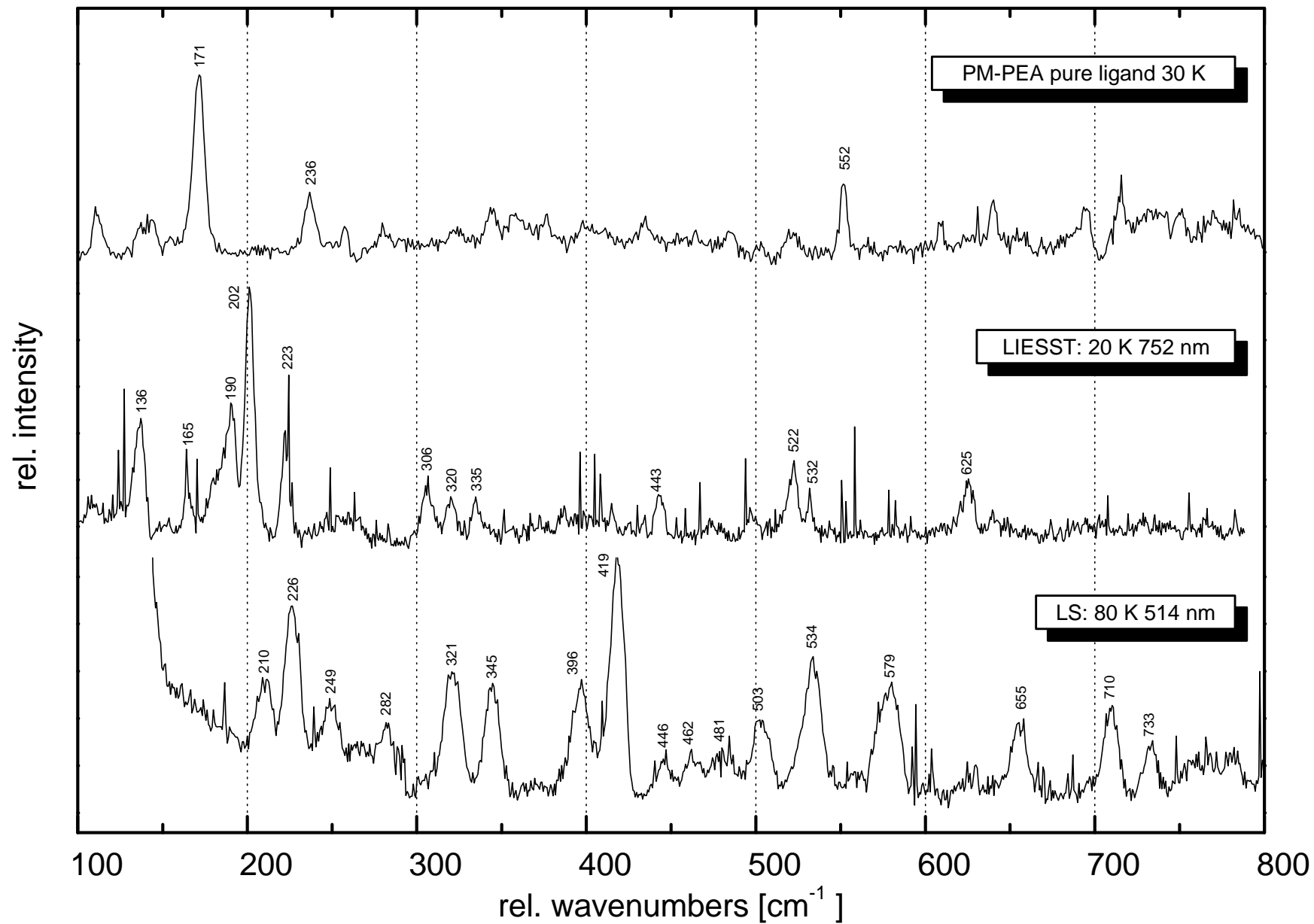


Figure 8.6: Low frequency Raman spectra of $[\text{Fe}(\text{PM-PEA})_2(\text{NCS})_2]$ and the pure ligand PM-PEA.

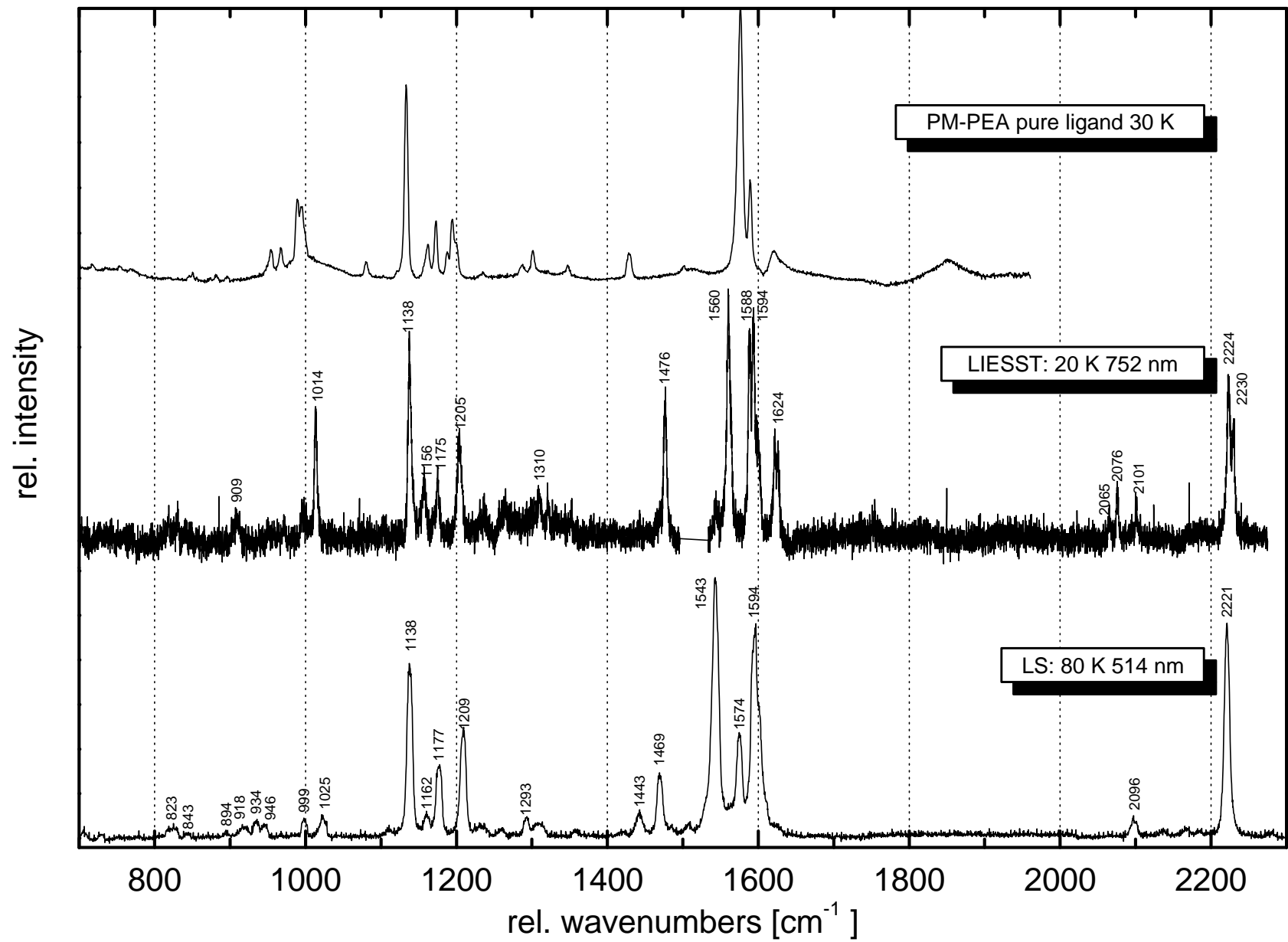


Figure 8.7: High frequency Raman spectra of $[\text{Fe}(\text{PM-PEA})_2(\text{NCS})_2]$ and the pure ligand PM-PEA.

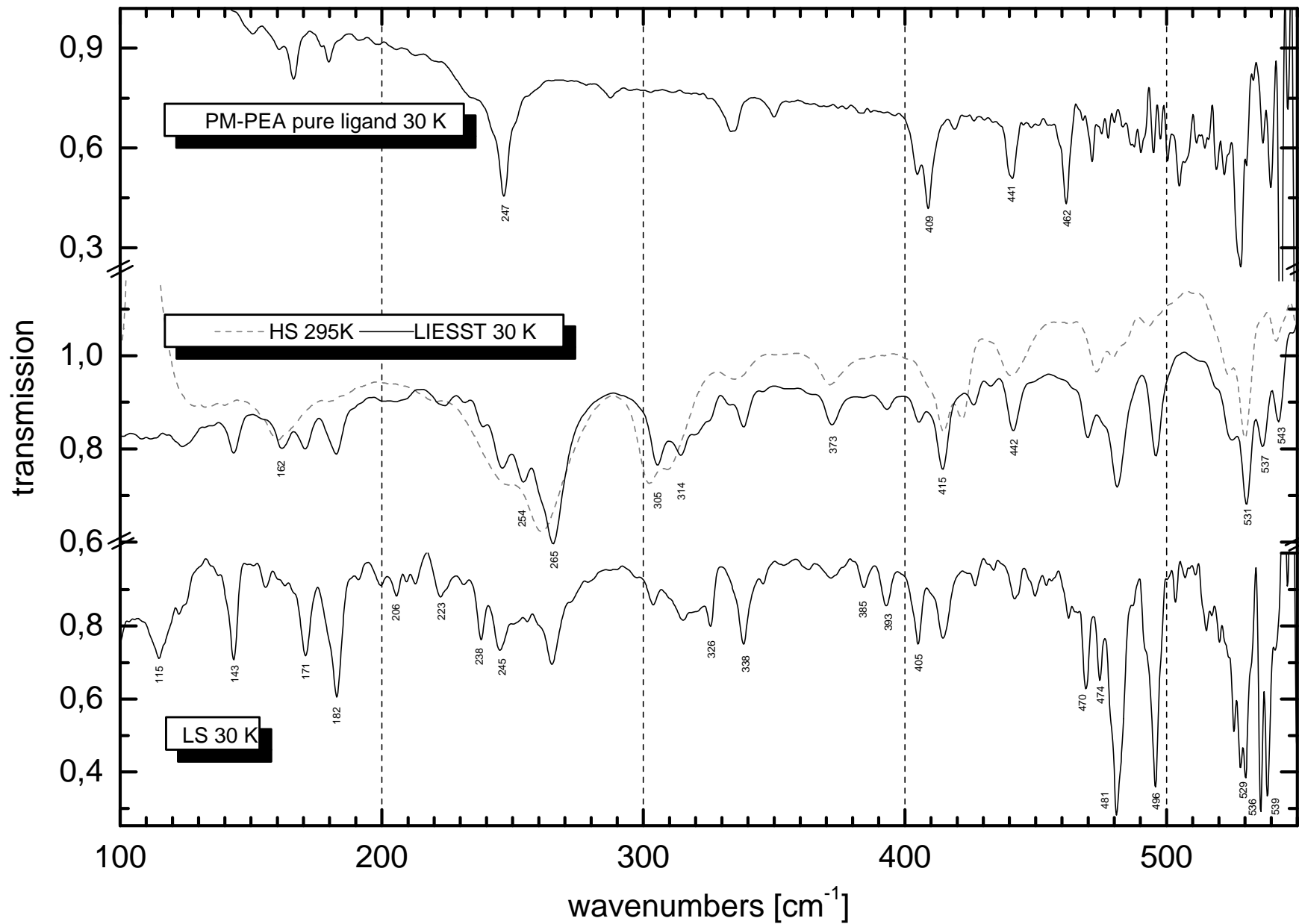


Figure 8.8: FIR spectra of $[\text{Fe}(\text{PM-PEA})_2(\text{NCS})_2]$ (nujol mulls) and the pure ligand PM-PEA (CsJ pellet).

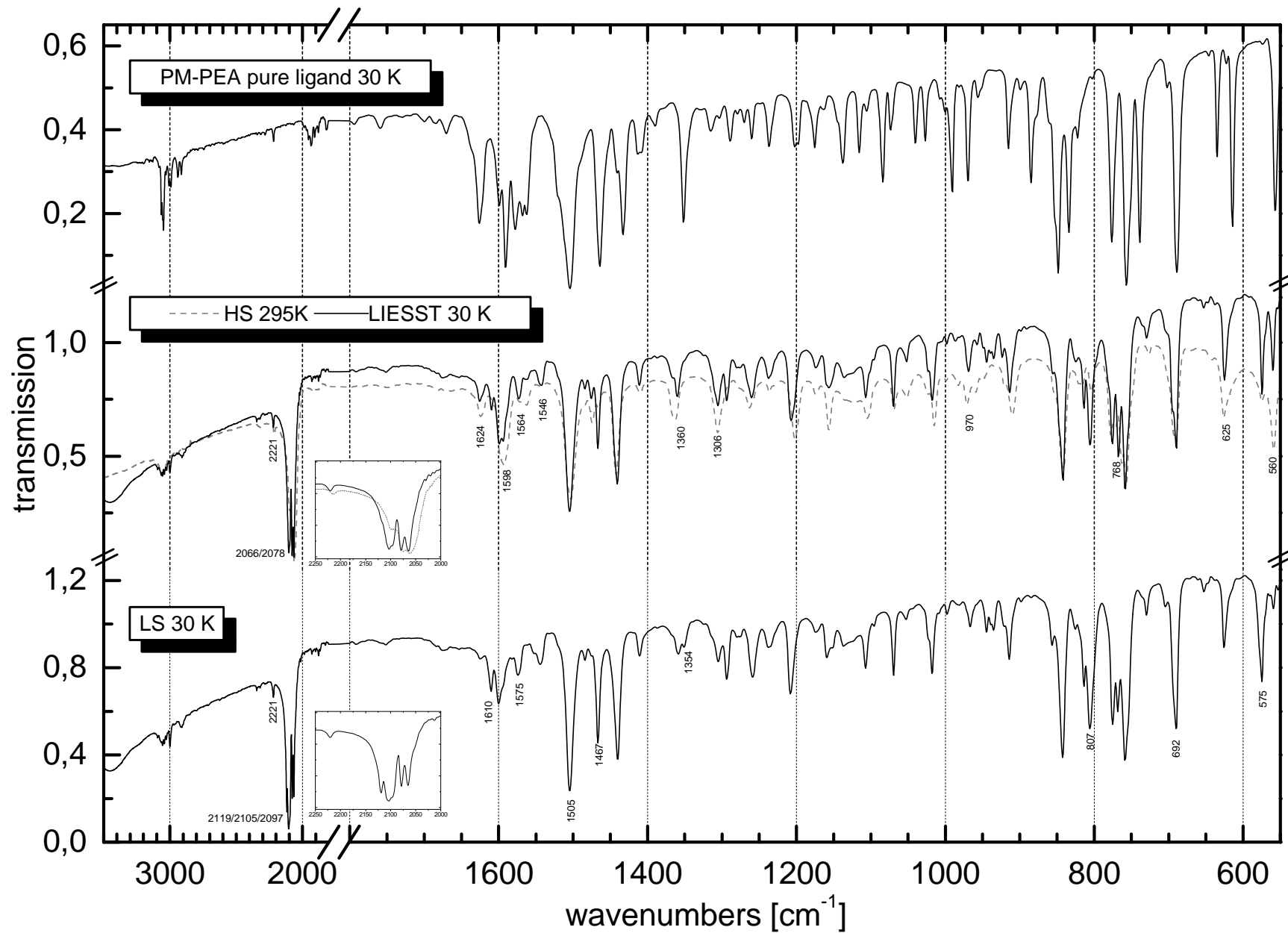


Figure 8.9: MIR spectra of $[\text{Fe}(\text{PM-PEA})_2(\text{NCS})_2]$ and the pure ligand PM-PEA (CsJ pellets).

8.3 [Fe^{II}(PM-A)₂(NCS)₂]

Samples of [Fe^{II}(PM-A)₂(NCS)₂] exhibit a gradual spin transition with an amount of residual HS about $\gamma_{\text{HS}} = 0.5$ at temperatures below 50 K [KSE98, KÖN74].

Due to the absorption in the visible region, both 514 and 752 nm excitation leads to the population of the LIESST state at 20 K as observed in the Raman spectra. Therefore, only the spectrum at 80 K using $\lambda_{\text{exc}} = 514$ nm shows a significant amount of LS species (figure 8.10). The only detectable differences between the two spin states in the higher energetic region are an additional band at 1551 cm⁻¹ in the LS state and, of course, the shift of the C-N stretch from 2075 cm⁻¹ (HS) to 2109 cm⁻¹ (LS).

In the low energetic region only a spectrum of the HS state (LIESST) at 20 K with $\lambda_{\text{exc}} = 752$ nm has been recorded in a quality good enough for revealing modes at 228, 293, 318, 523 and 552 cm⁻¹ typical for the HS species.

The FIR spectrum displayed in figure 8.11 contains some amount of LS at low temperatures as can be seen from the CN-stretch in the MIR insert. Vibrations distinctive for the HS state occur at 221, 251 and 310 cm⁻¹. The modes at 356 and 390 cm⁻¹ might be attributed to the LS state.

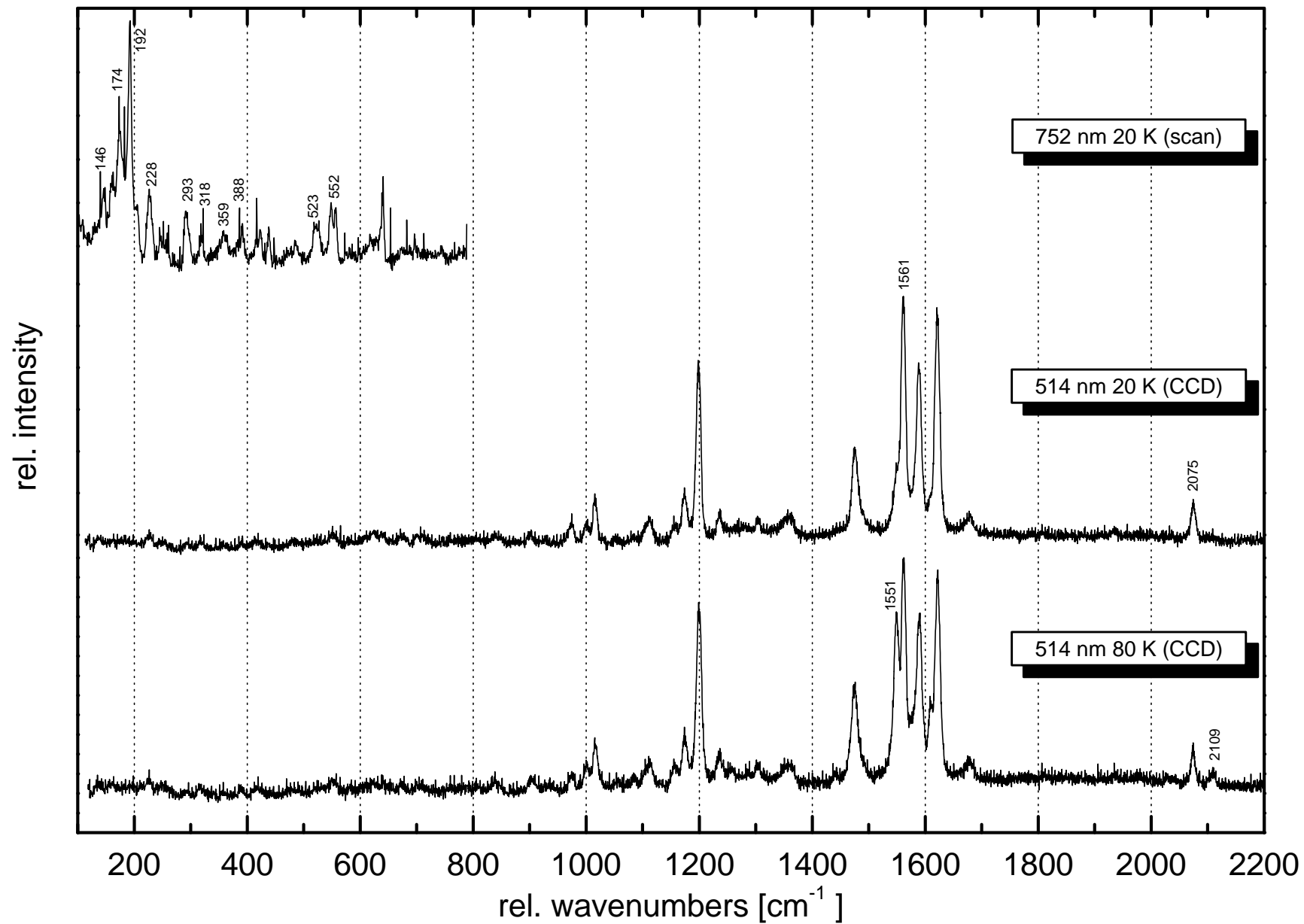


Figure 8.10: Raman spectra of [Fe(PM-A)₂(NCS)₂].

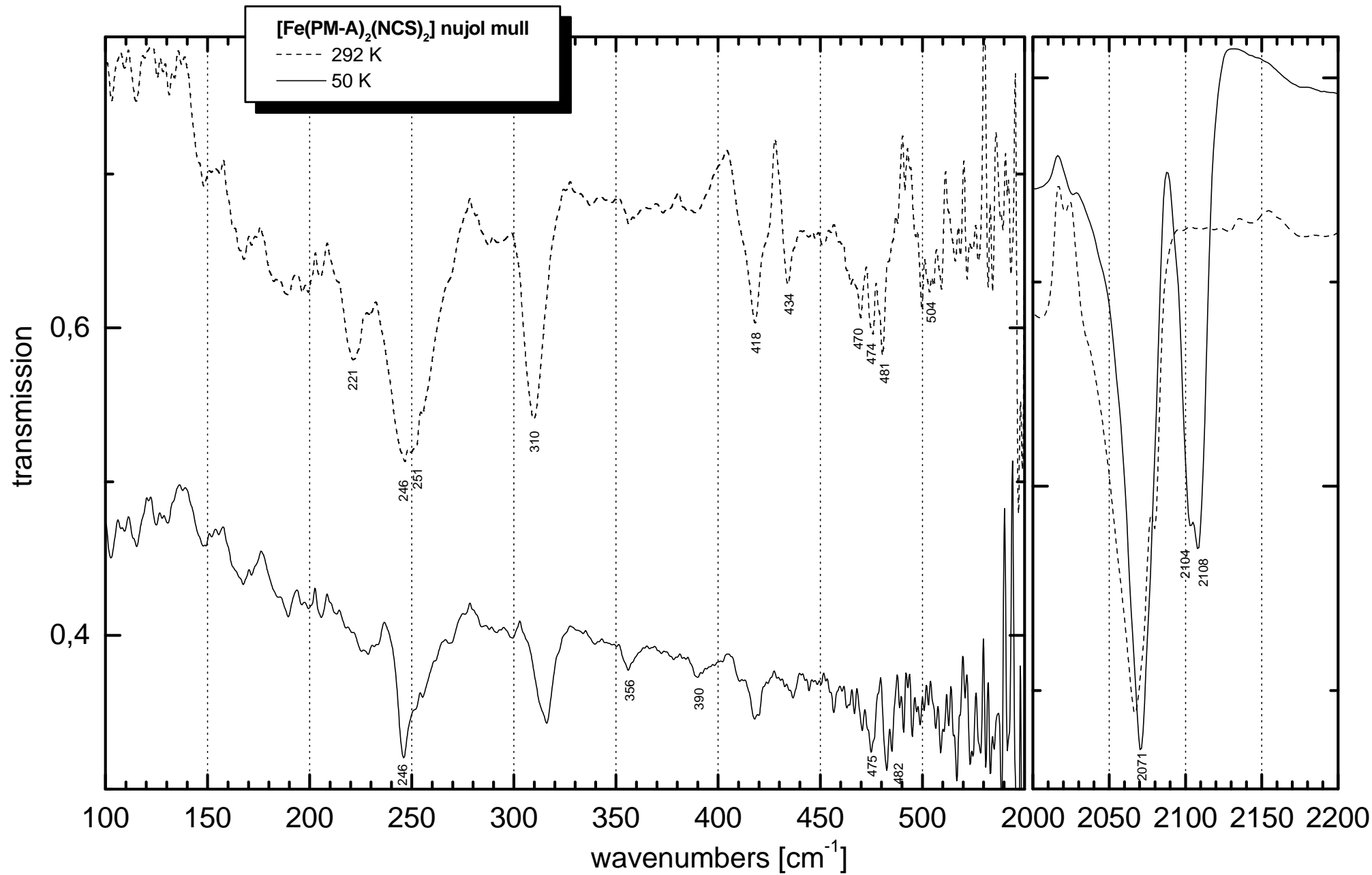


Figure 8.11: FIR spectra plus C-N-stretch region of [Fe(PM-A)₂(NCS)₂].

8.4 [Fe^{II}(PM-FIA)₂(NCS)₂]

[Fe^{II}(PM-FIA)₂(NCS)₂] undergoes a rather complete and gradual spin transition centred around $T_{1/2} = 167$ K [LET99].

The Raman spectra at 20 and 90 K as presented in figures 8.12 and 8.13 show the pure HS and LS species, respectively. Besides some small differences between HS and LS significant bands for the LIESST state occur at 161, 171, 308, 329, 500, 777, 1014, 1559, 1595, 1607 and 2075 cm⁻¹, whereas the LS reveals bands at 212, 348, 423, 473, 527, 536, 543, 784, 1025, 1546, 1573, 1622, 2118 and 2125 cm⁻¹.

The corresponding FIR spectra (figure 8.14) differ a lot between the two spin states. Having in mind the assignments made so far, the asymmetric Fe-N stretch is ascribed to the modes at 253 and 264 cm⁻¹ (HS) and 363 cm⁻¹ (LS).

The MIR spectra of the CsJ pellets (figure 8.15) show the C-N-stretch of the isothiocyanate group at 2052 / 2073 cm⁻¹ (HS) and 2122 cm⁻¹ (LS) with a large amount of residual HS at 30 K. The characteristic α -diimine-stretches are found at 1561, 1592 and 1626 cm⁻¹ (HS) and 1543, 1581, 1605 and 1619 cm⁻¹ (LS), respectively.

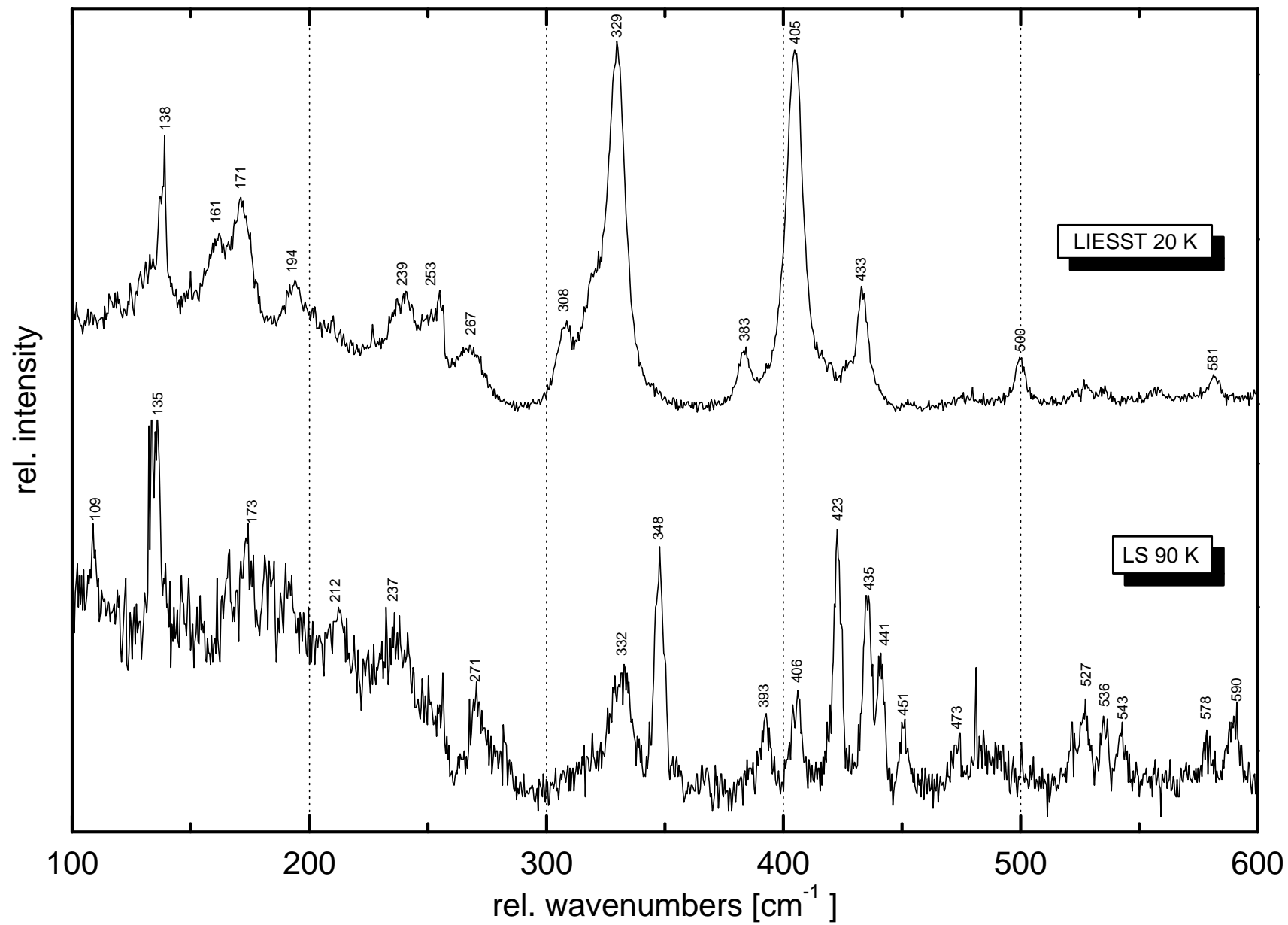


Figure 8.12: Low frequency Raman spectra of $[\text{Fe}(\text{PM-FIA})_2(\text{NCS})_2]$.

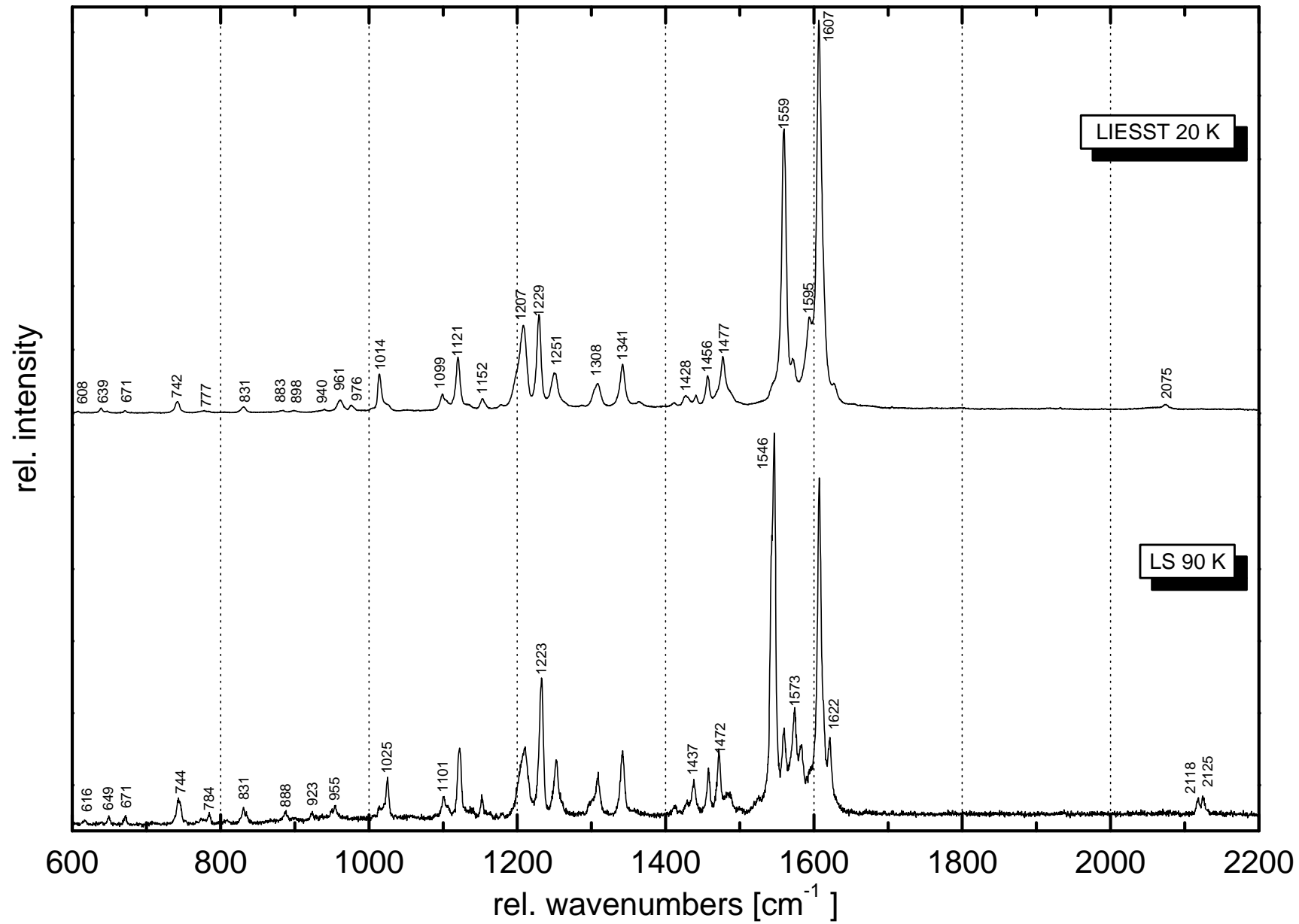


Figure 8.13: High frequency Raman spectra of $[\text{Fe}(\text{PM-FIA})_2(\text{NCS})_2]$.

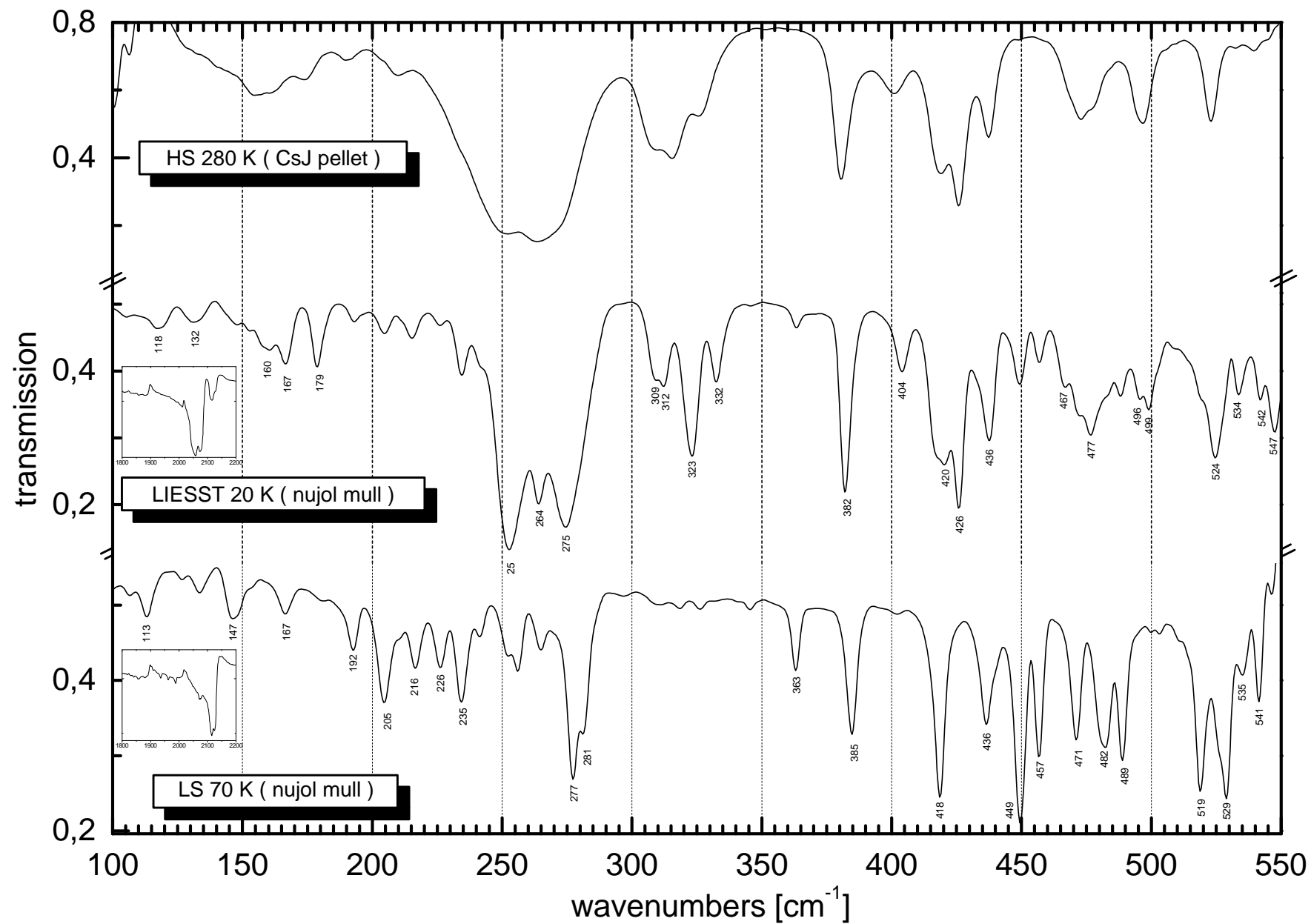


Figure 8.14: FIR spectra of $[\text{Fe}(\text{PM-FIA})_2(\text{NCS})_2]$.

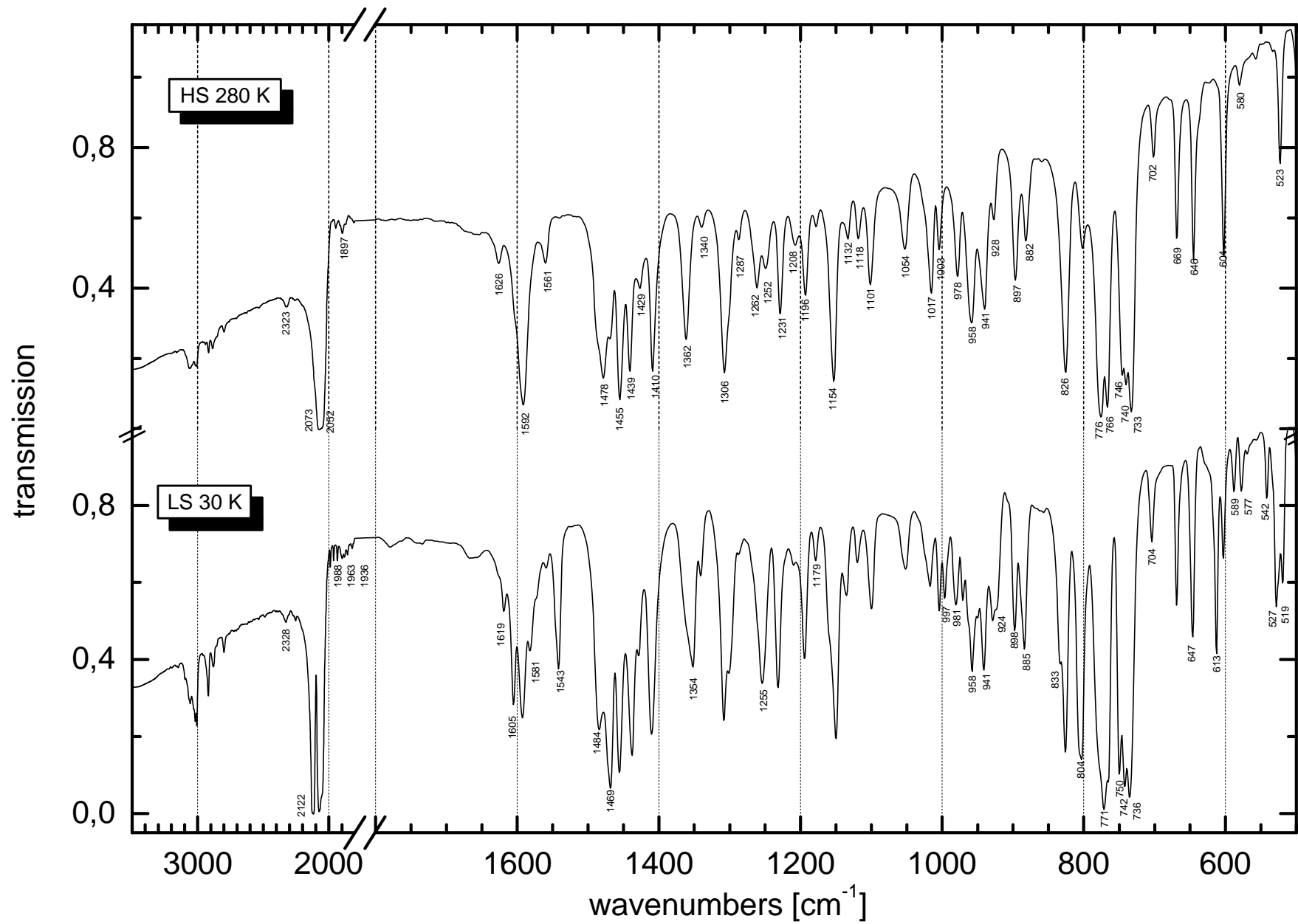


Figure 8.15: MIR spectra of $[\text{Fe}(\text{PM-FlA})_2(\text{NCS})_2]$ (CsJ pellets).

8.5 [Fe^{II}(PM-DMA)₂(NCS)₂]

Samples of the grey powder of [Fe^{II}(PM-DMA)₂(NCS)₂] do not exhibit a thermal spin cross-over but stay in the HS state from 300 to 10 K [KSE98].

Figures 8.16 and 8.17 show the comparison of the Raman and IR spectra at low temperatures in the low and high frequency range, respectively.

In agreement with the assignments made so far in this series of compounds, the vibrations at 134, 164 and 181 cm⁻¹ (Raman) and 242, 249 and 262 cm⁻¹ (FIR) are ascribed to have mainly Fe^{HS}-N stretching character. Furthermore, the NCS-bend at 481/490 cm⁻¹, the CS-stretch at 809/811 cm⁻¹, the α -diimine-stretches at 1569, 1589/1495 and 1634/1638 cm⁻¹, and finally the CN-stretch at 2066/2071 cm⁻¹ are assigned.

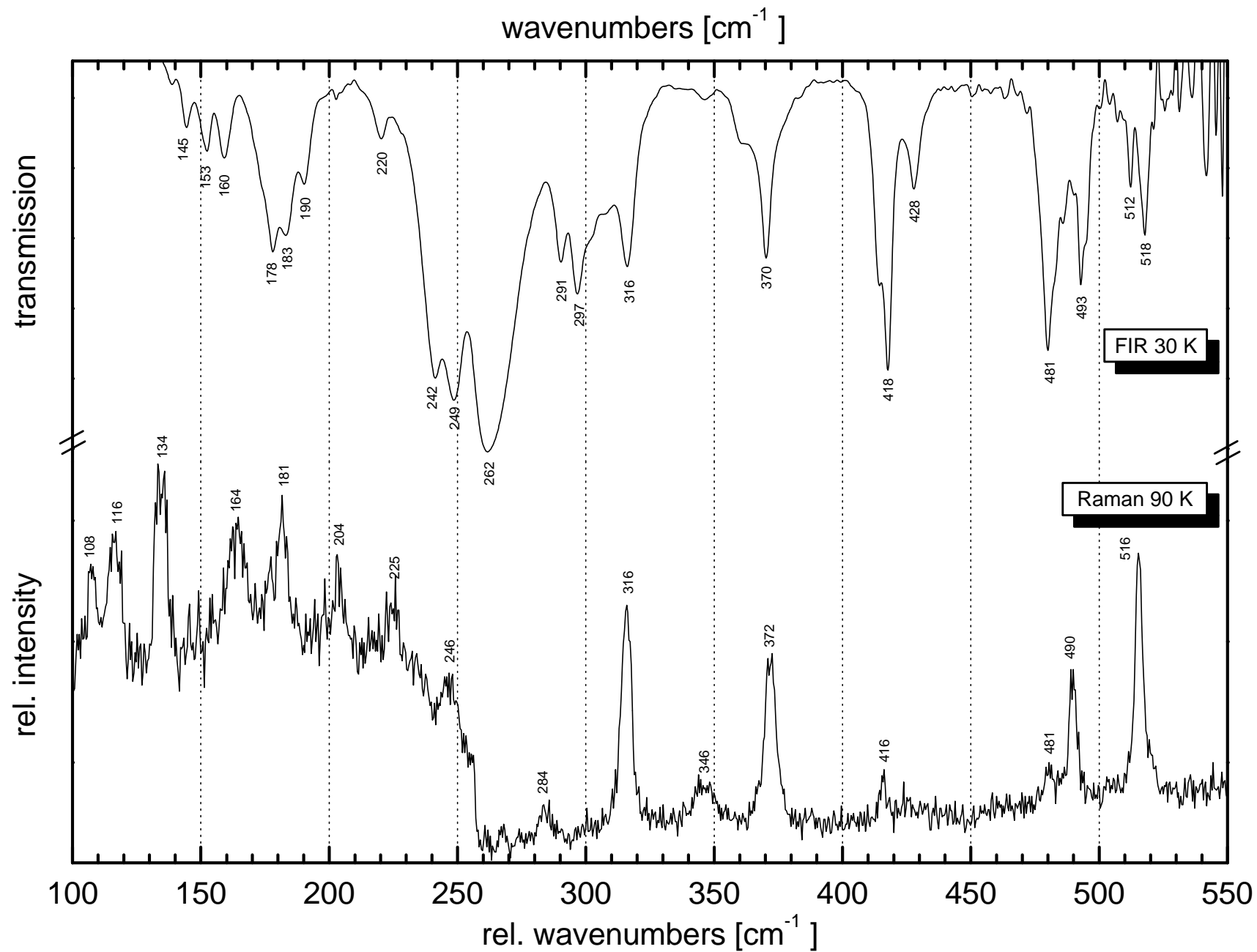


Figure 8.16: Low frequency Raman and FIR spectra (CsJ pellet) of $[\text{Fe}(\text{PM-DMA})_2(\text{NCS})_2]$.

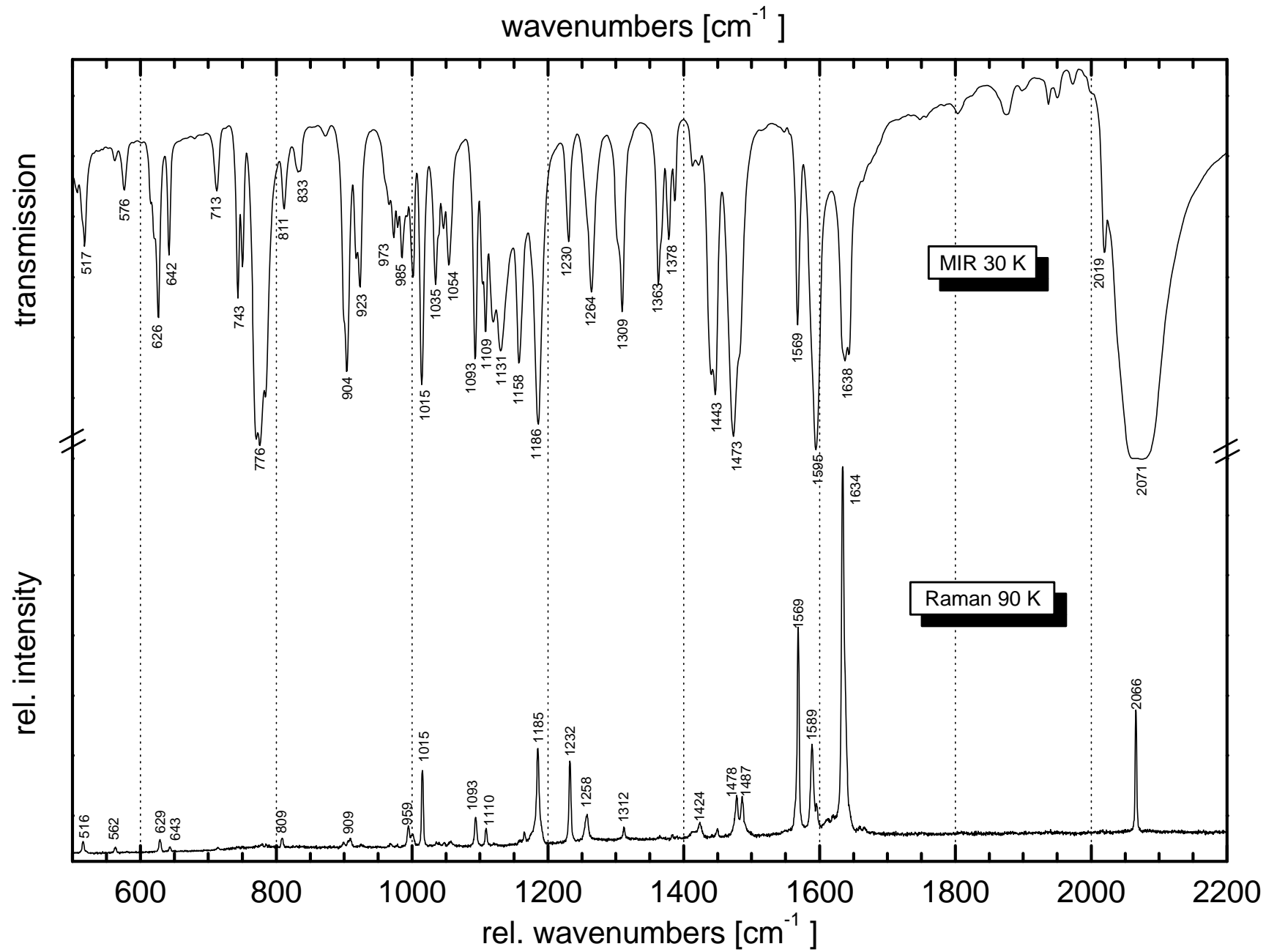


Figure 8.17: High frequency Raman and MIR spectra (CsJ pellet) of $[\text{Fe}(\text{PM-DMA})_2(\text{NCS})_2]$.

8.6 [Fe^{II}(PM-AzA)₂(NCS)₂]

The dark green compound [Fe^{II}(PM-AzA)₂(NCS)₂] shows a complete spin crossover with transition temperatures of $T_{1/2}^{\downarrow} = 186$ K and $T_{1/2}^{\uparrow} = 192$ K [KSE98].

Figures 8.18 and 8.19 depict the FIR and MIR spectra of the two spin states in comparison with the spectra of the pure ligand PM-AzA.

The nujol mull employed for the low energetic region is free of residual HS content at 70 K, but the LIESST conversion at 20 K is not complete. The Fe-N modes can be found at 255 and 268 cm⁻¹ in the LIESST state and at 345, 357 and 382/391 cm⁻¹ for the LS case. The modes between 467 and 480 cm⁻¹ are attributed to the bending of the isothiocyanate group.

The CsJ pellet used for the MIR spectra even at 30 K contains some amount of residual HS. Besides the shift of the CN-stretch from 2070/2082 cm⁻¹ in the HS to 2110/2122 cm⁻¹ in the LS state, the main difference between the two spin states again occurs in the α -diimine stretching region: the HS modes at 1562, 1590 and 1623 cm⁻¹ move to 1558, 1580 and 1610 cm⁻¹ in the LS state.

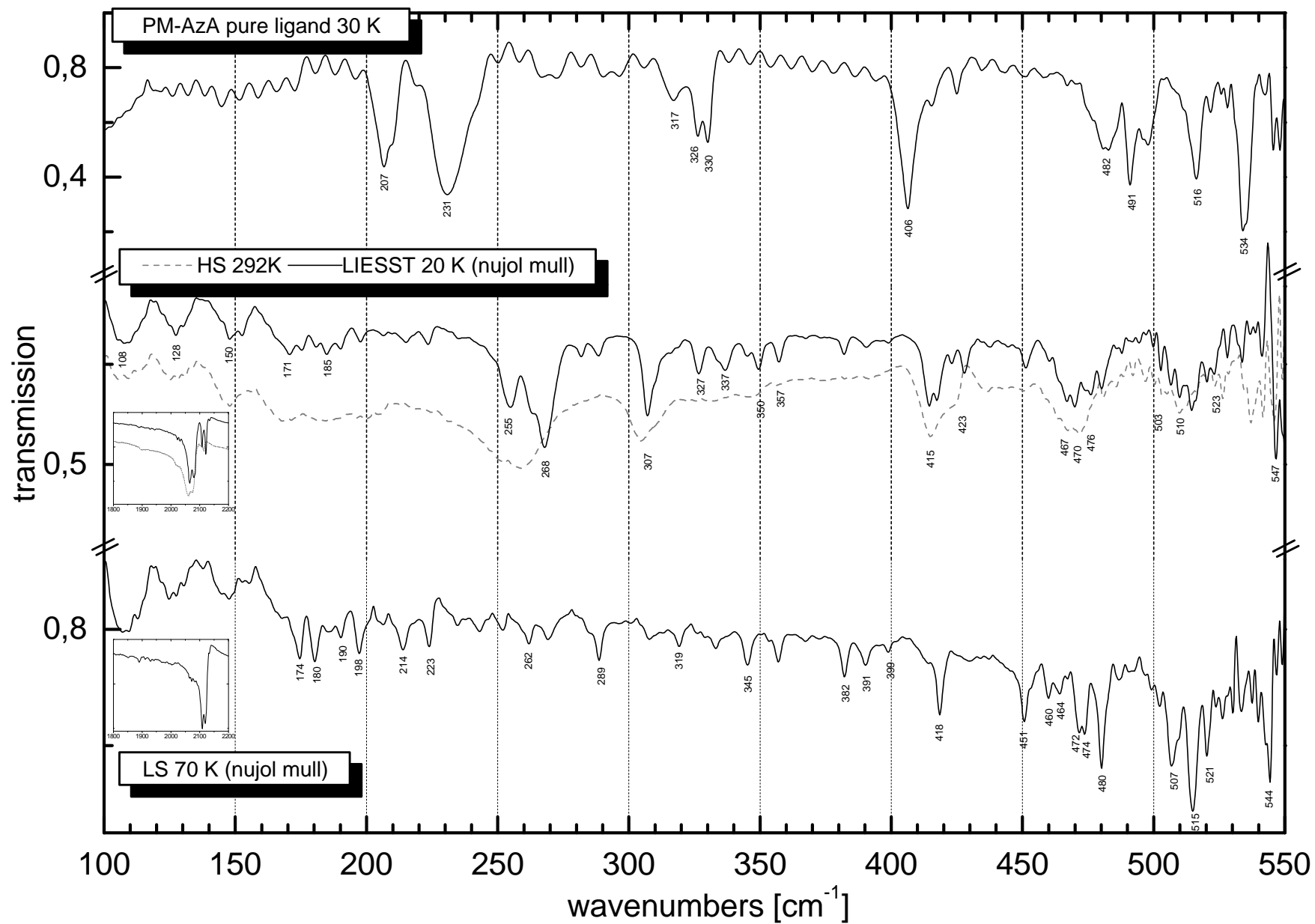


Figure 8.18: FIR spectra (nujol mull) of $[\text{Fe}(\text{PM-AzA})_2(\text{NCS})_2]$ and the pure ligand PM-AzA.

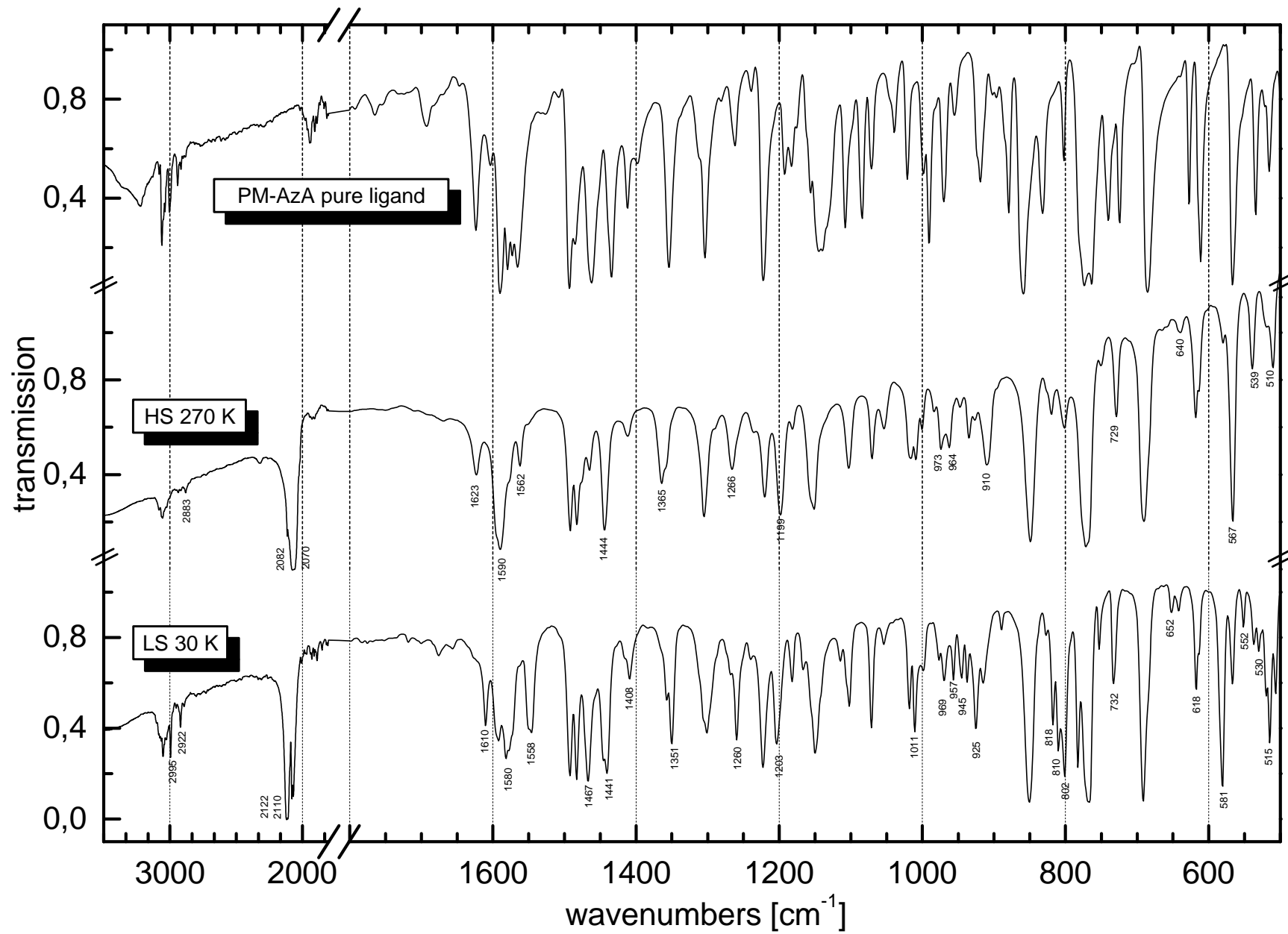


Figure 8.19: MIR spectra (CsJ pellets) of $[\text{Fe}(\text{PM-AzA})_2(\text{NCS})_2]$ and the pure ligand PM-AzA.

8.7 [Fe^{II}(PM-BPM)₂(NCS)₂]

Violet samples of [Fe^{II}(PM-BPM)₂(NCS)₂] exhibit spin crossover [LET98b].

Figures 8.20 and 8.21 show the low- and high-frequency infrared spectra of a nujol mull and a CsJ pellet at 295 and 70 K, respectively. After both kinds of sample treatment the spectrum at 70 K contains predominantly LS species.

The vibrations at 222 and 244 cm⁻¹ in the HS state as well as the modes at 369 and 394 cm⁻¹ in the LS state arise from Fe-N movements.

In the 500-700 cm⁻¹ region quite a few changes occur that are attributed to in-plane bends of the diimine ligand. Peaks in the α -diimine stretching regime shift from 1566, 1596 and 1637 cm⁻¹ in the HS to 1554, 1599 and 1611 cm⁻¹ in the LS state. Lastly, the CN-stretch is at 2062/2074 cm⁻¹ at ambient temperature and at 2104/2115 cm⁻¹ at 70 K.

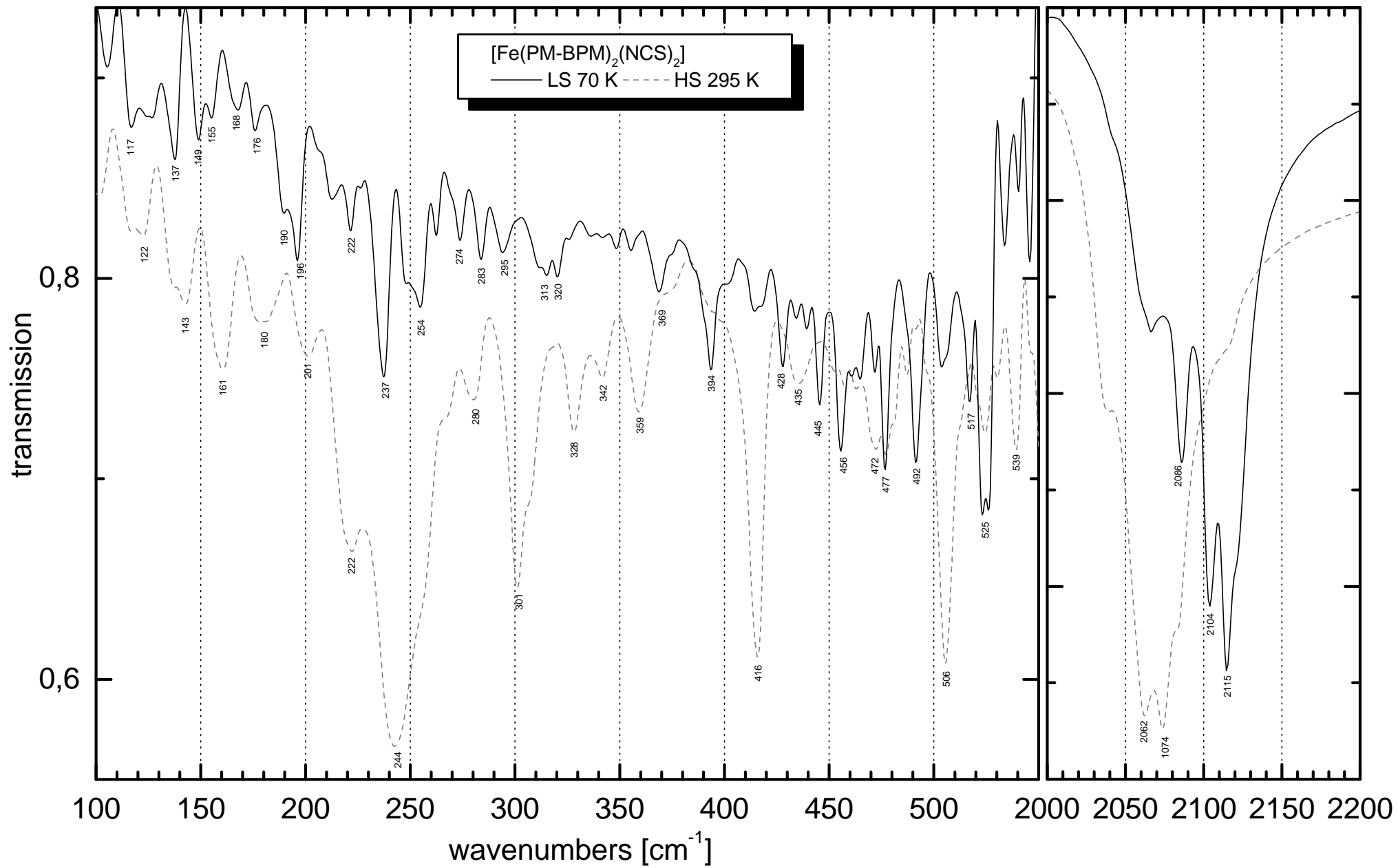


Figure 8.20: FIR spectra (nujol mulls) of $[\text{Fe}(\text{PM-BPM})_2(\text{NCS})_2]$.

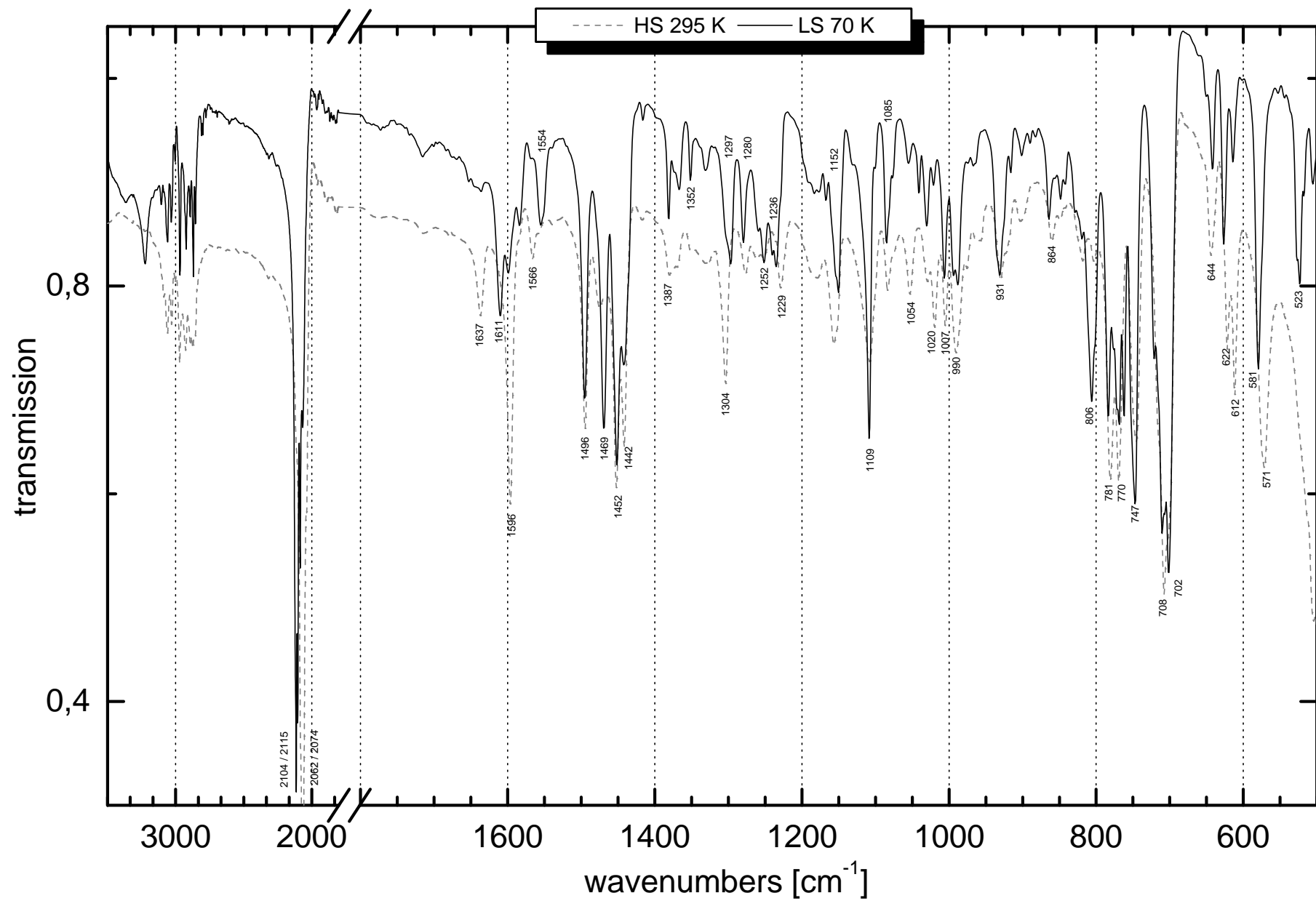


Figure 8.21: MIR spectra (CsJ pellets) of $[\text{Fe}(\text{PM-BPM})_2(\text{NCS})_2]$.

8.8 [Fe^{II}(PM-BMM)₂(NCS)₂]

Black powder samples of [Fe^{II}(PM-BMM)₂(NCS)₂] exhibit spin crossover [LET98b].

Figures 8.22 and 8.23 depict the FIR spectra of a nujol mull at 260 and 20 K and the MIR spectrum of a CsJ pellet at 20 K, respectively. The 20 K spectra are merely low-spin. It was not possible to populate the LIESST state at 20 K with 514 nm irradiation in neither of both matrices.

Fe^{HS}-N stretching is assigned to 242 cm⁻¹, whereas the corresponding LS mode occurs at 364/380 cm⁻¹.

The low-spin species reveals the α -diimine stretching at 1554, 1590 and 1610 cm⁻¹ and the CN stretch at 2114/2126 cm⁻¹.

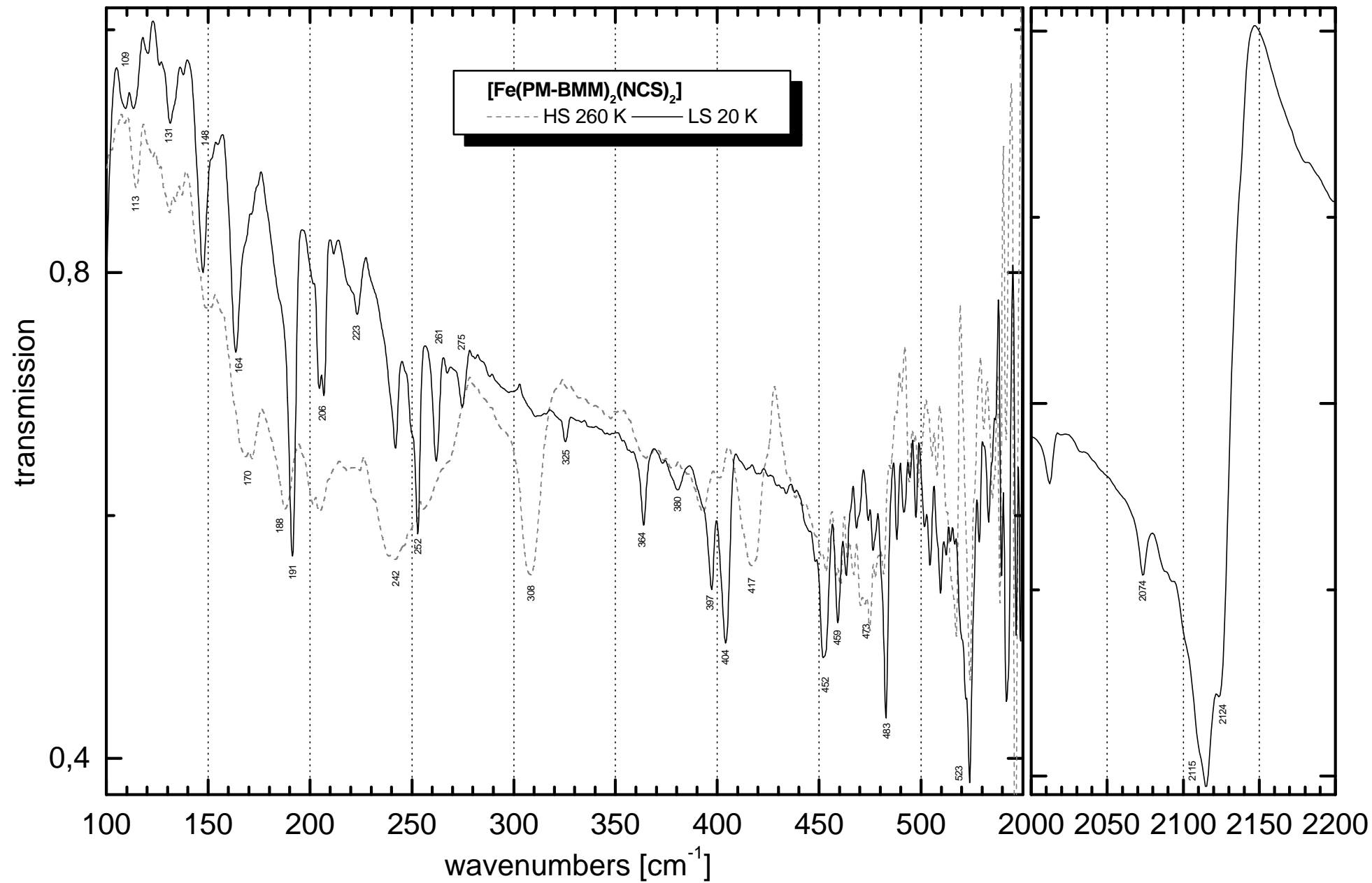


Figure 8.22: FIR spectra (nujol mulls) of [Fe(PM-BMM)₂(NCS)₂].

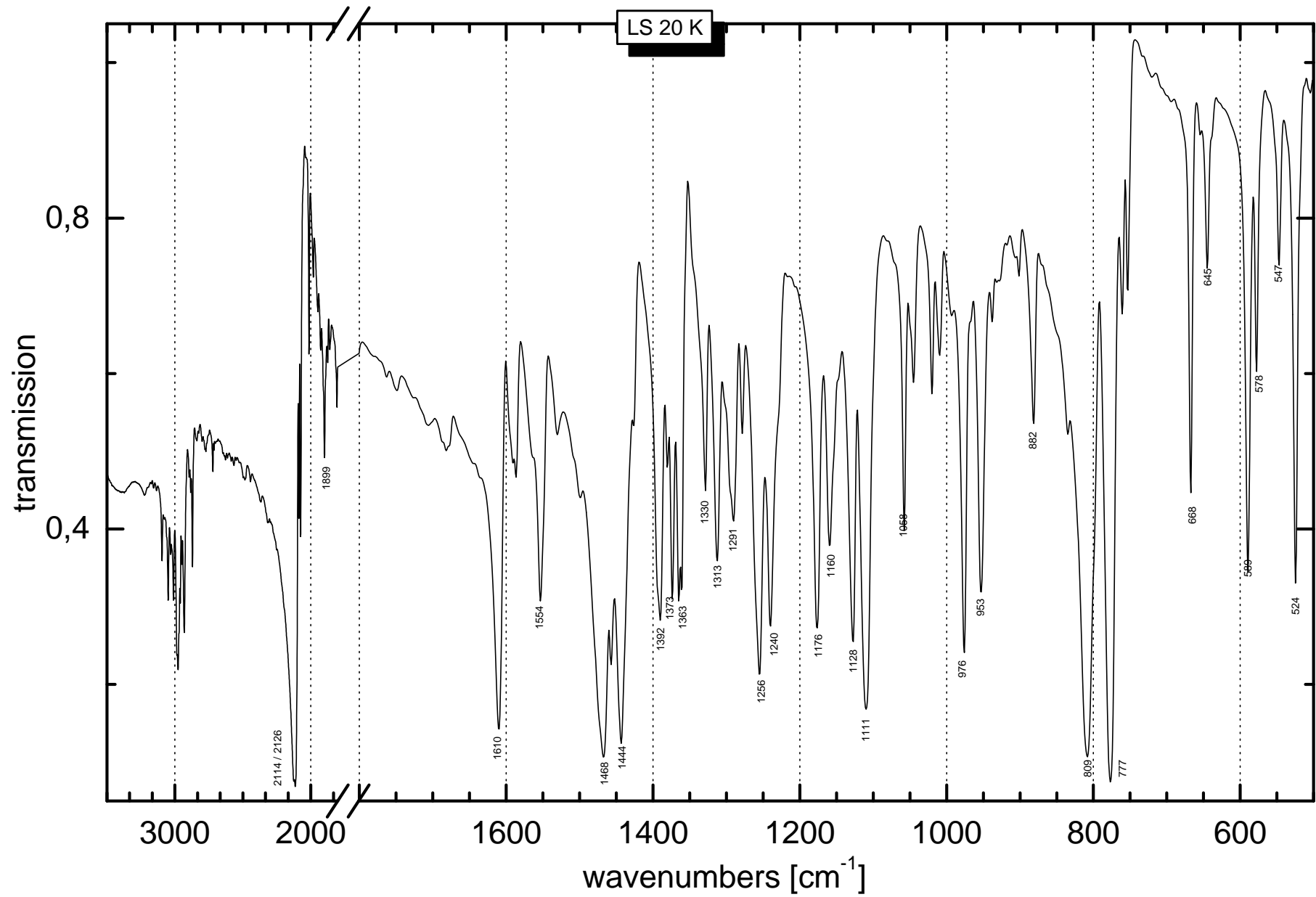


Figure 8.23: MIR spectrum (CsJ pellet) of $[\text{Fe}(\text{PM-BMM})_2(\text{NCS})_2]$ at 20 K.

8.9 Comparison and summary

In this chapter a series of complexes with very similar ligands PM-R which only vary in the substituent R have been investigated by vibrational spectroscopy. Depending on the substituent R they show different spin state behaviour over the temperature range from 10 to 300 K. Based on the similarity of the environment around the metal ion along this series, the calculations on a simplified model presented in chapter 7 and the resemblance to the already much more investigated $[\text{Fe}(\text{phen})_2(\text{NCS})_2]$ treated in chapter 6, some of the most important vibrations influenced by the spin crossover could be assigned. These assignments are summarised in table 8.1. In general the asymmetric Fe-N stretch appears at 220 - 270 cm^{-1} (HS) and 340 - 400 cm^{-1} (LS) in the far infrared. The assignment of the symmetric modes in the Raman spectra is not that unequivocal. But they should be around 130 - 200 cm^{-1} (HS) and 200 - 250 cm^{-1} (LS). The bend of the thiocyanate group centred around 470 cm^{-1} shows only slight dependence on the spin state, like the C-S stretch found around 800 cm^{-1} . As already known from quite a lot of spin crossover compounds with cis-NCS ligands a shift of the C-N stretch from $\sim 2070 \text{ cm}^{-1}$ (HS) to $\sim 2120 \text{ cm}^{-1}$ (LS) is observed.

Additionally, several intra-ligand modes of the α -diimine ligand are influenced by the spin transition due to the movement of the coordinating atom. These modes may occur in a wide range of vibrational energy, e.g. in the 450 - 700 cm^{-1} region or around 1000 cm^{-1} as discussed on the calculations in chapter 7. Finally, the α -diimine stretches around 1600 cm^{-1} change significantly when going from high-spin to low-spin state.

R =	mode	Infrared		Raman	
		HS	LS	HS	LS
BiA	Fe-N	246,259,271	342,364,368	151,207,326	237
	δ (NCS)	438,469,478	447,453,458, 473,487		
	C-S		809	840	831, 847
	C-N	2074	2124	2072, 2081	2124
	α -diimine-stretch	1564,1595,1626	1548,1580, 1601,1611	1561,1602, 1624	1547,1578, 1603
PEA	Fe-N	254, 265	385,393,405	190, 202	210,321,345
	δ (NCS)	(474, 481)	470,474, 481,496		446,462, 481
	C-S		807		823
	C-N	2066, 2078	2097,2105, 2119	2065, 2076	2096
	α -diimine-stretch	1564,1598,1624	1546,1575, 1600,1611	1560,1588, 1594,1624	1543,1574, 1594
FIA	Fe-N	253, 264	363	161, 171	212, 348
	δ (NCS)	467, 477	471,482,489		473
	C-S		804	777	784
	C-N	2052, 2073	2122	2075	2118, 2125
	α -diimine-stretch	1561,1592,1626	1543,1581, 1605,1619	1559,1595,1607	1546,1573, 1622
A	Fe-N	221,246,251	356, 390	146,174,192	
	δ (NCS)	470,474,481	475, 482		
	C-S				
	C-N	2071	2104, 2108	2075	2109
	α -diimine-stretch			1561,1589,1623	1551, 1614
DMA	Fe-N	242,249,262		134,164,181	
	δ (NCS)	481, 493		481, 490	
	C-S	811		809	
	C-N	2071		2066	
	α -diimine-stretch	1569,1595,1638		1569,1589,1634	
AzA	Fe-N	255, 268	345,357,382/91		
	δ (NCS)	467,470,476	472,474,480		
	C-S		802,810,818		
	C-N	2070, 2082	2110, 2122		
	α -diimine-stretch	1562,1590,1623	1558,1580,1610		
BPM	Fe-N	222, 244	369, 394		
	δ (NCS)	472	472,477,492		
	C-S		806		
	C-N	2062,2074,2086	2086, 2104,2115		
	α -diimine-stretch	1566,1596,1637	1554,1599,1611		
BMM	Fe-N	242	364, 380		
	δ (NCS)	473	483		
	C-S		809		
	C-N	2074	2114, 2126		
	α -diimine-stretch		1554, 1590, 1610		

Table 8.1: Comparison of the assigned vibrations [cm^{-1}] in the series of compounds $[\text{Fe}(\text{PM-R})_2(\text{NCS})_2]$.

9 Summary

The spin crossover phenomenon has been studied for many years by different research groups. Especially, there is great interest in explaining the mechanism of cooperative interactions, which govern the spin transition in the solid state. In order to investigate these cooperative interactions, the internal degrees of freedom of the molecular units must be known. In particular the contribution of the molecular vibrations to the entropy difference between the two spin states, which is to a large extent the driving force of the spin crossover, is an important factor, which is hardly known in detail.

In this context the vibrational properties of several spin crossover compounds have been studied extensively within the scope of this thesis. In general, temperature dependent Raman, middle and far infrared spectroscopy, isotope substitution and normal coordinate analysis in conjunction with density functional theory have been employed.

The $[M(\text{ptz})_6](\text{BF}_4)_2$ ($M = \text{Fe}, \text{Zn}$) system is one of the most extensively investigated systems in spin crossover research. This work yields the assignment of important frequencies and the relation of the force constants in both spin states:

The infrared-active ' T_{1u} ' metal-ligand stretching vibrations were assigned unequivocally by the help of isotope substitution with the metals ^{54}Fe , ^{56}Fe , ^{64}Zn , and ^{68}Zn . They occur at 191 cm^{-1} (Zn), 232 cm^{-1} (LIESST) and $359/413 \text{ cm}^{-1}$ (LS), respectively. The splitting of this mode in the LS state was explained by a coupling with an intra-ligand mode shown by NCA and DFT calculations. The similar complex $[\text{Fe}(\text{mtz})_6](\text{BF}_4)_2$ reveals the corresponding modes at $223/236 \text{ cm}^{-1}$ (LIESST) and $356/423/426 \text{ cm}^{-1}$ (LS).

DFT calculations on a simplified model result in a factor of 2.1 in the metal-ligand bond force constants between LS and HS. Further refinement of these values by adjusting to the assigned experimental frequencies in the framework of normal coordinate analysis lead to approximate force constants of $0.8 \text{ mdyn}/\text{\AA}$ (HS) and $1.95 \text{ mdyn}/\text{\AA}$ (LS) i.e. a factor of 2.4.

These calculations suggest the totally symmetric A_{1g} stretching mode, which is thought to be the reaction coordinate along the thermal spin crossover, to shift from 131 cm^{-1} (HS) to 201 cm^{-1} (LS). Probably, this mode has to be attributed to the experimental values at 141 cm^{-1} (HS) and 236 cm^{-1} (LS) in the former Raman measurements [HOE95].

The $[M(\text{ptz})_6](\text{BF}_4)_2$ system has only van-der-Waals forces between the molecules in the solid state. The covalent two-dimensional spin crossover system $\alpha\text{-}\{M[(\text{entz})_3\text{N}]_2\}(\text{BF}_4)_2$, which has very similar molecular units, reveals only slightly different frequencies: the analogue modes are tentatively assigned to 160 cm^{-1} (Zn), 167 cm^{-1} (HS) and $261/279 \text{ cm}^{-1}$ (LS) for the A_{1g} stretch observed by Raman spectroscopy and 236 cm^{-1} (HS) and $369/386/412/425 \text{ cm}^{-1}$ (LS) for the infrared active T_{1u} motion.

In the course of these investigations light induced structural phase transitions have been observed and monitored by vibrational spectroscopy. The HS-LIESST state has been shown

to exist in two different lattices at low temperatures accessible by the choice of temperature and laser power.

There has been a discrepancy between the vibrational contribution to the entropy difference of the two spin states derived from the FIR literature data assignments of $[\text{Fe}(\text{phen})_2(\text{NCS})_2]$ from 1972 [TAK72, TAK73, TAK74] and the actual measured values of the entropy difference. With the help of Resonance Raman, FIR and MIR spectroscopy, isotope substitution ($^{15}\text{N}^{13}\text{CS}$) and DFT calculations on a simplified model it was possible to reassign the asymmetric stretch of $[\text{Fe}(\text{phen})_2(\text{NCS})_2]$ in partial disagreement with the old assignments of *Takemoto et al.* [TAK72, TAK73, TAK74]. The Fe-N(phen) stretch lies at 220 (222) cm^{-1} in the HS state and at 368 (366) cm^{-1} in the LS state as measured by Raman (FIR) spectroscopy. The Fe-N(CS) stretch shifts from 252 (254) cm^{-1} (HS) to 376 (375) cm^{-1} (LS). The mode at 530 cm^{-1} which has formerly been ascribed to the Fe-N(CS) bond in the LS state is now assigned to an in-plane bend of the phenanthroline ligand with a remarkable participation of the Fe-N(phen) bond. These new assignments remove the discrepancy described above.

Finally, the series of compounds $[\text{Fe}(\text{PM-R})_2(\text{NCS})_2]$ with different α -diimine ligands PM-R has been investigated by means of Raman and infrared spectroscopy. A general range of 220 - 270 cm^{-1} (HS) and 340 - 400 cm^{-1} (LS) has been found for the asymmetric Fe-N stretch. The α -diimine stretches centered around 1600 cm^{-1} have been proven to be an additional vibrational probe of the spin state, especially in Raman measurements where the intensity of the C-N-stretch is rather low.

DFT calculations on a simplified model of a complex molecule with two α -diimine and two cis-NCS ligands reveal a factor of about 2 - 2.2 in the force constants of the Fe-N(diimine) bond. On the other hand the strength of the Fe-N(CS) bond changes only by a factor of ~ 1.2 when going from HS to LS state.

The values gained of the relevant vibrations as well as the strengthening factors of the Fe-N bonds can now be utilised to refine theoretical models for describing the spin transition.

Appendix

A.1 DFT results on tetrazole ligands

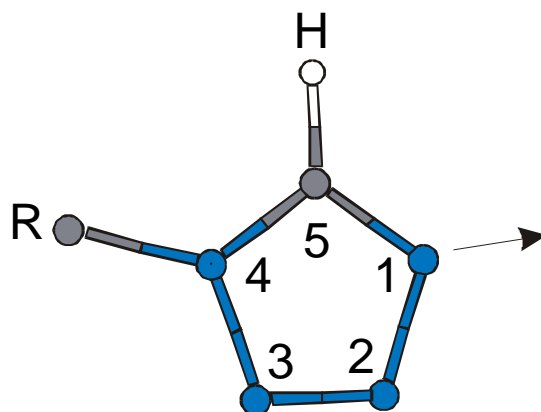


Figure A.1: Numbering scheme of the tetrazole ring.

Basis:		<i>ptz</i>		<i>mtz</i>			<i>htz</i>		<i>ptz</i>	
		experiment.	STO-3G	6-311G(d)	LanL2DZ	3-21G	LanL2DZ	STO-3G	6-311G(d)	
1	r 1-2	1.361	1.463	1.362	1.405	1.442	1.409	1.462	1.403	
2	r 1-5	1.325	1.365	1.313	1.345	1.329	1.343	1.366	1.332	
3	r 2-3	1.303	1.376	1.288	1.332	1.329	1.331	1.376	1.32	
4	r 3-4	1.342	1.444	1.353	1.399	1.418	1.396	1.443	1.387	
5	r 4-5	1.321	1.397	1.346	1.364	1.359	1.365	1.397	1.356	
6	r 4-R	1.503	1.501	1.454	1.465	1.468	(1.01)	1.509	1.466	
7	r 5-H		1.098	1.078	1.077	1.075	1.077	1.089	1.072	
8	α 3-4-5	108.49	108.335	107.49	108.18	107.74		108.218		
9	α 4-5-1	108.88	111.007	109.2	109.47	111.24		111.105		
10	α 4-5-H		122.752	124.49	125.23	123.62				
11	α 5-1-2	105.99	104.536	105.47	105.79	104.78		104.505		
12	α 5-4-R	129.81	130.029	131.17	131.29	131.64		129.726		

Table A.1: Calculated geometries of the pure ligand models with different basis sets in comparison with the X-ray structural values. (All distances in Å, angles in degrees).

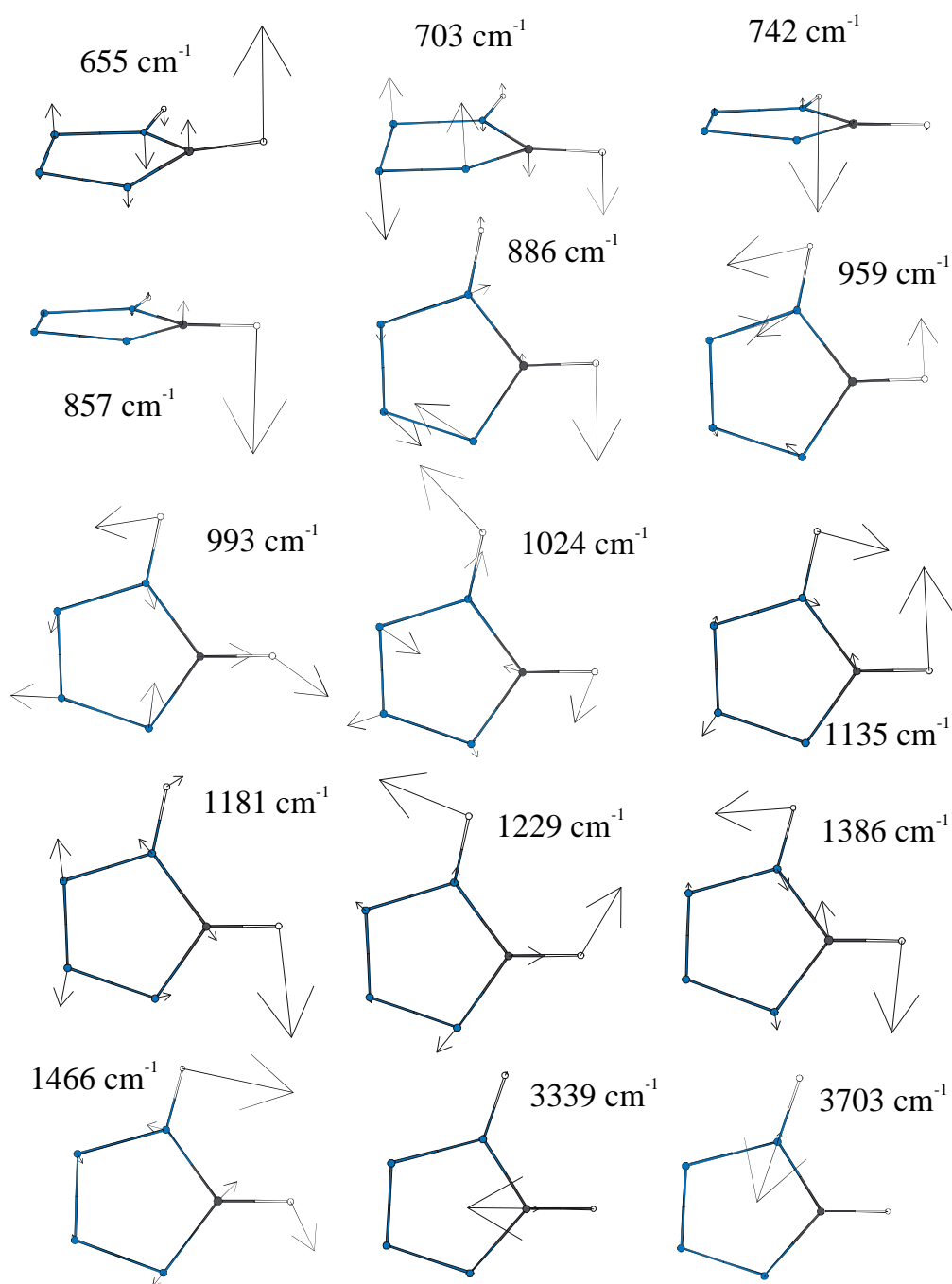
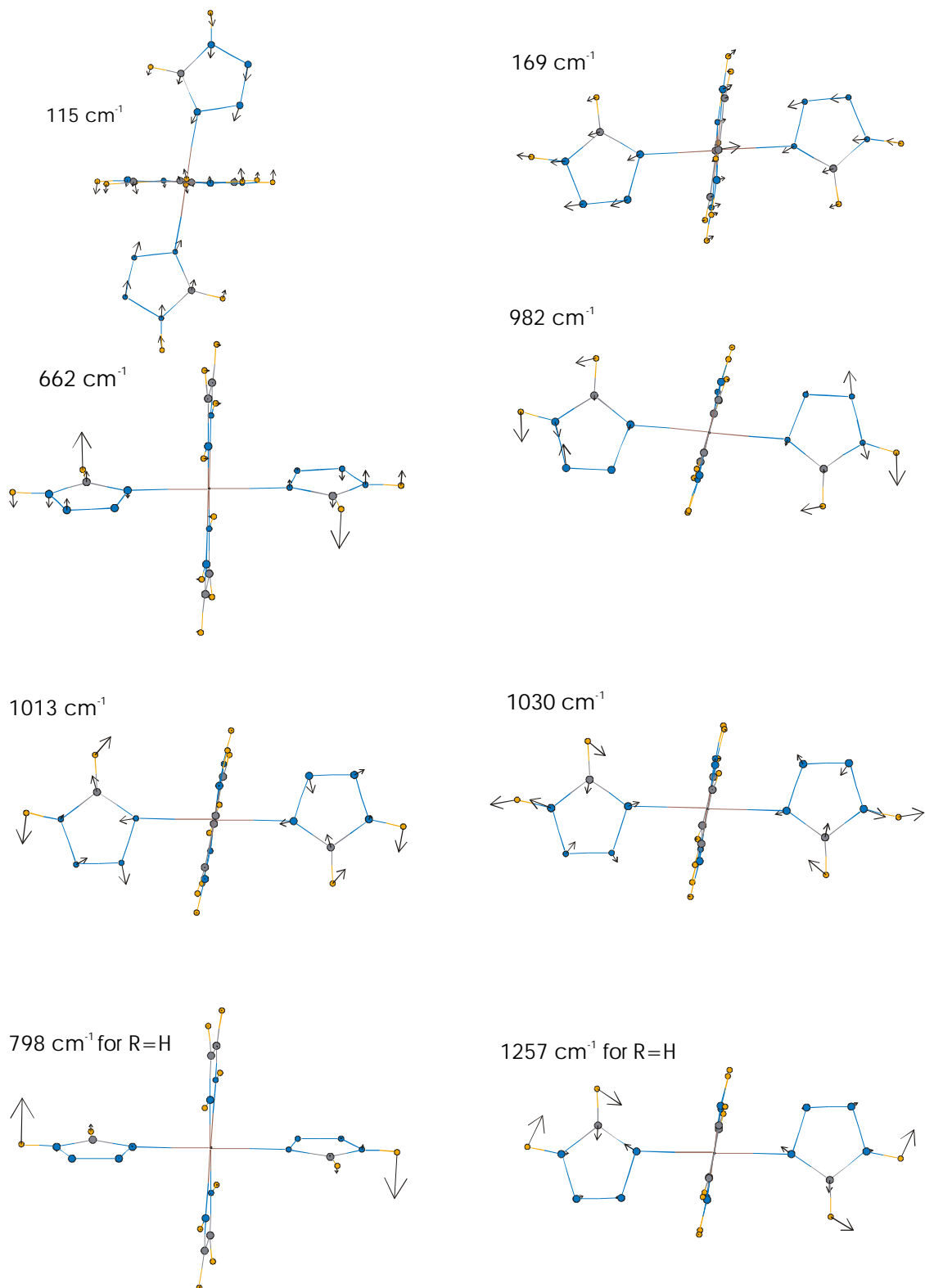


Figure A.2: Eigenvectors of H-tetrazole calculated with B3LYP/LanL2DZ.

A.2 DFT results on $[M(\text{htz})_2(\text{diimine})_2]^{2+}$ **A.2.1 $[\text{Zn}(\text{htz})_2(\text{diimine})_2]^{2+}$** Figure A.3: Selected normal modes with tetrazole participation in $[\text{Zn}(\text{htz})_2(\text{diimine})_2]^{2+}$.

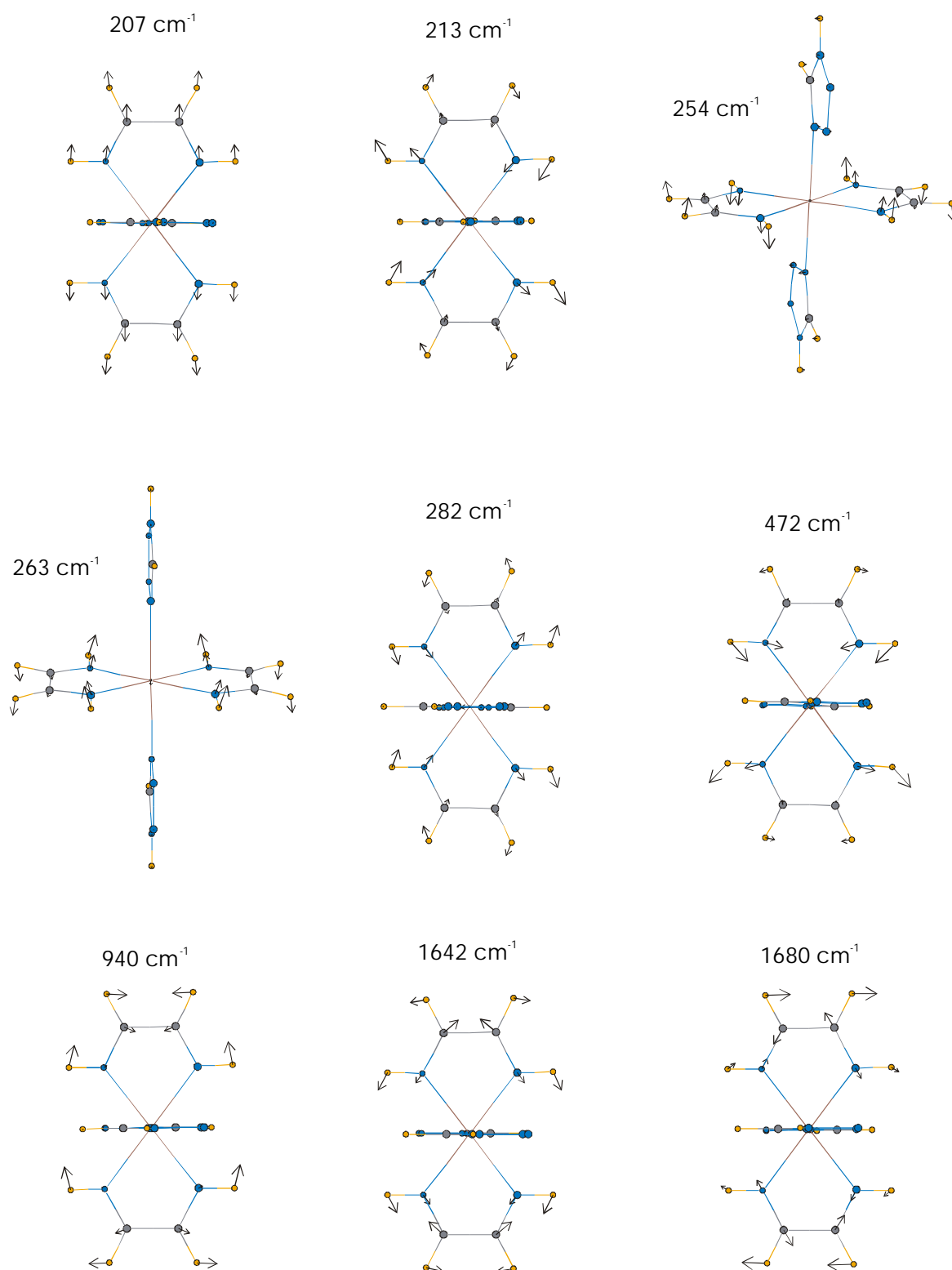
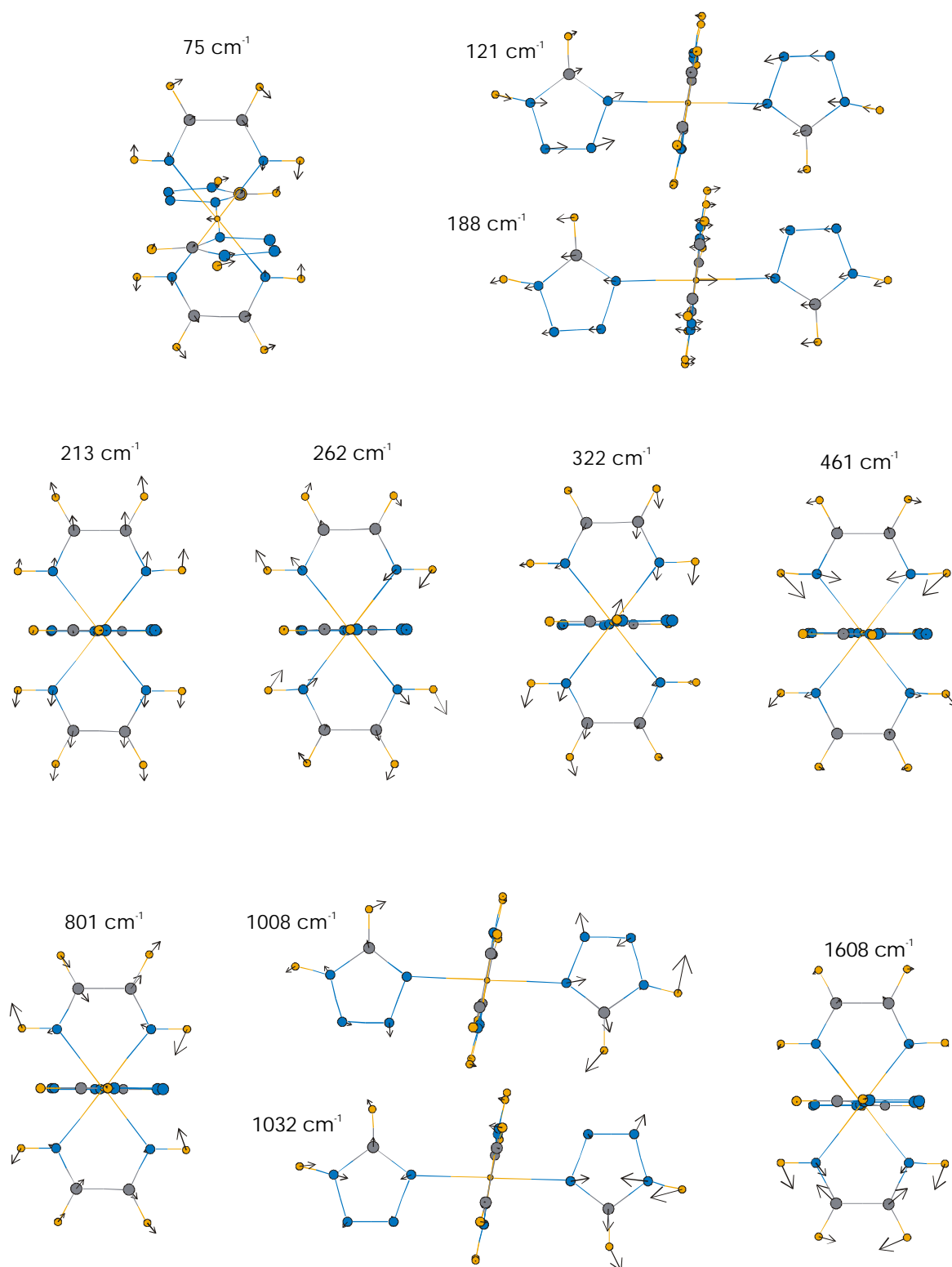


Figure A.4: Selected normal modes with diimine participation in $[\text{Zn}(\text{htz})_2(\text{diimine})_2]^{2+}$.

A.2.2 $[\text{Fe}^{\text{HS}}(\text{htz})_2(\text{diimine})_2]^{2+}$ Figure A.5: Selected normal modes of $[\text{Fe}^{\text{HS}}(\text{htz})_2(\text{diimine})_2]^{2+}$.

A.2.3 $[Fe^{LS}(htz)_2(diimine)_2]^{2+}$



Figure A.6: Selected normal modes of $[Fe^{LS}(htz)_2(diimine)_2]^{2+}$.

A.3 DFT results on [Fe(PM-H)(diimine)(NCS)₂]

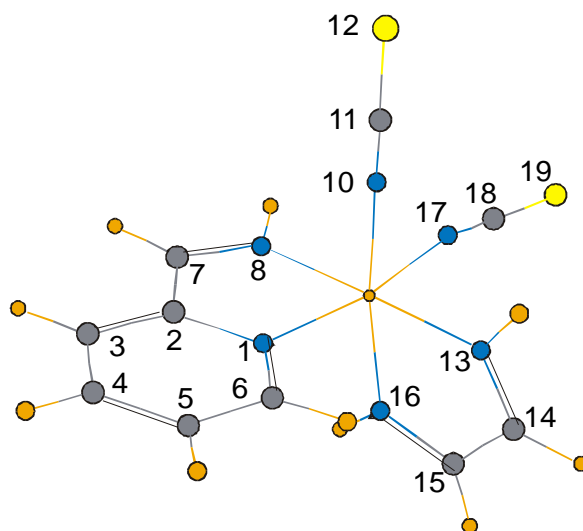


Figure A.7: Numbering scheme of the model.

Assignment	[Fe(PM-H)(diimine)(NCS) ₂]		
	HS (LanL2DZ)	LS (LanL2DZ)	PM-A (6-311G)
Fe-N-C bend	14, 17, 18, 19	6, 16, 18, 21	
torsions	45, 52, 66	65, 77,	35, 54
Fe-1 / diimine tors.	99, 110	110, 153	
PM-H oop rot.			95, 149, 207
Fe-17 / oct. bend	143		
oct. bend	160		
Fe-N-C bend	123, 171	170	
PM-H oop-rot. / Fe-N-CS	183	193, 209, 225, 242	
Fe-16/8/10	213	318	
Fe-1/8/13/16/10	225	416	
Fe-17 / diimine rot.	237	264	
PM-H/diimine ip-rot		198, 296	253
Fe-16/10	286 / 312	372	
ip 7			302
Fe-1/17 / diimine rot.	304	390	
PM-H ip			388, 591, 645, 651 666
Fe-13	314		
Fe-8	348	467	
diimin oop	376	511	
PM-H oop	438	436	423, 426, 451, 484
NCS bend	441, 449, 454, 459	425, 433, 439, 449	
ip 1/2/5	487	521	
diimine ip	490	564	

PM-H oop	498	492, 542	
ip 1/4	648	663	
wag H (diimine)	673	728	
ip 7/3	687	701	
wag H (PM-H)	747, 788	751, 793	701, 723, 771, 794
C-S	791, 806	781, 788	
diimine ip	793	838	
wag H (diimine)	825, 1005, 1026, 1050	857, 1019, 1037	
ip 7/5	847	861	
wag H (PM-H)	881, 944, 1013, 1098	869, 940, 1011, 1046, 1061	862, 873, 937, 948, 970, 1002, 1009, 1027, 1049
C-C (diimine)	1010	1017	
ip 1/3/5	1014	1031	1009
ip (PM-)A			758, 1030, 1057, 1117, 1331
4-5 / 5-6	1064	1068	1066
ip H (PM-H)	1121, 1175, 1204, 1413	1130, 1183, 1205, 1410	1204, 1213, 1223, 1232, 1317, 1382, 1405, 1477
ip (PM)-A			1491, 1541, 1642
ip H (diimine)	1187, 1218, 1346	1187, 1221, 1363	
2-7	1263	1269	913, 1194
C-C/C-N (PM-H)	1330	1326	1289
1-2	1344	1342	
C-N (diimine)	1371, 1584	1423, 1594	
2-3/5-6	1466, 1627	1506, 1652	1124
1-2/1-6	1503	1470	1501, 1617
14-15	1512	1528	
1-2/4-5	1604	1592	1596
7-8	1672	1629	1607, 1632
N-C(S)	2063, 2081	2123, 2138	
C-H	3132, 3165, 3190, 3215, 3227, 3237, 3253	3187, 3202, 3220, 3224, 3233, 3246, 3263	3159, 3168, 3170, 3180, 3180, 3194, 3201, 3225, 3227
N-H	3520, 3524, 3531	3529, 3533, 3541	3405

Table A.2: Calculated frequencies [cm^{-1}] of the model system $[\text{Fe}(\text{PM-H})(\text{diimine})(\text{NCS})_2]$ and the ligand PM-A with their assignment.

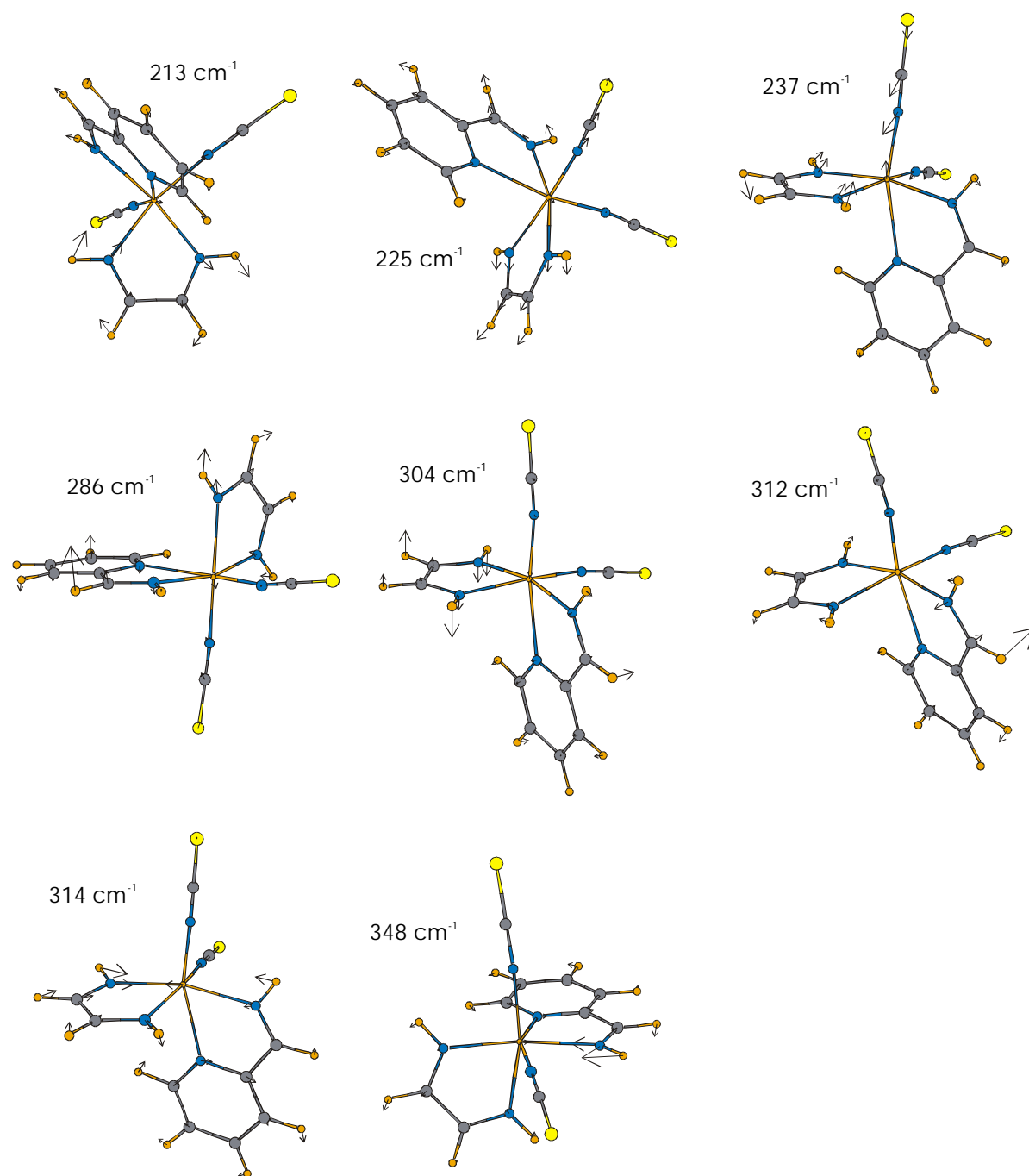


Figure A.8: HS modes with mainly Fe-N character.

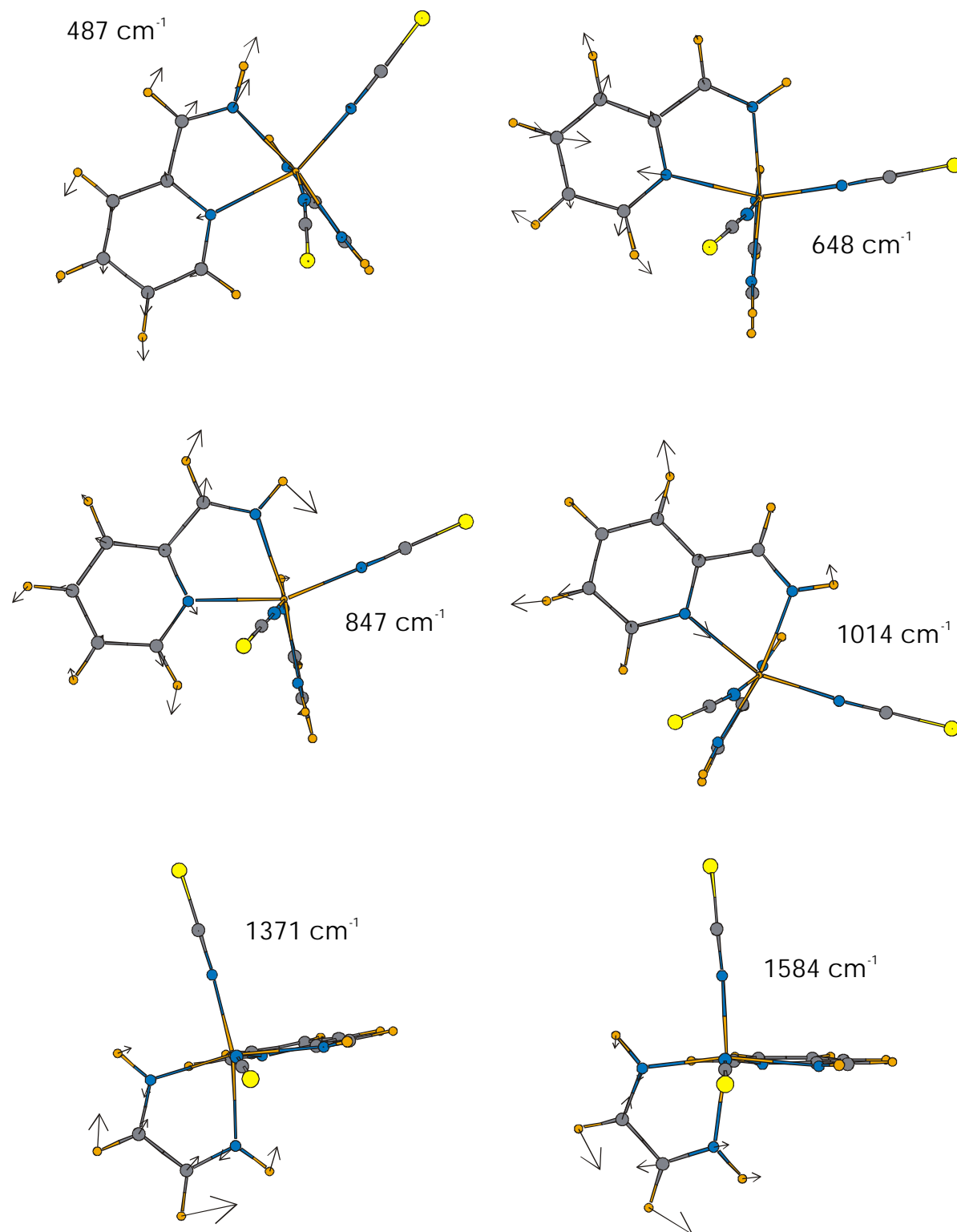


Figure A.9: HS intra-ligand modes with significant Fe-N participation.

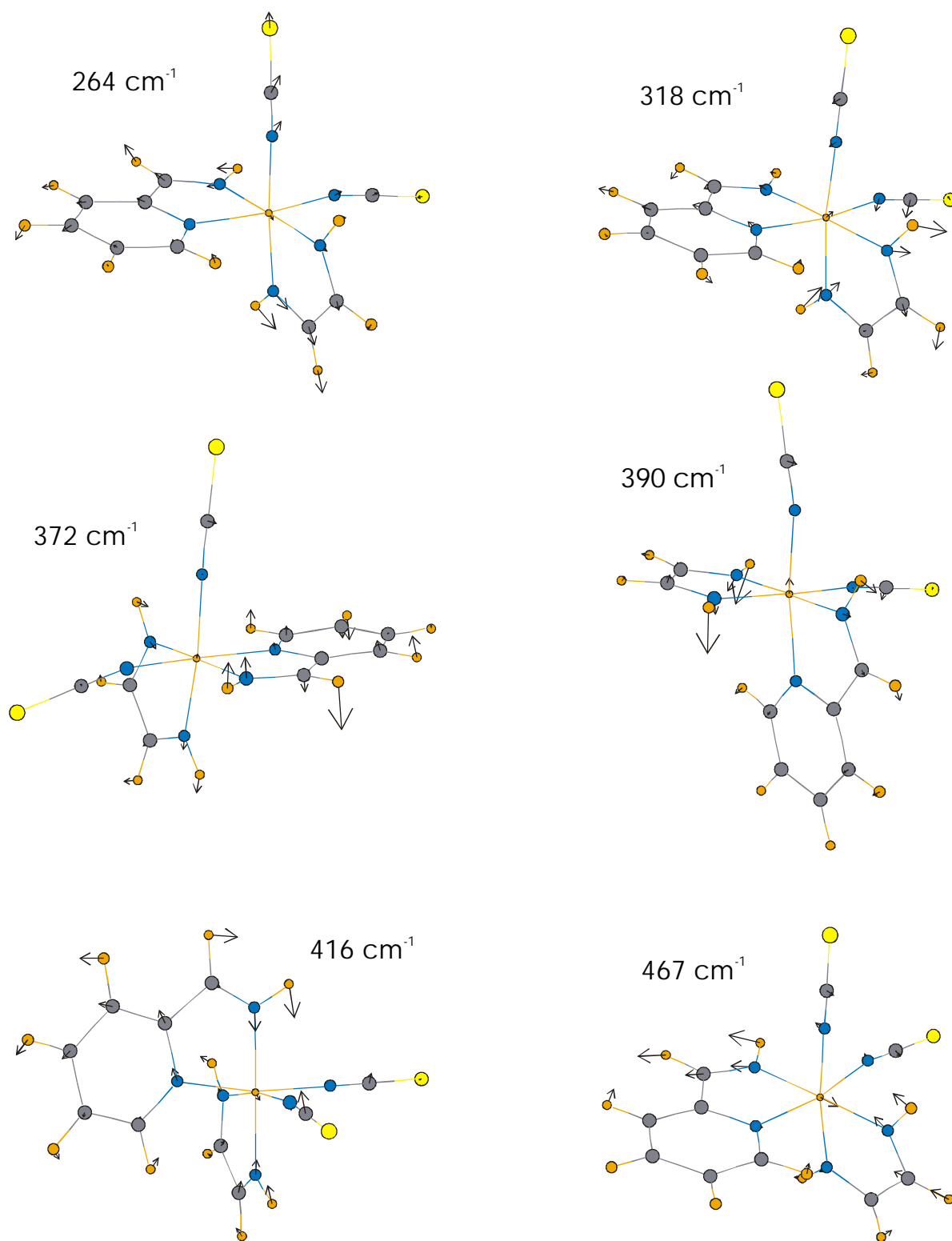


Figure A.10: LS modes with mainly Fe-N character.

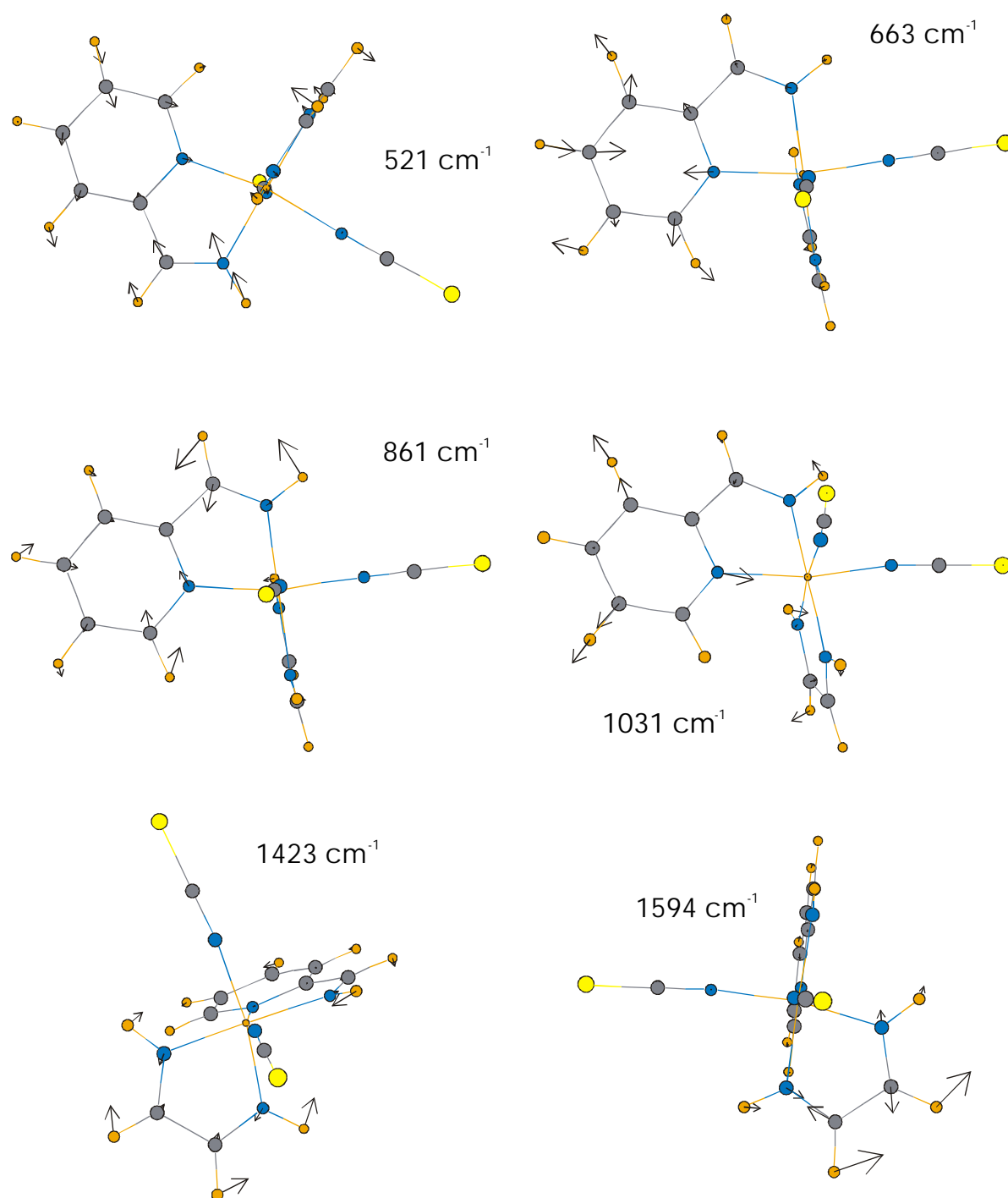


Figure A.11: LS intra-ligand modes with significant Fe-N participation.

Bibliography

- [ALL93] A. Allouche and J. Pourcin, *Spectrochim. Acta* **49A**, 571 (1993)
- [BAK64] W. A. Baker and H. M. Bobonich, *Inorg. Chem.* **3**, 1184 (1964)
- [BAT83] W.H. Batschelet and N.J. Rose, *Inorg. Chem.* **22**, 2078 (1983)
- [BAT83b] W.H. Batschelet and N.J. Rose, *Inorg. Chem.* **22**, 2083 (1983)
- [BEA88] J. K. Beattie, *Adv. Inorg. Chem.* **32**, 1 (1988)
- [BEC93] A. D. Becke, *J. Chem. Phys.* **98**, 5648 (1993)
- [BRO96] R. Bronisz, Z. Ciunik, K. Drabent, and M. F. Rudolf, *3rd European Workshop on Magnetic Molecular Materials*, Aussois, 14.-18. Sept. 1996
- [BRO96b] R. Bronisz, Z. Ciunik, K. Drabent, and M. F. Rudolf, *Conference Proceedings Vol. 50 «ICAME 95»*, I. Ortalli (Ed.), SIF, Bologna, 1996
- [CAM31] L. Cambi and A. Cagnasso, *Atti Accad. Naz. Lincei* **13**, 809 (1931)
- [CLA77] R. J. H. Clark, P. C. Turtle, D. P. Strommen, B. Streusand, J. Kincaid, and K. Nakamoto, *Inorg. Chem.* **16**, 84 (1977)
- [COT90] F. A. Cotton, *Chemical Applications of Group Theory*, 3rd Ed., J. Wiley & Sons, New York, 1990
- [DEC84] S. Decurtins, P. Gülich, C. P. Köhler, H. Spiering, and A. Hauser, *Chem. Phys. Lett.* **105**, 1 (1984)
- [DEC85] S. Decurtins, P. Gülich, K. M. Hasselbach, H. Spiering, and A. Hauser, *Inorg. Chem.* **24**, 2174 (1985)
- [DEC85b] S. Decurtins, P. Gülich, C. P. Köhler, and H. Spiering, *J. Chem. Soc. Chem. Comm.* **1985**, 430
- [DEN00] A. Dennis, *private communication*
- [DUN76] T. H. Dunning, Jr. and P. J. Hay in *Modern Theoretical Chemistry* (ed.: H. F. Schaefer, III), Plenum, New York, 1976
- [FOR95] J. B. Foresman and Æ. Frisch, *Exploring Chemistry with Electronic Structure Methods*, 2nd ed., Gaussian, Inc., Pittsburgh, PA, 1995-1996
- [FRA82] P. L. Franke, J. G. Haasnoot, and A. P. Zuur, *Inorg. Chim. Acta* **59**, 5 (1982)
- [GAL90] B. Gallois, J.-A. Real, C. Hauw, and J. Zarembowitch, *Inorg. Chem.* **29**, 1152 (1990)
- [GAN81] P. Ganguli, P. Gülich, E. W. Müller, and W. Irlner, *J. Chem. Soc., Dalton Trans.*, **1981**, 441
- [GAU94] Gaussian 94, Revision E.2, M. J. Frisch, G. W. Trucks, H. B. Schlegel, P. M. W. Gill, B. G. Johnson, M. A. Robb, J. R. Cheeseman, T. Keith, G. A. Petersson, J. A. Montgomery, K. Raghavachari, M. A. Al-Laham, V. G. Zakrzewski, J. V. Ortiz, J. B. Foresman, J. Cioslowski, B. B. Stefanov, A. Nanayakkara, M. Challacombe, C. Y. Peng, P. Y. Ayala, W. Chen, M. W. Wong, J. L. Andres, E. S. Replogle, R. Gomperts, R. L. Martin, D. J. Fox, J. S. Binkley, D. J. Defrees, J. Baker, J. P. Stewart, M. Head-Gordon, C. Gonzalez, and J. A. Pople, Gaussian, Inc., Pittsburgh PA, 1995.
- [GRI70] W. P. Griffith and G. T. Turner, *J. Chem. Soc. A*, **1970**, 858
- [GÜT81] P. Gülich, *Struct. Bond.* **44**, 83 (1981)
- [GÜT94] P. Gülich, H. Spiering, and A. Hauser, *Angew. Chem.* **106**, 2109 (1994), See also *Angew. Chem. Int. Ed. Engl.*, **33**, 2024 (1994)

- [GÜT96] P. Gütlich, J. Jung, and H.A. Goodwin, *Spin transitions in Iron(II) Complexes in Molecular Magnetism - from Assemblies to Devices*, E. Coronado, P. Delhaès, D. Gatteschi, and J. S. Miller (eds.), NATO ASI Series: Series E - Applied Sciences - Vol.321, 327 (1996), Kluwer Academic Publ., NL
- [HAU86] A. Hauser, Chem. Phys. Lett. **124**, 543 (1986)
- [HAU91] A. Hauser, Habilitationsschrift, Universität Mainz, 1991
- [HAU91b] A. Hauser, J. Chem. Phys. **94**, 2741 (1994)
- [HAY85] P. J. Hay and W. R. Wadt, J. Chem. Phys. **82**, 270 and 299 (1985)
- [HER86] R. Herber and L. M. Casson, Inorg. Chem. **25**, 847 (1986)
- [HOE95] A. Hofer, Diplomarbeit, Universität Mainz, 1995
- [HUP85] J. T. Hupp, and M. J. Weaver, J. Phys. Chem. **89**, 2795 (1985)
- [HUT70] B. Hutchinson, J. Takemoto, and K. Nakamoto, J. Am. Chem. Soc. **92**, 3335 (1970)
- [JUN95] J. Jung, PhD thesis, Universität Mainz, 1995
- [KHA91] S. U. M. Khan, and Z. Y. Zhou, J. Chem. Soc. Faraday Trans., **87**, 535 (1991)
- [KNÖ71] E. Knözinger, Chemiker-Zeitung **23/24**, 983 (1971)
- [KÖN67] E. König and K. Madeja, Inorg. Chem. **6**, 48 (1967)
- [KÖN70] E. König and K. J. Watson, Chem. Phys. Lett. **6**, 457 (1970)
- [KÖN74] E. König, G. Ritter, and R. Schnakig, Chem. Phys. Lett. **27**, 23 (1974)
- [KÖN91] E. König, Struct. Bond. **76**, 51 (1991)
- [KSE98] V. Ksenofontov, G. Levchenko, H. Spiering, P. Gütlich, J.-F. Létard, Y. Bouhedja, and O. Kahn, Chem. Phys. Lett. **294**, 545 (1998).
- [KUS99] J. Kusz, private communication
- [LEH99] N. Lehnert, PhD thesis, Universität Mainz, 1999
- [LET97] J.-F. Létard, S. Montant, P. Guionneau, P. Martin, A. L. Calvez, E. Freysz, D. Chasseau, R. Lapouyade, and O. Kahn, J. Chem. Soc., Chem. Commun. **1997**, 745
- [LET97b] J.-F. Létard, P. Guionneau, E. Coddjovi, O. Lavastre, G. Bravic, D. Chasseau, and O. Kahn, J. Am. Chem. Soc., **119**, 10861 (1997)
- [LET98] J.-F. Létard, P. Guionneau, L. Rabardel, J. A. K. Howard, A. E. Goeta, D. Chasseau, and O. Kahn, Inorg. Chem. **37**, 4432 (1998)
- [LET98b] J.-F. Létard, *private communication*
- [LET99] J.-F. Létard, L. Capes, G. Chastanet, N. Moliner, S. Létard, J.-A. Real, and O. Kahn, Chem. Phys. Lett. **313**, 115 (1999)
- [MAD66] K. Madeja, W. Wilke, and S. Schmidt, Z. Anorg. Chem., **346**, 306 (1966)
- [MCI78] D.F. McIntosh, K.H. Michaelian, and M.R. Peterson, Can.J.Chem. **56**, 1289 (1978) ; *QCPE* programme package 576
- [MIK80] M. Mikami, K. Konno, and Y. Saito, Acta Cryst. **B36**, 275 (1980)
- [MIY58] T. Miyazawa, J. Chem. Phys. **29**, 246 (1958)
- [MÜL82] E. W. Müller, H. Spiering, and P. Gütlich, Chem. Phys. Lett. **93**, 567 (1982)
- [MÜL83] E.W. Müller, J. Ensling, and H. Spiering, Inorg. Chem. **22**, 2074 (1983)
- [MÜL83b] E.W. Müller, H. Spiering, and P. Gütlich, J. Chem. Phys. **79**, 1439, 1983
- [NAK62] I. Nakagawa and T. Shimanouchi, Spectrochim. Acta **18**, 101 (1962)

- [NAK64] I. Nakagawa and T. Shimanouchi, *Spectrochim. Acta* **20**, 429 (1964)
- [NOY62] R.M. Noyes, *J. Am. Chem. Soc.* **84**, 513 (1962)
- [OCH99] Joseph W. Ochterski, White paper: '*Vibrational Analysis in Gaussian*', 1999
- [OZA89] A. Ozarowski and B.R. McGarvey, *Inorg. Chem.* **28**, 2262 (1989)
- [PAR89] R. G. Parr and W. Yang, *Density-Functional Theory of Atoms and Molecules*, 1st ed., Oxford University Press, New York, 1989
- [PAU99] H. Paulsen, *to be published*
- [POG90] P. Poganiuch, S. Decurtins, and P. Gülich, *J. Am. Chem. Soc.* **112**, 3270 (1990)
- [QUI71] A. S. Quist, J. B. Bates, and G. E. Boyd, *J. Chem. Phys.* **54**, 4896 (1971)
- [ROM93] H. Romstedt, PhD thesis, Universität Mainz, 1993
- [RUD95] M. F. Rudolf, R. Bronisz, Z. Ciunik, and K. Drabent, *2nd Spin-Crossover Family Meeting*, Gif sur Yvette, France, 27.-28.Oct.1995
- [SAI72] Y. Saito, J. Takemoto, B. Hutchinson, and K. Nakamoto, *Inorg. Chem.* **11**, 2003 (1972)
- [SCH75] K. H. Schmidt and A. Müller, *Inorg. Chem.* **14**, 2183 (1975)
- [SCH76] K. H. Schmidt and A. Müller, *Coord. Chem. Rev.* **19**, 41 (1976)
- [SCH80] H.L. Schläfer and G. Gliemann, *Einführung in die Ligandenfeldtheorie*, Akadem. Verlagsgesellschaft, Wiesbaden, **1980**, pp. 462
- [SCH89] G. Schmitt, Diplomarbeit, Universität Mainz, 1989
- [SCH96] G. Schaftenaar, *Molden*, version 3.2, CAOS/CAMM Center, University of Nijmegen, Netherlands, 1996
- [SOR74] M. Sorai and S. Seki, *J. Phys. Chem. Solids* **35**, 555 (1974)
- [SUG70] S. Sugano, Y. Tanabe, and H. Kamimura, *Multiplets of Transition-Metal Ions in Crystals*, volume 33 of *Pure and Applied Physics*, Academic Press, (New York), 1970
- [SZA89] A. Szabo and N. S. Ostlund, *Modern Quantum Chemistry*, 1st ed. (revised), McGraw-Hill, New York, 1989
- [TAK72] J.H. Takemoto and B. Hutchinson, *Inorg. Nucl. Chem. Letters* **8**, 769 (1972)
- [TAK73] J.H. Takemoto and B. Hutchinson, *Inorg. Chem.* **12**, 705 (1973)
- [TAK74] J.H. Takemoto, B. Streusand, and B. Hutchinson, *Spectrochim. Acta Part A* **30**, 827 (1974)
- [TOF84] H. Toftlund, E. Pedersen, and S. Yde-Andersen, *Acta Chem. Scand., Ser. A*, **37**, 693 (1984)
- [TOF89] H. Toftlund, *Coord. Chem. Rev.* **94**, 67 (1989)
- [VOL72] H. Volkmann, *Handbuch der Infrarot-Spektroskopie*, Verlag Chemie, Weinheim, 1972
- [WAD85] W. R. Wadt and P. J. Hay, *J. Chem. Phys.* **82**, 284 (1985)
- [WIE86] L. Wiehl, G. Kiel, C. P. Köhler, H. Spiering, and P. Gülich, *Inorg. Chem.* **25**, 1565 (1986)
- [WIE93] L. Wiehl, *Acta Cryst.* **B49**, 289 (1993)
- [WIL55] E. B. Wilson, Jr. , J. C. Decius, and P. C. Cross, *Molecular Vibrations*, 1st ed. McGraw-Hill, New York, 1955
- [XMO93] *XMol*, version 1.3.1, Minnesota Supercomputer Center, Inc., Minneapolis, MN, 1993

Acknowledgement

First of all I want to thank the group leader for providing the interesting subject of this thesis and the excellent working conditions with his well-equipped experimental facilities. The possibility to be part of the TOSS team enabled me to establish fruitful contacts within the scientific community.

This thesis would not have the structure and the 'scientific language' without the enduring help of my supervisor. The 'endless' discussions with you opened my mind for lots of things, I wouldn't even have noticed. Thank you, Hartmut.

Felix introduced me to Raman spectroscopy. You have always been the expert, when experimental or theoretical problems arose. Thank a lot, Felix.

The group in Belfast helped me a lot in 'searching for the relevant frequencies'. Especially the cooperation with Andrew and the fruitful discussions with you, John, gave me new impulses for working on this subject. Jean-François from Bordeaux kindly supplied me with his series of compounds. Hauke from Lübeck kindly communicated the results from his calculations before publication.

I have to express my gratitude to Ulrich and Nils for teaching me everything I never dared to ask about computers and Gabi for her great support in fighting against university's bureaucracy. All members of the group, which cannot be mentioned individually, have been responsible for the excellent working atmosphere. This contributed a lot to retaining my enthusiasm for scientific work.

That science is not everything, was made possible by my dear colleagues and friends Renée 'Miss D.', Thorsten 'Rosta', Nicolai 'Elwood', Franz 'Yakisoba', Axel, Beatrix and Christina. Besides the scientific support, excursions to the Linden- or Apfelbaum, never-ending Muschelfeten or Biofeten and cycle tours to Straußwirtschaften made the last years a marvellous time at Mainz.

All the students of biology, which have been tortured by me during my practical courses, have to be mentioned for 'teaching me teaching'. It was an experience I don't want to miss.

I really have to thank Christina for her endurance and understanding during the end phase of my thesis. It wouldn't have gone that way without you.

Last, but not least, I want to thank my parents for their support all over the years. My scientific education was made possible by your help and understanding.

Vita

Andreas Hofer
Elgerter Straße 1
56269 Dierdorf
Germany
Andreas@Hofer.net

Personal data

Date and place of birth 18th April 1970, Koblenz (Germany)

Education

76 - 80 : Grund- und Hauptschule, Dierdorf (primary school)
80 - 89 : Martin-Butzer-Gymnasium, Dierdorf (secondary school)
Final examination (Abitur) in May 1989

Military service

06/89 - 08/90: Westerwaldkaserne, Montabaur

University training

10/90 - 9/95: Student of chemistry, Johannes Gutenberg-Universität, Mainz
9/95: Master thesis at the Institute of Inorganic Chemistry on

*‘Temperaturabhängige Ramanspektroskopie an Einkristallen
des Spincrossover systems $[M(ptz)_6](X)_2$, ($M = Fe, Zn$; $X = BF_4, ClO_4$)’*

since 10/95: graduate studies at the Johannes Gutenberg-Universität, Mainz
on:

*‘Vibrational Spectroscopy
on thermally and optically switchable spin crossover compounds’*

December 6th, 2000: Viva Voce

Career

01/95 - 12/95: scientific assistant, Universität Mainz
01/96 - 11/99: scientific staff member at the Institute of Inorganic Chemistry
since 03/00: Training as 'junior consultant SAP R/3 process industry', GIB mbH, Mainz

Conferences

10/95 - Posterpresentation	2nd Spin Crossover Family Meeting, <i>Gif sur Yvette</i>
02/96	Research visit <i>University of Belfast</i>
07/97 - Posterpresentation	12th International Symposium on Photochemistry and Photophysics of Coordination Compounds, <i>Colchester, USA</i>
04/98 - Lecture	1st European TMR-TOSS Meeting, <i>Seeheim</i>
08/98 - Posterpresentation	33rd Int. Conference on Coordination Chemistry, <i>Florenz</i>
09/98 - Posterpresentation	3rd Int. Conference on Molecular Magnets, <i>Seignosse</i>
04/99	4th Spin Crossover Family Meeting, <i>Seeheim</i>